Imaging and modeling the cardiovascular system

Elira Maksuti

Doctoral Thesis

KTH Royal Institute of Technology
School of Technology and Health
Department of Medical Engineering
SE-141 57 Huddinge, Sweden

Karolinska Institutet
Department of Molecular Medicine and Surgery
Clinical Physiology
SE-171 76 Stockholm, Sweden

TRITA-STH Report 2016:9
ISSN: 1653-3836
ISRN/KTH/STH/2016:9-SE
ISBN: 978-91-7729-192-3

Printed in Sweden by Universitetsservice US-AB, Stockholm 2016

Preface

This thesis is submitted to the KTH Royal Institute of Technology and Karolinska Institutet (KI) in partial fulfillment of the requirements for the Joint Doctoral Degree in Medical Technology. The work has mainly been performed at KTH School of Technology and Health in Huddinge, Sweden, and KI, Department of Clinical Physiology in Stockholm, Sweden, with Associate Professor Michael Broomé as main supervisor, Associate Professor Anna Bjällmark, Associate Professor Matilda Larsson and Associate Professor Martin Ugander as cosupervisors. Six months were spent at the Laboratory of Hemodynamics and Cardiovascular Technology at the École polytechnique fédérale de Lausanne (EPFL) in Lausanne, Switzerland, where Study III was performed, under the supervision of Professor Nikos Stergiopulos. The research projects were supported by grants from the Swedish Research Council (2012-2800, 2012-2795), VINNOVA VINNMER Marie Curie International Qualification Grant (2011-01365) and the Hans Werthén scholarship from The Royal Swedish Academy of Engineering Sciences (IVA).

The thesis will be publicly defended at 10 am, December 9, 2016, in the T2 lecture hall, Hälsovägen 11C, Huddinge, Sweden.

Abstract

Understanding cardiac pumping function is crucial to guiding diagnosis, predicting outcomes of interventions, and designing medical devices that interact with the cardiovascular system. In turn, better diagnostics and treatment of cardiovascular function would improve the prognosis of cardiovascular diseases, which account for 31% of all global deaths. The heart and the vascular system are strongly coupled, and changes in arterial properties that occur with age and in the presence of pathologies have a significant impact on cardiac function. Because of the complexity of the cardiovascular system and the diversity of disease processes, it is not always possible to understand the role played by each part of the system in the final outcome. Computer simulations of hemodynamics can show how the system is influenced by changes in single or multiple cardiovascular parameters and can be used to test clinically relevant hypotheses. In addition, methods for the detection and quantification of important markers such as elevated arterial stiffness would help reduce the morbidity and mortality related to cardiovascular disease.

The general aim of this thesis work was to improve understanding of cardiovascular physiology and develop new methods for assisting clinicians during diagnosis and follow-up of treatment in cardiovascular disease. Both computer simulations and medical imaging were used to reach this goal.

In the first study, a new cardiac model based on piston-like motions of the atrioventricular plane was developed in order to deepen the understanding of the forces responsible for filling and emptying of the cardiac chambers. In the second study, the presence of the anatomical basis needed to generate hydraulic forces during diastole was assessed in heathy volunteers. In the third study, a previously validated lumped-parameter model was used to quantify the contribution of arterial and cardiac changes to blood pressure during aging. In the fourth study, in-house software that measures arterial stiffness by ultrasound shear wave elastography (SWE) was developed and validated against mechanical testing.

The studies showed that longitudinal movements of the atrioventricular plane can well explain cardiac pumping and that the macroscopic geometry of the heart enables the generation of hydraulic forces that aid ventricular filling. Additionally, simulations showed that structural changes in both the heart and the arterial system contribute to the progression of blood pressure with age. Finally, the SWE technique was validated to accurately measure stiffness in arterial phantoms. Future *ex vivo* and *in vivo* studies are needed to determine the technique's sensitivity and applicability to clinical measurements.

Keywords: cardiac pumping, diastolic function, hemodynamics, modeling, simulation, arterial stiffness, ultrasound, shear wave elastography.

Sammanfattning

Förståelsen av hjärtats pumpmekanism är central för att kunna ställa diagnos, förutsäga behandlingseffekter och för att kunna utveckla medicinteknisk utrustning inom kardiovaskulär sjukvård. I sin tur skulle bättre diagnostik och behandling kunna förbättra prognosen för hjärt- och kärlsjukdomar, vilka orsakar 31 % av alla dödsfall i världen. Hjärtat och kärlsystemet är sammankopplade och förändringar i blodkärlens egenskaper i samband med åldrande och sjukdom påverkar hjärtats funktion signifikant. Det kardiovaskulära systemets komplexitet och mångfalden av sjukdomar gör att det inte alltid är möjligt att förstå hur en enskild del av systemet påverkar helheten. Datorbaserade simulering av hemodynamik har förmågan att visa hur hela systemet påverkas av förändringar i en enskild eller flera kardiovaskulära parametrar samtidigt. På så sätt kan man testa kliniska hypoteser om sjukdomar eller deras behandling. På liknande sätt kan nya metoder för att detektera och kvantifiera kärlstyvhet också tänkas bidra till att minska sjuklighet och dödlighet relaterad till hjärt- och kärlsjukdomar.

Det allmänna syftet med denna avhandling är att förbättra förståelsen av hjärt- och kärlsystemets fysiologi samt att utveckla nya metoder för att kunna stödja klinikerna med diagnostik, behandling och uppföljning av hjärt- och kärlsjukdomar. Både datorbaserade simuleringar och medicinsk bildteknik användes för att nå detta mål.

I den första studien utvecklades en modell av hjärtats pumpmekanism baserad på den kolvliknande rörelsen av det atrioventrikulära planet (AV-planet) mellan hjärtats bägge förmak och kammare. Syftet med modellen var att utveckla förståelsen av krafterna som verkar när hjärtrummen fylls och töms. I den andra studien utvärderades om hjärtats anatomi skapar förutsättningar för att generera en hydraulisk kraft under hjärtats fyllnadsfas (diastole) hos friska frivilliga försökspersoner. I den tredje studien användes en tidigare validerad modell för att bestämma hur mycket förändringar i hjärtat och kärlsystemet medverkar till blodtryckets förändringar under åldrande. I fjärde studien utvecklades en egen mjukvara för att kunna mäta kärlstelhet med användning av den ultraljudsbaserade tekniken skjuvvågselastografi (Shear wave elastography – SWE), som sedan validerades med experimentell mekanisk testning.

Studierna visade att de longitudinella rörelserna hos AV-planet väl kan förklara hjärtats pumpförmåga och att hjärtats egen geometri ger förutsättningar för att generera hydrauliska krafter som understödjer kammarens fyllnad. Dessutom visade simuleringar att strukturella förändringar i hjärtat och kärlsystemet bägge påverkar ändringar i blodtryck med ålder. Till sist, visades att SWE-tekniken med noggrannhet kunde mäta stelheten i kärlfantomer. Ytterligare *ex vivo*- och *in vivo*-studier behövs för att avgöra om tekniken kan användas kliniskt.

Riassunto

Comprendere il meccanismo attraverso il quale il cuore assolve la sua funzione di pompaggio è fondamentale per poter aiutare la diagnostica, predire il risultato dei trattamenti e progettare strumentazioni biomedicali che interagiscano opportunamente con il sistema cardiovascolare. Migliori strumenti di diagnosi e per il trattamento della funzione cardiovascolare possono migliorare la prognosi delle malattie cardiovascolari, le quali causano il 31% delle morti a livello globale.

Il cuore e il sistema vascolare sono fortemente interconnessi. Di conseguenza cambiamenti strutturali delle proprietà delle arterie, che occorrono con l'età e in presenza di patologie, hanno un impatto importante sulla funzione cardiaca. A causa della complessità del sistema cardiovascolare e della varietà dei processi patologici, non è sempre possibile comprendere il ruolo di ciascuna parte del sistema nel funzionamento complessivo. Simulazioni al computer di emodinamica hanno la capacità di mostrare come il sistema sia influenzato dal cambiamento di un singolo o di molteplici parametri cardiovascolari. Le simulazioni permettono anche di testare ipotesi di rilievo clinico. In aggiunta, metodi per misurare marker importanti, come un'elevata rigidezza delle arterie, possono aiutare a ridurre la morbilità e la mortalità associate alle malattie cardiovascolari.

L'obiettivo generale del lavoro presentato in questa tesi è stato quello di migliorare la comprensione della fisiologia dell'apparato cardiocircolatorio e sviluppare nuovi metodi per aiutare i medici durante il processo di diagnosi e di monitoraggio dei trattamenti delle malattie cardiovascolari. Per raggiungere quest'obiettivo sono state utilizzate sia simulazioni al computer che tecniche di diagnostica per immagini.

Nel primo studio è stato sviluppato un modello cardiaco basato sui movimenti del piano atrioventricolare, i quali possono essere paragonati a quelli di un pistone. L'obiettivo del modello è stato quello di migliorare la comprensione delle forze responsabili del riempimento e dello svuotamento dei ventricoli. Nel secondo studio è stato valutato in volontari sani se l'anatomia stessa del cuore è tale da generare delle force idrauliche che possano agevolare la fase diastolica. Nel terzo studio è stato utilizzano un modello a parametri concentrati precedentemente validato per quantificare il contributo dei mutamenti strutturali a livello arterioso e cardiaco sui cambiamenti della pressione sanguigna durante l'invecchiamento. Nel quarto studio è stato sviluppato un software basato sulla tecnica dell'elastografia delle onde di taglio (Shear wave elastography – SWE) in grado di misurare la rigidezza delle arterie da segnali ecografici. La tecnica è poi stata validata con un confronto con test meccanici.

Gli studi hanno mostrato che i movimenti longitudinali del piano atrioventricolare sono in grado di spiegare la funzione di pompaggio cardiaco e che la stessa geometria del cuore genera forze idrauliche che agevolano il riempimento dei ventricoli. Inoltre, le simulazioni hanno mostrato che cambiamenti strutturali sia del cuore sia delle arterie contribuiscono ai cambiamenti di pressione sanguigna che si manifestano con l'età. Infine, la tecnica SWE ha mostrato di poter accuratamente misurare la rigidezza di fantocci di arterie. Tuttavia,

ulteriori studi *ex vivo* ed *in vivo* sono necessari per determinare se la tecnica può essere utilizzata per misure in ambito clinico.

Acknowledgments

Many wonderful people have supported me during this journey and have contributed in different ways to this thesis and to my personal development. I wish to give special thanks to some of them.

I would like to thank my cosupervisors **Anna Bjällmark** and **Matilda Larsson** for being brave enough to hire me before there was a PhD position available. Thank you for trusting me, inspiring me, and helping me find my own way. Anna, thank you for helping me plan my path during these years by prioritizing my development as a researcher and as a teacher, letting me travel to all those interesting conferences, helping me structure my papers, and for sharing your energy and joy. Matilda, thanks for always finding time for me, for being there during all phases, through good and tough times. I admire how you can bring out the best in every situation and your ability to give honest and kind feedback.

Special thanks go to my main supervisor **Michael Broomé**, who thought me so much about physiology and helped me develop a clinical perspective on research and engineering. Michael, thank you for the long and interesting conversations about modeling, cardiovascular function, chaos theory, and much more. Thank you for helping me plan my exchange period at EPFL and visiting me in Lausanne. I will always remember celebrating my birthday discussing why vascular resistance increases with age, while eating delicious food from all over the world.

I also wish to thank my cosupervisor at Karolinska Institutet **Martin Ugander** who "adopted" me as a PhD student along the way. Martin, thank you for your enthusiasm and passion in cardiac physiology. Thank you for inspiring me and motivating me to do something important and always caring about my interests, ambitions and future path.

My journey started five years ago and it would have not been such a positive start without my colleague **Erik**. Thank you for showing me different perspectives on things, for encouraging and challenging me. We are different in many ways and working together made us both learn a lot from each other. Thank you for our fun trips and for your contribution to this thesis.

I wish to thank my colleague **David** for his contribution to Study IV and for being such a good and caring friend. I'm very happy I had the chance to work with you and I believe your wide competences, smart intuitions and your humbleness will make you a great scientist.

Thank you **Jonas** for introducing me to the world of cardiac pumping and inspiring me to understand more about it. Thank you **Tim** for making our Verasonics system work and for always being helpful. Thank you **Mamo** for being the most fun and cleaver discussion partner. Thank you **Malin** for being the best event organizer and good-mood bringer. Thanks **Mattias** for helping me when I needed it most and for sharing your teaching experience with me. Thank you **Dmitry** for always being available and interested in my

research. Thank you **Peter Arfert** for building our ingenuous experimental setups, which are an important part of this thesis work. Thank you **Chiara** for being a great member of the wellness group, for actively participating in the PhD activities and, most importantly, for your energizing step classes! Special thanks also go to all the other colleagues at the School of Technology and Health (STH) at KTH, who made my daily work so enjoyable.

Many people outside STH and Sweden have significantly contributed to my work. I wish to thank **Matthew W. Urban** at Mayo Clinic for teaching me so much about shear wave elastography, for being the best research host during both my visits at Mayo and for always finding time to discuss the details of research.

I wish to thank my coauthors in Study II **Marcus Carlsson** and **Håkan Arheden** at the Department of Clinical Physiology, Lund University, for the interesting discussion about cardiac pumping in the unusual setting of Stockholm's archipelago during winter.

I would like to thank **Nikos Stergiopulos** at the Laboratory of Hemodynamics and Cardiovascular Technology at EPFL for welcoming me to his group, for introducing me to the fascinating aspects of cardiovascular aging and also for introducing me to **Nico Westerhof** and **Berend Westerhof.** Nico, thank you for your detailed comments and endless passion for cardiovascular physiology and science. I've been very much inspired by you. Berend, thank you for your kind welcome in Amsterdam and for all your input and help with Study III. I would also like to send special thanks to **Bram Trachet** and **Lydia Aslanidou** for making me feel welcome at EPFL and creating such a pleasant environment in the office. Thank you for all the fun lunches and for our discussions about the purpose of science and its current directions.

I wish to thank all my friends in Stockholm, in Italy and around the world for always showing interest in my research and making these years so fulfilling and fun. Special thanks go to **Daniel Alzén** for his patience in correcting my Swedish mistakes and for explaining all the hidden details of this fascinating language and culture.

I would like to express my gratitude to my parents, **Liljana** and **Edmond,** and to my brother **Gjergj** for being my best supporters and for teaching me the importance of what you know rather than what you have.

Finally, I wish to give my warmest thanks to **Paolo** for his endless support, love and for inspiring me every day. Thank you for joining me, first in Lausanne whenever possible, and then in Stockholm. Thank you for making *us* possible.

Elira Maksuti
Stockholm, November 2016

Abbreviations

ASA	Atrial short-axis area
ARF	Acoustic radiation force
AV	Atrioventricular
C	Total arterial compliance
CMR	Cardiovascular magnetic resonance
CT	Computer tomography
DAE	Differential algebraic equation
E_{es}	End-systolic elastance
E_{ed}	End-diastolic elastance
$E(t)$	Time-varying elastance
ECG	Electrocardiogram
EF	Ejection fraction
fMRI	Functional magnetic resonance imaging
F/T	Freeze-thaw
IQ	In-phase and quadrature
L	Total inertance
LA	Left atrium
LV	Left ventricle
MAPSE	Mitral annular plane systolic excursion
MRI	Magnetic resonance imaging
ODE	Ordinary differential equation
P_{ed}	End-diastolic pressure
PET	Positron emission tomography
PRF	Pulse repetition frequency

PWV	Pulse wave velocity
R	Vascular resistance
RMSE	Root-mean-square error
ROI	Region of interest
SWE	Shear wave elastography
TAPSE	Tricuspid annular plane systolic excursion
VSA	Ventricular short-axis area
VSA_{Endo}	Ventricular short-axis endocardial area
VSA_{Epi}	Ventricular short-axis epicardial area
Z_c	Aortic characteristic impedance

Table of Contents

Preface i
Abstract iii
Sammanfattning (Swedish summary) v
Riassunto (Italian summary) vii
Acknowledgments ix
Abbreviations xi
Table of Contents xiii
1 Introduction 1
1.1 Motivations 2
1.2 Thesis outline 4
2 Aims 5
3 Included publications 7
3.1 List of publications 7
3.2 Division of work between authors 7
4 Background 9
4.1 Cardiovascular physiology 9
4.1.1 The heart 9
4.1.2 The arteries 15
4.1.3 Arterial–cardiac interaction 17
4.2 Modeling cardiovascular hemodynamics 18
4.2.1 Classification of models 18
4.2.2 Time-varying elastance model of cardiac contraction 19
4.2.3 The Windkessel model 19
4.2.4 Modeling by bond graphs 20
4.3 Imaging the cardiovascular system 22
4.3.1 Ultrasound imaging 22
4.3.2 Magnetic resonance imaging 24
4.3.3 Assessment of cardiac function 26
4.3.4 Assessment of vascular function 27
5 Methodology and contributions 33
5.1 Cardiovascular modeling 33

5.1.1 General description of the models 33
5.1.2 Equivalent bond graph models 38
5.1.3 Parameter selection 40
5.1.4 Simulations 45
5.2 Hydraulic forces physical model 45
5.3 *In vivo* measurements of atrial and ventricular short-axis areas 46
5.3.1 Study population 47
5.3.2 Area measurements 47
5.3.3 Diastolic filling forces comparison 47
5.4 Shear wave elastography 49
5.4.1 Phantom construction 49
5.4.2 Shear wave elastography setup 50
5.4.3 Software development 52
5.4.4 Mechanical testing 55
5.4.5 Shear wave elastography and mechanical testing comparison 56
6 Results 57
7 Discussion 63
7.1 Hydraulic forces and cardiac function 64
7.1.1 *In silico:* modeling 64
7.1.2 *In vitro:* physical model 66
7.1.3 *In vivo:* left atrial and ventricular short-axis areas 66
7.1.4 Additional implications of longitudinal pumping 67
7.2 Cardiovascular aging 69
7.3 Arterial shear wave elastography 70
7.4 General limitations 72
8 Conclusions 75
9 Future work 77
10 Other scientific contributions 79
11 References 83

1 Introduction

Why is it important to know how the heart works? While I have heard this question many times, I never personally felt the need for a detailed answer. Simply, I thought it was important because humans are curious about nature and want to know how things work. After some time, however, I realized that this was not a good enough reason for many others in the field of applied clinical sciences and I looked for more structured answers. I found out that there are plenty of reasons to be interested in knowing about how the heart works. We cannot recognize faults, or repair or improve a system if we do not know how it works. We would never repair a car if we did not know how it functions in the first place. Just looking at the differences between a well-functioning car and a poorly-functioning car will not necessarily help us to know how to repair it. How can we properly diagnose cardiovascular disease if we do not know what to measure, why we measure it and what a specific index means? This is why we still need to perform basic research on the heart and the cardiovascular system, that is, so that we can reduce the negative effects of cardiovascular disease, which remains the main cause of death in the world [1]. This goal is challenging because the heart and the vascular tree form a complex system whose behavior might be difficult to predict. Nevertheless, integrated knowledge of biology, chemistry and physics can help us to explore and understand the main functioning mechanisms of this important and fascinating system.

Mathematical models of hemodynamics were introduced as early as in the 19th century and were used to explain the arterial blood pressure wave form over time. An example of such models is the mathematical formulation of the Windkessel effect formalized by Otto Frank [2]. Frank's model was particularly useful in explaining the blood pressure decay during diastole [3]. Decades later, the advent of numerical simulations made it possible to solve the model's governing equation in an automatic manner [4], which increased the model's usability and complexity. Nowadays, many different models of the cardiovascular system are used to understand physiological and pathological processes, complementing the information provided by medical imaging and that acquired through other noninvasive means. This has shown to be very useful in both diagnostics and treatment planning [5]. Furthermore, modeling and simulations are also a valuable educational tool [6,7]. In the future, one goal is to use simulations of hemodynamics as a decision-making aid in clinical diagnostics and therapeutics. To date, several advanced cardiovascular models have been developed for multiple purposes [7–12]. However, some features of cardiac pumping such as the longitudinal movements in the atrioventricular (AV) region [13,14] are not often included in cardiac models. Modeling these features of cardiac pumping would improve the capability of the models to correctly reproduce cardiac physiology. Additionally, modeling could be used to understand clinical data related to physiological processes such as cardiovascular aging.

The use of medical imaging has substantially changed medical diagnostics and treatments. In fact, the currently available technology gives us the possibility to obtain images of the interior structures of the human body without invasive interventions. Medical images primarily show the anatomy or motion patterns of different organs, and are often obtained using ultrasound imaging, magnetic resonance imaging (MRI) and computer tomography (CT). In recent decades, many imaging techniques have also aimed at capturing the organs' functions, for example, using images obtained with positron emission tomography (PET) or functional MRI (fMRI). Specifically, PET images show tissues' metabolic activity and fMRI images show regions of brain activity by identifying the areas of the brain with higher blood flow. In order to provide clinically useful information, new and ingenious uses of medical imaging techniques are being suggested and developed. Among these, elastography is an emerging and fast-growing field of medical imaging that aims at providing clinicians with a tool for characterizing tissues' mechanical properties [15]. For centuries, clinicians have used manual palpation to feel abnormalities in the body, since healthy and pathological tissues often have different stiffness values. However, palpation is highly subjective and cannot be applied deep in the body. Elastography aims at substituting the palpation technique by providing quantitative measurements of tissue stiffness. Among other clinical applications, elastography offers many exciting possibilities in the cardiovascular field, where it could be used to assess arterial [16–21] and myocardial stiffness [22–24]. Nevertheless, further technique development and validation is needed before applying cardiovascular elastography in clinical routines.

This thesis, titled "*Imaging and modeling the cardiovascular system*," aims at using engineering tools, such as modeling of hemodynamics and elastography to better understand the cardiovascular system and to measure indexes that are relevant for the early diagnosis of cardiovascular disease. The specific motivation for each of the four studies presented in this thesis will be described in the following section. These motivations are tightly connected to the aims of the studies, as stated in Chapter 2.

1.1 Motivations

Study I — Clinical imaging and scientific studies have proven that the heart pumps by means of minor outer volume changes and back-and-forth longitudinal movements in the AV region [13,14]. The magnitude of AV-plane displacement has also been shown to be a reliable index for diagnosis of heart failure [25,26]. Despite this, AV-plane displacement is usually omitted in cardiovascular modeling.

Study II — Mechanisms involved in diastolic filling are not fully understood and are an active area of research [27–32]. Hydraulic forces have been previously hypothesized to contribute to diastolic filling [33–35]. To generate a net hydraulic force in the apex-to-base direction, a difference in short-axis area between the left atrium (LA) and the left ventricle (LV) is required. However, *in vivo* assessment and comparison of the LA and LV short-axis areas is missing from the literature.

Study III Increases/decreases in blood pressure with age are commonly explained by changes in the arterial system alone [36]. However, changes in arterial stiffness and vascular resistance that result in a systolic pressure increase induce ventricular remodeling, consequently affecting cardiac structure and function [37–39]. Cardiac hypertrophy resulting from these arterial changes is widely recognized and reported; however, the effects of the hypertrophy on blood pressure during aging have not been systematically quantified.

Study IV An increase in arterial stiffness is an important risk factor for cardiovascular events, as can be predicted and understood by mechanical and hemodynamic principles [36] and demonstrated by numerous clinical studies [40–42]. The ultrasound-based technique shear wave elastography (SWE) has been suggested for quantitative measurements of local arterial stiffness at multiple times during the cardiac cycle [16,17]. However, the accuracy of arterial SWE compared with an independent reference method has not been assessed.

1.2 Thesis outline

The thesis is divided into 11 chapters. After this short introduction, where the motivation for the thesis work is explained, the aims are presented in Chapter 2. Chapter 3 includes references to the four publications on which this thesis is based and statements about the contributions of the different authors to each study. Chapter 4 gives an overview of the background needed to understand the work presented in the thesis. Specifically, this chapter introduces the reader to cardiovascular physiology and the general principles of cardiovascular modeling and imaging. I wish to recommend the reading of the sections about the heart, even to the expert reader, because some key aspects of cardiac pumping that are omitted in many physiology books will be described. The methodologies used and the contributions made to this specific thesis work are described in Chapter 5. The main results are presented in Chapter 6 and discussed in Chapter 7. The main conclusions and suggested future work are presented in Chapters 8 and 9, respectively. Chapter 10 includes a list of other scientific contributions that are not presented in this thesis. The references are listed in the last chapter. Finally, the full versions of the publications are provided in the appendix.

2 Aims

The general aim of this thesis was to improve our understanding of cardiac function and cardiovascular aging, and to develop methods for the early detection of atherosclerosis. Both computer simulations and medical imaging were used to reach this goal. The specific aim for each study was as follows:

Study I — To develop a cardiac model based on the pumping action generated by the longitudinal movements of the AV plane.

Study II — First, to construct a physical model of the left ventricle and left atrium showing the action of hydraulic forces in ventricular filling. Second, to assess the presence of the anatomical basis needed to generate hydraulic-forces in healthy individuals by measuring left atrial and left ventricular short-axis areas with MRI.

Study III — To quantify the contribution of the heart and the arterial system to blood pressure changes during normal aging by using a validated lumped-parameter model and comparing simulation results with population data.

Study IV — To develop in-house software and experimental setup for arterial SWE measurements, and to assess the accuracy of the technique by comparison with mechanical testing in arterial phantoms.

3 Included publications

3.1 List of publications

The thesis is based on the four publications below. The publication and the corresponding study will be referred to in this thesis by their Roman numerals. The publications in their full format are attached as appendixes at the end of the thesis.

I. Modeling the heart with the atrioventricular plane as a piston unit. **E. Maksuti**, A. Bjällmark, M. Broomé. *Medical Engineering & Physics*, vol. 37, p. 87–92, 2015.

II. Hydraulic forces contribute to left ventricular diastolic filling. **E. Maksuti**, M. Carlsson, H. Arheden. S.J. Kovács, M. Broomé, M. Ugander. *Scientific Reports*, 2016. *Under review*.

III. Contribution of the arterial system and the heart to blood pressure during normal aging – a simulation study. **E. Maksuti**, N. Westerhof, B. Westerhof, M. Broomé, N. Stergiopulos. PLoS ONE 11(6):e0157493, 2016.

IV. Arterial stiffness estimation by shear wave elastography: validation in phantoms with mechanical testing. **E. Maksuti**, E. Widman, D. Larsson, M. W. Urban, M. Larsson, A. Bjällmark. *Ultrasound in Medicine & Biology*, vol. 42, p. 309–321, 2016.

3.2 Division of work between authors

I. **EM** implemented the model and ran the simulations. **EM**, AB and MB participated in the study design. **EM** drafted the manuscript. AB and MB further contributed to the manuscript. All authors approved the final manuscript.

II. All authors contributed to the design of the study. MC and MU conducted the data acquisition. **EM**, MC and MU participated in the data analysis. **EM** performed the statistical analysis. All authors interpreted the results. **EM** drafted the manuscript. MU and MB further contributed to the manuscript. All authors reviewed and approved the final manuscript.

III. NW, BEW and NS conceived and designed the study. **EM** implemented the model and run the simulations. All authors analyzed the data. **EM** drafted the manuscript. NW and BEW further contributed to the manuscript. MB and NS reviewed the manuscript. All authors approved the final manuscript.

IV. **EM**, EW, ML and AB participated in the initiation and design of the study.

EM and EW participated in the software development. DL participated in the mechanical testing design and further contributed to the main study design. **EM** and DL performed the experiments and analyzed the data. **EM** performed the statistical analysis. All authors interpreted the results. **EM** drafted the manuscript. DL, EW and AB further contributed to the manuscript. ML and MWU reviewed the manuscript. All authors approved the final manuscript.

4 Background

4.1 Cardiovascular physiology

4.1.1 The heart

Incredibly enough, there is a muscular organ in our body that incessantly contracts and relaxes with no rest during our entire lifetime: the heart. This essential organ serves a major function, i.e. it enables the circulation of blood within the closed cardiovascular-system loop. The blood is the carrier of all vital substances that organs, tissues and single cells need. Among these substances we can find nutrients, oxygen and signaling molecules that behave as messengers and convey information between different parts of the body. The blood also carries carbon dioxide and waste products to their elimination points. Without the blood's continuous circulation, no organ of the body could perform its tasks and no dangerous substance could be expelled.

The human heart is located in the middle of the chest (Figure 4.1), behind the sternum and slightly shifted to the left. It is approximately the size of a clenched fist and normally weighs between 148 to 296 g in women [43] and from 233 to 383 g in men [44]. The tip of the heart is called the apex and the region of the heart opposite the apex is called the base. The base represents the upper border of the heart and includes the left atrium, part of the right atrium, and the proximal portions of the great vessels. Neither the apex nor the base moves to a large extent during the heart cycle [14].

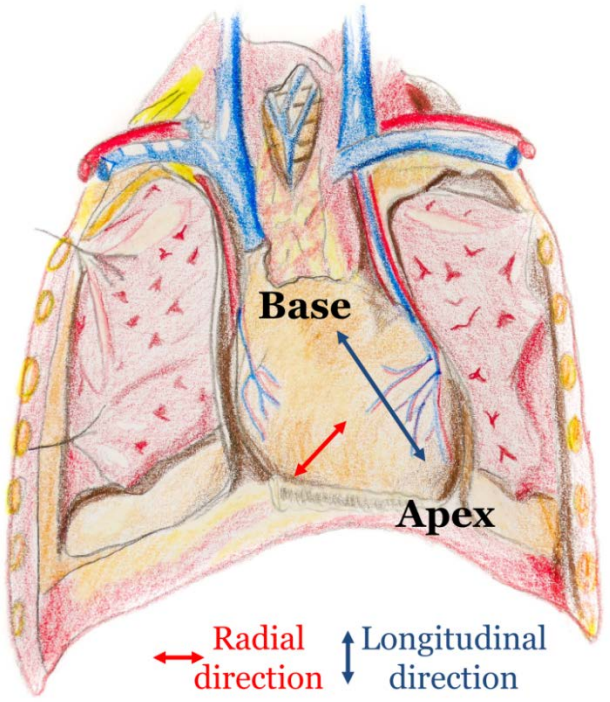

Figure 4.1 – Overview of the heart's anatomy and surrounding structures *in situ*. The heart is enclosed in the pericardium, leans against the diaphragm, is surrounded by the lungs and protected by the rib cage. The base and the apex of the heart do not move to a large extent during the cardiac cycle.
Author's own drawing

As can be seen in Figure 4.1, the heart is surrounded by a fibrous double-walled sac, called the pericardium, and many other structures, such as the lungs, the diaphragm, the sternum and the ribs. The movements of the heart are largely limited by these surrounding tissues and structures. However, some directions of motion are facilitated by the

pericardium itself. In fact, between the pericardial layers there is a cavity (the pericardial space in Figure 4.2), where pericardial fluid is secreted and acts as a lubricant. The pericardial fluid secretion allows the epicardium to glide along the pericardium with minor energy losses [45,46]. The heart is organized into two separated, but interconnected sides functioning at different pressure levels, as shown in Figure 4.3. The left side of the heart pumps blood into the systemic circulation, which reaches the entire body and requires high pressures to overcome losses throughout its widely spread network. The pressure loss occurs in particular at the level of the small resistance arteries, which contract and dilate to regulate and direct blood flow to different organs. The right side of the heart pumps blood into the pulmonary circulation, which reaches only the lungs and has a vascular resistance of an order of magnitude lower than the systemic circulation. Consequently, the pulmonary circulation requires lower pressure levels. The interventricular septum regulates the balance in flow and pressure between the right and left sides of the heart [33,47].

Each side of the heart is divided into two chambers: the atrium and the ventricle. Four valves allow one-directional flow between the atria and the ventricles and between the ventricles and the large arteries. The four valves are surrounded by stiff, dense connective tissue and all are located in the same region, which is commonly referred to as the atrioventricular (AV) plane. An overview of the AV plane viewed from above is shown in Figure 4.4. The aforementioned anatomical considerations are fundamental to understanding the pumping and filling function of the heart, which has been debated for centuries and still is [27,29,33,48–52].

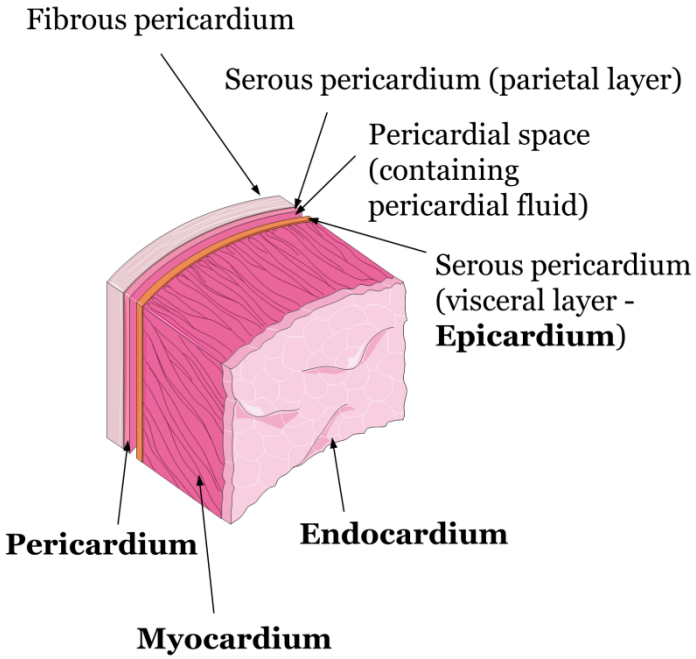

Figure 4.2 – Schematic representation of the different layers of the cardiac muscle and the surrounding pericardial sac.
Images modified and used with permission from Servier Medical Art – Creative Commons Attribution 3.0 Unported License.

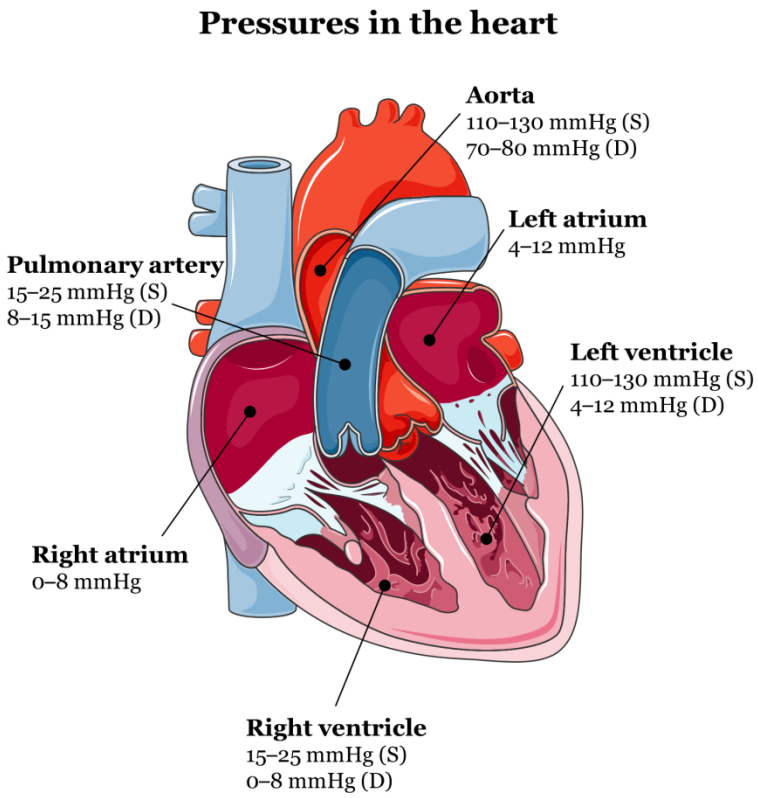

Figure 4.3 – Schematic representation of the four chambers of the heart with the corresponding pressure levels during systole (S) and diastole (D).
Images modified and used with permission from Servier Medical Art – Creative Commons Attribution 3.0 Unported License.

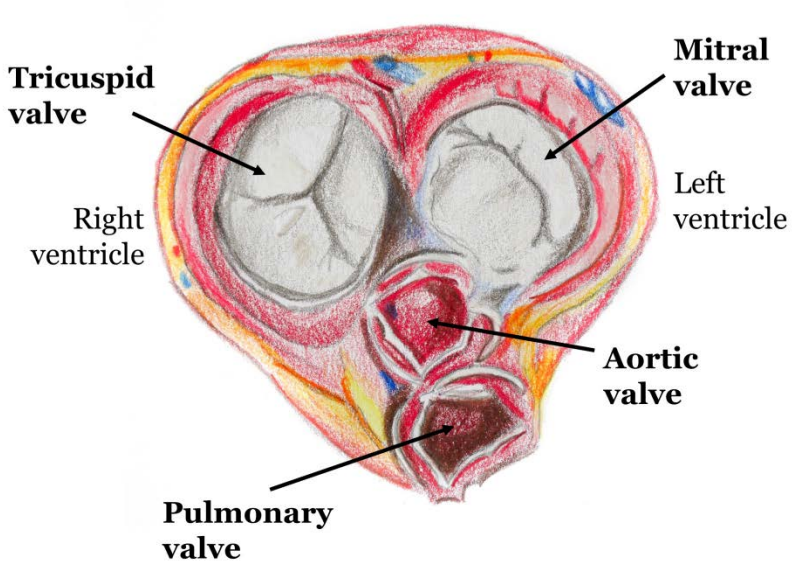

Figure 4.4 – Drawing of the AV plane and the four cardiac valves seen from above, having removed the atria.
Author's own drawing

Closed-chest versus open-chest cardiac pumping

The heart has a complex motion pattern, which is often described by dividing it into components along different directions (Figure 4.1). The longitudinal direction corresponds to the apex–base direction, the radial direction is perpendicular to this and the circumferential direction corresponds to the rotation around the apex-to-base axis. The motion pattern and the pumping mechanism of the heart are different in the closed-chest and in the open-chest scenario (Figure 4.5). This is because of the presence or absence of the pericardium and the surrounding tissues. The pericardium can be compared to a plastic bag, i.e. flexible but stiff. This sac significantly limits the heart's total volume [53]. To confirm this, studies based on MRI have shown that the total heart volume variation during the heart cycle is in the range 5–11% [13]. These findings oppose the theory that the heart pumps by a squeezing mechanism in the radial direction (Figure 4.5), which would require large volume changes, and instead suggest a longitudinal piston-like mechanism, where internal reciprocal redistribution of blood volume between the atria and the ventricle is caused by the longitudinal motion of the AV plane while preserving the total heart volume [14,54]. This mechanism was colorfully described in 1964 by Rushmer, who compared the ventricular ejection pattern as closer to "striking a piston with a mallet than squeezing an orange or milking a cow" [52]. Nowadays, the movement patterns of the heart are clearly visible in medical images (see Figure 4.12 and Figure 4.15 in section 4.3).

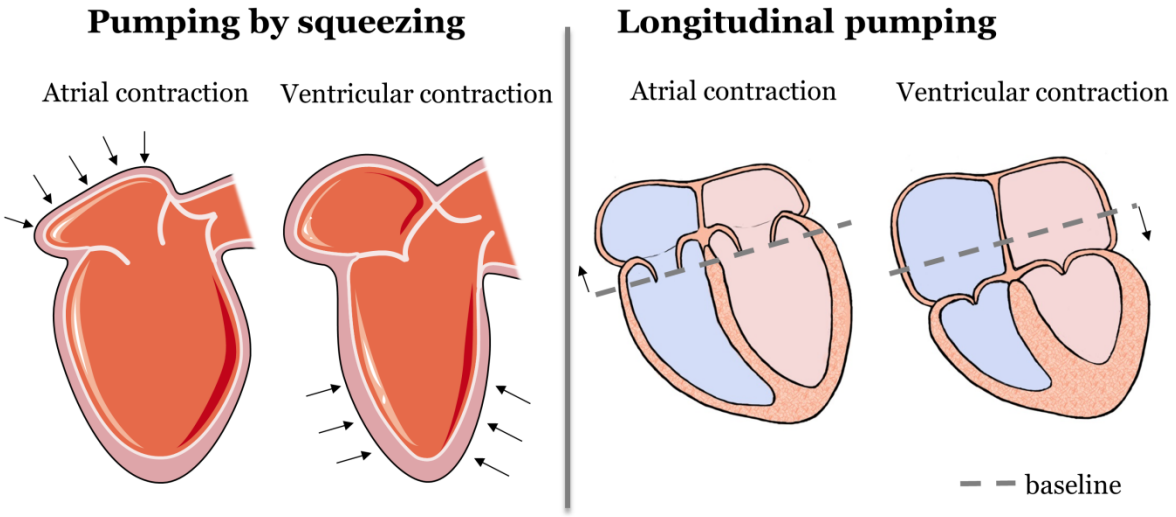

Figure 4.5 – Comparison between the heart's traditionally described squeezing mechanism (left panel) and the actual pumping mechanism by longitudinal piston-like motion seen in medical images (right panel). Constraints imposed by the pericardium and the tissues and organs surrounding the heart do not allow large volume changes. Therefore, the pumping action is carried out by longitudinal movements of the AV plane and reciprocal volume changes between the atria and the ventricles. The squeezing mechanism can be seen in open-heart surgery, when the chest is open and the pericardium is cut; thus, constraints preventing large volume changes are no longer present.

Left panel image modified and used with permission from Servier Medical Art – Creative Commons Attribution 3.0 Unported License.

However, the heart is also capable of working as a squeezing pump, as can be observed in open-heart surgery, when the chest is open and the pericardium cut. These surgical observations might be the reason for the common misunderstanding of the cardiac pumping action. In addition, experiments have shown that the pericardium alters both systolic and diastolic function [46,55] and therefore there is a difference between closed-chest and open-chest cardiac function.

The cardiac cycle

The heart cycle is divided into two main phases: systole and diastole. During systole, the ventricles contract and pump blood into the arteries. During diastole, the ventricles relax and fill with blood to be ejected during the subsequent heartbeat. These two main phases can be further divided into additional phases that better describe and characterize cardiac function, e.g. for diagnostic purposes. The exact definition of the cardiac phases may differ between different studies, depending on the methodology used to characterize cardiac function. In this section, six main phases will be described with a focus on the main events occurring during each phase. Using the ventricles as a reference, the mitral and tricuspid valves will be referred to as inflow valves and the aortic and pulmonary valves will be referred to as outflow valves. The sequence of events that occurs during the cardiac cycle can be seen in medical images, such as those acquired with MRI; see section 4.3.2 for details.

Atrial contraction. The atrial myocardium contracts, emptying the atrial appendages and pulling the AV plane toward the base. During this phase, the inflow valves are open and there is flow from the atria to the ventricles. The outflow valves are closed.

Isovolumetric contraction. This is the transition phase that occurs between atrial and ventricular contraction. The inflow valves are closed and no changes in ventricular volume occur during this phase, since the outlet valves are also closed. The R wave of the electrocardiogram occurs during this phase.

Ventricular contraction (ejection). The ventricular muscles contract and pull the AV plane toward the apex. The motion of the AV plane pushes the blood toward the arteries in a piston-like fashion. The pressure in the ventricles increases and when it exceeds the arterial pressures, the outflow valves open. The inflow valves are closed during this phase. The motion of the AV plane toward the base increases the atrial volume, which has the effect of sucking blood from the veins to the atria [54]. The ejection ends when the outflow valves close and the AV plane stops moving.

Isovolumetric relaxation. This is the transition phase that occurs at the end of ventricular contraction. Both inlet and outlet valves are closed during this phase and no ventricular volume changes occur. The ventricular myocardium begins to relax and the AV plane starts to move back toward the base. The pressure in the ventricle starts to decrease.

Rapid filling. When the pressure in the atria exceeds the ventricular pressure, the inlet valves open and rapid filling begins. The blood accumulated in the atria flows rapidly through the inlet valves and is redistributed in the ventricles, causing the AV plane to move toward the base. In this phase the muscles are relaxed, the outlet valves are closed and the

AV plane is free to move. Since the inlet valves are open, the pressure in the atria and in the ventricles is approximately the same.

Diastasis (slow filling). After the rapid filling, the ventricles continue to fill slowly until they reach their maximum volume during that specific heart cycle. In this phase, the AV plane is slowly moving toward the base, or is static in the longitudinal direction and expands in the radial direction. During this phase, the incoming blood from the veins might also flow to the atrial appendages instead of to the ventricle. The appendages serve as an extra reservoir for blood.

Forces acting during ventricular ejection and filling

Ventricular ejection. To eject blood from the ventricles to the arteries, the cardiac muscle fibers in the myocardium contract in an organized manner in response to an electrical stimulus that is converted to a mechanical force. The contraction mechanism is similar to what happens in skeletal muscles, with the difference being that cardiac muscle fibers cannot be controlled voluntarily and have a more advanced intracellular calcium handling system, with ions released from the sarcoplasmic reticulum in a process called calcium-induced calcium release [56]. When the intracellular calcium concentration is sufficiently high, calcium ions bind to the protein troponin, which in turn allows myosin to bind to actin and contraction to occur. The additional release of intracellular calcium prolongs the duration of the action potential from approximately 5 ms (typical duration for skeletal muscle) to 200–300 ms. The duration of the action potential is tightly related to the duration of the contraction [57]. Within physiological conditions, cardiac muscle contraction is tireless.

Ventricular filling. During contraction, potential energy is accumulated and stored within the myocardium [31,50], pericardium [58,59] and surrounding tissues, and forcefully released at the onset of diastole. This mechanism is often referred to as elastic recoil [32,60], and is driven by a restoring force [28,31]. At the end of contraction, calcium ions are pumped back into the sarcoplasmic reticulum, which allows the actin and myosin filaments to uncouple and to slide back to their resting positions. This process is energy consuming and is therefore called active relaxation. While active relaxation takes place, there are still actin–myosin bonds left that cause residual tension within the myocardium and prevent it from fully relaxing. The active relaxation duration is often characterized by a time constant that might be more or less prolonged depending on age and pathology [29]. Restoring forces and active relaxation act simultaneously. Specifically, incomplete relaxation partially opposes filling until the myocardium is fully relaxed and the release of restoring forces allows the ventricle to expand.

In addition to these two mechanisms, hydraulic forces have been hypothesized to contribute to diastolic filling and will be further discussed in this thesis (section 5.1.1 and 5.2).

Cardiac regulatory function

The intensity of the force generated by the contraction is regulated by the Frank–Starling mechanism, which was described by Otto Frank and Ernest Starling based on their own experiments and previous work by Dario Maestrini [57,61,62]. This mechanism, sometimes

referred to as “the law of the heart”, implies that the more each myocyte in the cardiac muscle is stretched during filling, the stronger the contraction will be. This law is of high importance as it can explain how the heart is capable of pumping out all the blood that comes into it, preventing blood from being dammed in the veins. Namely, within physiological limits, the heart can be considered as an inflow-controlled pump, where all blood that comes in is pumped out. Another hypothesis that could explain the regulatory function of the heart is related to the heart’s own macroscopic shape and anatomy [33]. To prove this hypothesis, an artificial pump with a small flexible chamber (representing the atrium) and a large flexible chamber (representing the ventricle) was constructed and tested. It showed continuous inflow, pulsating outflow and high sensitivity to filling pressure, and as such was similar to the human heart [63]. Despite this proof-of-concept, translational studies are still needed to confirm that the heart’s shape significantly influences its own regulation of the filling volume. Such studies could deepen our understanding of the heart’s regulatory mechanisms.

4.1.2 The arteries

The circulatory system has the task of transporting blood to all organs and cells in the body, similarly to how a hydraulic network transports water to different locations. The first part of the circulation is constituted by arteries, which are large and elastic pipes that can dilate and constrict to accommodate varying volumes of blood pumped by the heart. Arteries are defined as those vessels that transport blood away from the heart. They transport oxygenated blood in the systemic circulation and deoxygenated blood in the pulmonary circulation. A schematic representation of the systemic arterial system is shown in Figure 4.6. The first large artery connected to the left ventricle is the aorta. This large artery branches into smaller arteries, which branch into arterioles later in the network and finally branch into capillaries. The oxygen and nutrients transfer occurs at the capillary level. After this transfer has occurred, capillaries merge together to create venules, which merge into veins. The veins are the vessels that come back to the heart. Veins accommodate the largest part of the total blood volume. Another difference from the arteries is that veins work at low pressures.

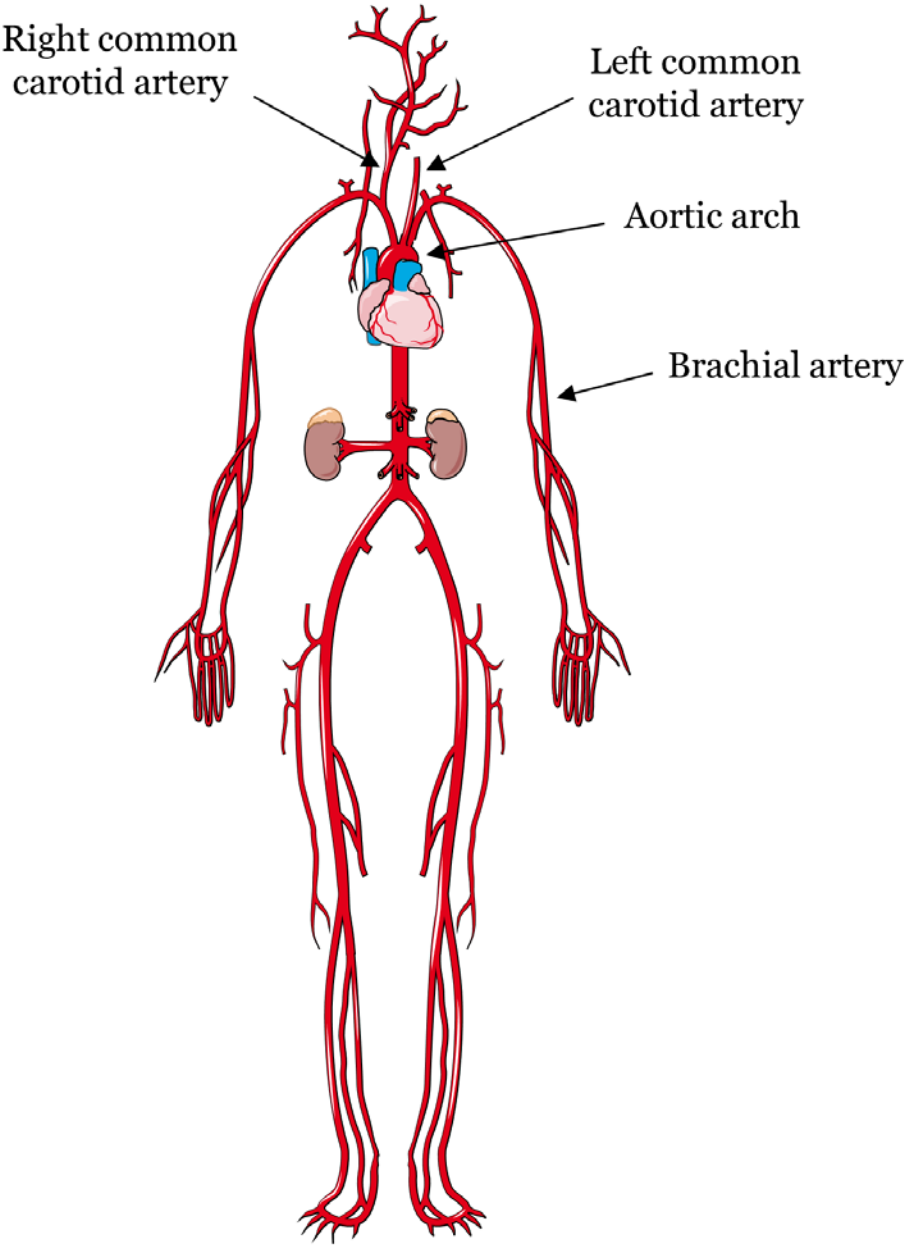

Figure 4.6 – Overview of the systemic arterial system. The most relevant arteries to this thesis work are indicated.
Image modified and used with permission from Servier Medical Art – Creative Commons Attribution 3.0 Unported License.

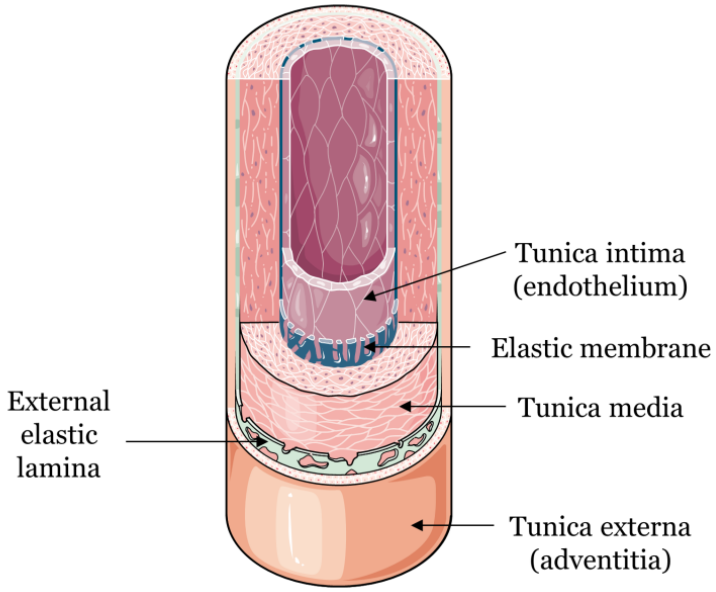

Figure 4.7 – Overview of the different layers of the arterial wall.
Image modified and used with permission from Servier Medical Art – Creative Commons Attribution 3.0 Unported License.

The arterial system represents the load that the heart must overcome in order to eject blood. In particular, the arterial compliance (which is the inverse of stiffness) and arterial resistance are independent contributors to the systolic and diastolic pressure [64]. The arterial compliance is mainly located in large arteries [65], whereas resistance is the major feature of the smallest arteries [66]. Arteries should have the ability to withstand high pressures and at the same time be compliant so as to not excessively tire the heart. Consequently, an increase in arterial stiffness can have negative consequences for the functioning of the cardiovascular system. To be able to meet all these demands, the arterial wall has a complex structure made up of different layers, as illustrated in Figure 4.7.

4.1.3 Arterial–cardiac interaction

The heart and the arterial system are tightly interconnected and influence each other's function. The interaction between the heart and the arterial system has been studied extensively and is often referred to as arterial–cardiac interaction or ventricular–arterial coupling [67,68]. An effective way to characterize cardiac mechanics and hemodynamics is by means of pressure–volume diagrams of the left ventricle. These diagrams provide a large amount of information about left ventricular pumping, filling and ventricular–arterial coupling in a compact and efficient way. However, a relevant piece of information that is missing in the pressure–volume loops is the time variable. The interested reader is referred to useful guides by Burkoff *et al.* [69] and Westerhof *et al.* [70] for further reading on the topic.

During aging, structural changes occur in the arterial system mainly because of the replacement in the arterial wall of elastin fibers by collagen fibers. This process produces an increase in arterial stiffness that affects blood pressure [36]. More specifically, these

changes in arterial stiffness result in a systolic pressure increase and a diastolic pressure decrease. Stiffer arteries demand more work from the heart, which is demonstrated by the fact that a systolic pressure increase induces ventricular hypertrophy [37–39]. These consideration show that the arterial–cardiac interaction is particularly important during aging and in pathological conditions such as hypertension, as the properties of both the heart and the arterial tree change with age and pathology [36,38,71–73].

4.2 Modeling cardiovascular hemodynamics

Due to the complexity of the cardiovascular system, it is not always possible to understand the role played by each part of the system. Modeling and simulation can therefore be a useful tool to assess how the system is influenced by a change in a single part of the system as well as by a combination of multiple changes. The heart and the circulatory system are physical systems governed by energy and mass conservation laws, as is true for any other physical system, and can therefore be studied and modeled using an engineering approach.

A system composed of interacting parts can be defined as an entity separable from the rest of the environment in which it is integrated [74]. Any system that changes status with time is called a dynamical system and its dynamics are described by variables. Each component of the system has properties that can be quantified by parameters, usually constant values. More precisely, a parameter is a measurable factor that modulates the impact that a specific component has on the system's dynamics. Despite being a measurable factor, it is often very challenging to measure the cardiovascular system's parameters *in vivo*. Therefore, parameter values such as inertia to flow, arterial compliance and resistance to flow can only be estimated by indirect measurements or by calculations based on theoretical assumptions.

4.2.1 Classification of models

Every model is a simplified representation of reality and can only describe part of the real system's behavior. For these reasons, each model is designed with a specific purpose and level of abstraction. Models of the cardiovascular system can be classified into three major groups:

- Lumped-parameter or 0D models.
- Wave transmission or 1D models.
- Finite element or 3D models.

Lumped-parameter models do not take the geometry of the cardiovascular system into account and each component of the model is considered as a point. Therefore, pressure and flow variables are expressed by mathematical equations as a function of time and relevant parameters, but not as spatial coordinates. One advantage of lumped-parameter models is that they are computationally efficient and allow real-time simulations of the entire cardiovascular system [10].

Wave transmission models are based on transmission line theory and are used to model the vascular system [11,75]. In such models, the vascular tree is divided into small segments and each segment has a specific geometry and specific mechanical properties.

These 1D models are capable of reproducing wave transmission and reflection phenomena within the arterial tree, which is not possible with a lumped-parameter model made up of a single arterial compartment.

Finite element models are usually 3D models, where the geometry of the part of the cardiovascular system being investigated is taken into account. Such models are used to study detailed flow patterns in a segment of the arterial tree [76], or to simulate ventricular mechanics and hemodynamics [77]. These models have the advantage of taking the real geometry into account, but are computationally demanding and realistic boundary conditions are not easy to implement [78].

In this thesis, the focus will be on lumped-parameter models, in particular the time-varying elastance of the left ventricle [79], the Windkessel models of the arterial tree [80] and novel lumped-parameter models [81], as they require a limited number of parameters and can be used to model the global behavior of the cardiovascular system.

4.2.2 Time-varying elastance model of cardiac contraction

The time-varying elastance *E(t)* is defined as

$$E(t) = \frac{p(t)}{v(t) - V_0} \tag{4.1}$$

where *p(t)* and *v(t)* are the pressure and volume, respectively, of the left ventricular cavity throughout the cardiac cycle, and V_o indicates the minimum filling volume required before the ventricle can generate any pressure and is assumed constant. The elastance is therefore tightly related to the pressure–volume loop, since it represents the slope of the line connecting each point of the loop to V_0 [69]. Elastance is a measure of chamber stiffness and is therefore the inverse of chamber compliance. Experimental measurements of pressure and volume in the left ventricle have shown that the shape of the time-varying elastance is similar in different subjects, both in normal physiology and pathological conditions [82]. The maximum value of the elastance function is a load-independent measure of contractility and the minimum value is related to passive chamber stiffness. For these reasons, a predefined elastance function is often used as an input to 0D cardiovascular models [8,10,83]. Using the elastance function does not give insights into the intrinsic pumping mechanism of the heart, but the method reproduces cardiac hemodynamics well and is computationally efficient.

4.2.3 The Windkessel model

The Windkessel model is a lumped-parameter model of the arterial tree and can be made up of two, three or four elements [3] as shown in Figure 4.8.

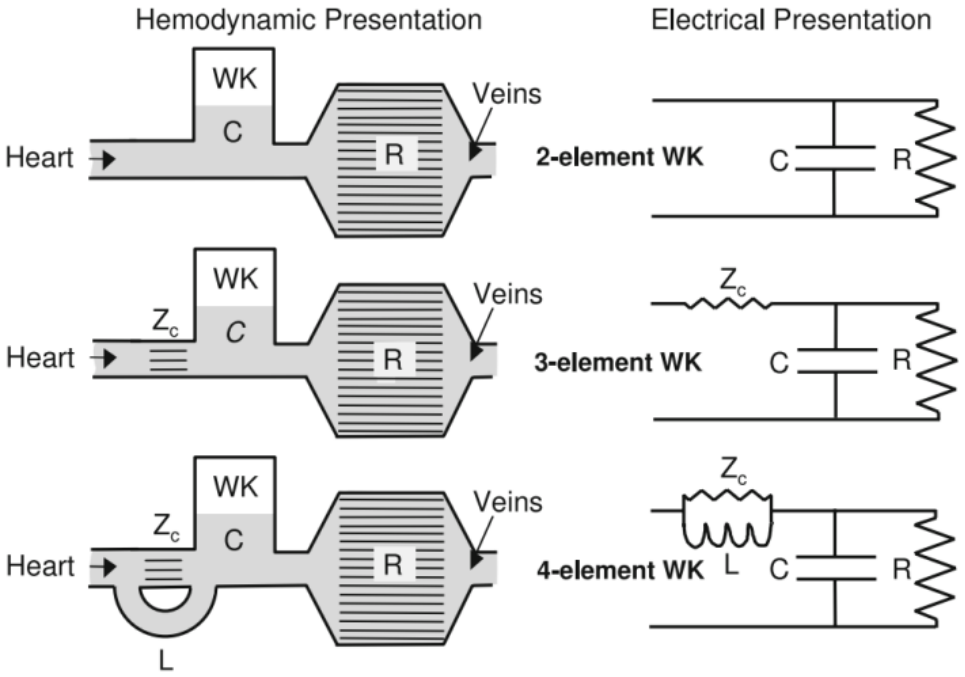

Figure 4.8 – Hemodynamic and electrical representation of the two-, three- and four-element Windkessel model of the arterial tree. The Windkessel model is a lumped-parameter model and returns as output aortic flow and pressure over the cardiac cycle. WK = Windkessel; C = compliance; R = resistance; Zc = characteristic impedance; L = inertance.
Reproduced with permission from [3] *under the Creative Commons Attribution Noncommercial License.*

The two elements that give the most significant contribution to aortic pressure and flow are the total arterial compliance (inverse of elastance), which is related to the stiffness of the arterial system, and the vascular resistance, which is defined as

$$R = \frac{\Delta P}{Q} \tag{4.2}$$

where ΔP is the mean pressure drop caused by the arterial segment and Q is the mean flow through the segment. Vascular resistance therefore represents the pressure losses in the system, given a certain flow. The additional third element is the characteristic impedance of the proximal aorta, which together with the other two elements better reproduces the fast pressure and flow changes of the arterial pulse. The fourth element is the inertance, which is related to the inertia of the blood.

4.2.4 Modeling by bond graphs

In 1959, Paynter suggested the use of the bond graph notation in system dynamics modeling as a unified representation for all physical domains [84]. Bond graphs are a graphical tool based on energy and information flow that can describe complex systems through a small set of ideal elements. The use of ideal standard elements is similar to what is done in electrical engineering when drawing circuits that use capacitors, resistors,

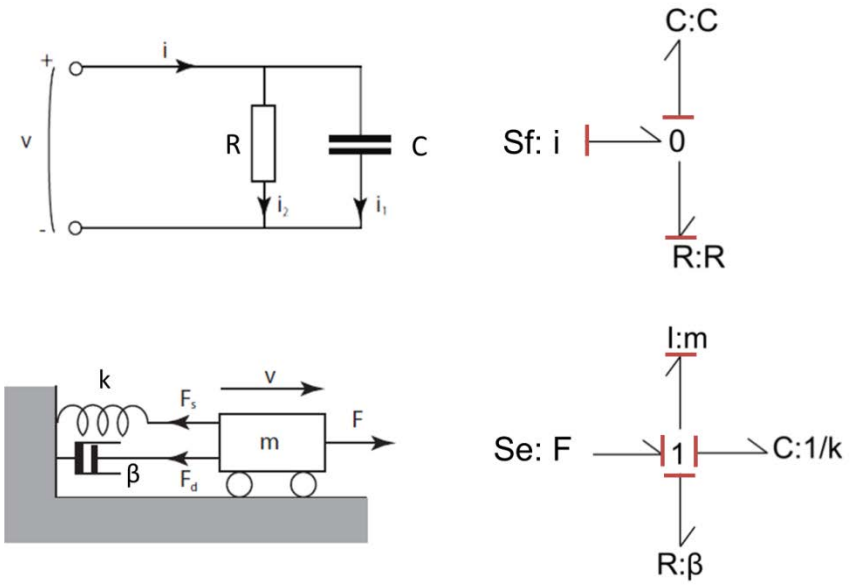

Figure 4.9 – Example of an electrical system and a mechanical system and their equivalent bond graph models. With bond graphs, the same set of symbols is used for both physical domains. The red dashes in the bond graph model indicate the direction of causality (see main text for details). R = resistance; C = capacitance; i = current; v = voltage/velocity; Sf = flow source; Se = effort source; k = spring constant, m = mass; β = damping coefficient, F = force.

inductors, sources and other elements. The main difference introduced with the bond graph notation is that it can be used independently from the application domain, e.g. mechanical, hydraulic or electrical. Since the cardiovascular system is a multidomain system, the use of bond graphs avoids the abstraction of equivalent electrical circuits.

In the bond graph notation, a bond represents the flow of power between two different parts of the system. The bond is drawn as a half-arrow and the tip of the bond indicates the direction of positive power flow. The power is always given by the product of two variables, effort (e.g. pressure or force) and flow (e.g. volumetric flow or velocity). There are seven main elements that can exchange power among themselves: the R-element, the C-element, the I-element, the effort source (Se), the flow source (Sf), the transformer element (TF) and the gyrator element (GY). These elements can be connected through two kinds of junctions. The 1-junction is used when the flow variable is the same in all elements connected to the junction, similar to electrical components connected in series. The 0-junction is used when the effort variable is the same in all elements connected to the junction, similar to electrical components connected in parallel. Two examples of mechanical and electrical systems with their equivalent bond graph models are shown in Figure 4.9. In a bond graph scheme, causality is also shown (red dashes in Figure 4.9). The causality sign is located close to those elements that dictate the flow variable to the rest of the system. For example, a flow source will induce the flow (e.g. volumetric flow) in the system and at the same time experience the effort (e.g. pressure) that the system is imposing back on it. Since a single component can only dictate either flow or effort, the elements that do not have a causality sign close to them will dictate the effort. This implies that once the bond graph scheme is drawn, it clearly shows inconsistencies in the system that might otherwise remain hidden.

These inconsistencies could for example bring to light algebraic loops, i.e. endless substitutions of the system equations. Bond graphs and causality can show this problem, well before equations are derived [74]. In addition, the notation is suitable for deriving differential equations by iteratively applying a predefined procedure. For a more detailed explanation of the use and applications of bond graphs, the reader is referred to the books by Karnopp [74] and Cellier [85].

Simulations in Dymola

A general bond graph model can be implemented and run on the software platform Dymola, by means of the bond graph library [86]. Dymola is the software used in this thesis and is based on the object-oriented language Modelica and solves differential algebraic equations (DAEs) directly. DAEs, in contrast with ordinary differential equations (ODEs), are written in an implicit form, which means that input and output do not need to be defined a priori. The numerical method DASSL [87] implemented in Dymola can automatically convert the DAEs to ODEs. This allows simple models of the subsystems (ventricle, artery, etc.) to be created and then connected with each other without rewriting the new dynamic system equations.

4.3 Imaging the cardiovascular system

Medical imaging technology has substantially changed the way medicine is performed, as it enables clinicians and healthcare professionals to obtain an image of internal organs and structures of the human body that would not otherwise be visible without invasive interventions. In other words, current technology makes it possible to obtain images of arbitrary slices of the human body without actually cutting the body open. This might seem obvious nowadays, but for many centuries it was not possible [88]. The advent of medical imaging has enabled better and more precise diagnoses, follow-up of treatment and therapy [88,89]. On the other hand, the new technology has also increased complexity, shaped the hospital environment and increased costs for healthcare providers [88].

Many different imaging modalities are currently available. Each modality is based on a specific physical principle and has its advantages, disadvantages and range of applications. In this introduction and thesis, focus will be put on ultrasound imaging and MRI, since they do not make use of ionizing radiation and are therefore suitable for initial diagnoses and the screening of heathy volunteers in basic research.

4.3.1 Ultrasound imaging

The physical principle of ultrasound imaging is based on sending pressure waves and detecting their reflections at the boundary between different media. Sound is also a pressure wave, similarly to ultrasound. The only difference between the two is that ultrasound includes frequencies above 20 kHz, which are not audible to the human ear. When an ultrasound wave reaches the boundary between two media, e.g. two different organs, part of the wave continues to travel in the same direction and part of the wave is reflected, as shown in Figure 4.10. This reflected wave is detected and provides the basic information needed to reconstruct the image. Specifically, the speed of the ultrasound wave in soft tissues is known (~1500 m/s [90]) and therefore it is possible to calculate the

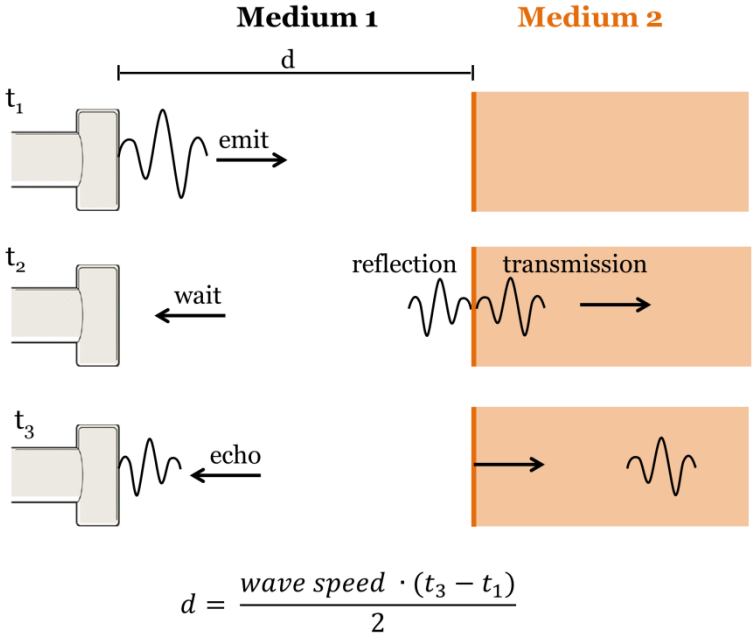

Figure 4.10 – Physical principle of ultrasound. A compression wave is emitted in medium 1 by the transducer at the time t_1. The wave travels forward until it reaches the interface with medium 2, where it is partially reflected and partially transmitted. The reflected wave (echo) is detected by the transducer and the distance between the transducer and the media interface can be calculated based on the time delay between the transmitted wave and the echo. d = distance; t = time.

Figure 4.11 – Illustration of a clinical ultrasound system.

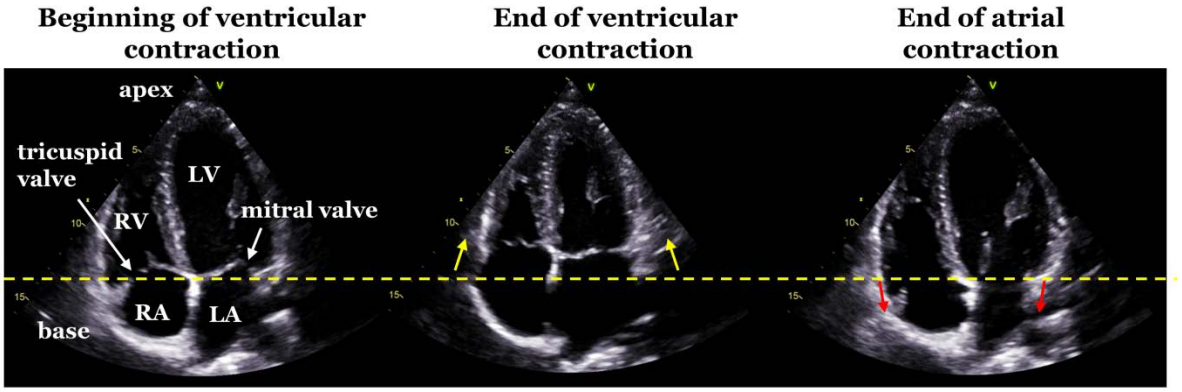

Figure 4.12 – Ultrasound images of the four cardiac chambers (commonly referred to as the 4-chamber view) at three different time points in the cardiac cycle. The apex of the heart is located on the top of the image. The dashed line indicates the position of the AV plane at the beginning of ventricular contraction. Note that the AV plane moves toward the apex during ventricular contraction (direction of the yellow arrows) and is pulled toward the base during atrial contraction (direction of the red arrows). LV = left ventricle; RV = right ventricle; LA = left atrium; RA = right atrium.

distance between the transducer and the media boundary by measuring the time delay between the transmitted wave and the received wave (Figure 4.10). The reflected wave is called the echo and therefore ultrasound imaging is sometimes referred to as echography. By repeating this procedure multiple times, it is possible to reconstruct an image where the borders between different organs and structures appear as white pixels and the regions where the ultrasound wave is not reflected appear as black pixels Figure 4.12. However, reflections from small scatters within the tissue have random amplitude and phase. When these reflections add together, they produce a random pattern in the image brightness called speckle. Despite being a random pattern that appears as noise in the image, the speckle signal is not purely random noise but is a specific pattern for each tissue region. An example of a cardiac ultrasound image at different phases of the cardiac cycle is shown in Figure 4.12, where the heart's pumping action, as explained in paragraph 4.1.1, can be clearly seen. One of the main advantages of ultrasound is the fast image acquisition time. In fact, with conventional ultrasound (different from ultrafast ultrasound imaging explained in section 4.3.4), it is possible to obtain up to 100 frames per second, depending on the penetration depth and width of the image. Another advantage of ultrasound is the cost efficiency of the examination because the device itself is less expensive than other imaging modalities such as MRI and computed tomography; in addition, it does not require a specific hospital room and it can be easily moved (Figure 4.11). The technique also has some disadvantages: images have relatively poor soft tissue contrast and are therefore not easy to interpret. For this reason, an experienced user is needed to perform an accurate diagnosis. Moreover, structures such as bones and lungs cannot easily be imaged because the ultrasound wave is highly reflected at the border between soft tissue and bone or air. Ultrasound imaging is widely used to image the fetus [91] and the heart [92]. Both applications involve soft tissue surrounded by a fluid, i.e. amniotic fluid or blood, conditions under which the ultrasound signal and contrast are particularly good. The high temporal resolution is also important for fast-moving organs such as the heart and even for the slower movements of the fetus.

4.3.2 Magnetic resonance imaging

MRI is based on nuclear magnetic resonance theory, according to which nuclei located in a magnetic field absorb and re-emit electromagnetic radiation. The human body is mainly constituted of water. Each hydrogen nucleus (proton) of the water molecules has an angular momentum (spin), which results in a magnetic momentum. Consequently, each proton behaves like a small magnet. Once these magnets are located in a strong magnetic field $\mathbf{B_0}$, they tend to align with $\mathbf{B_0}$ by *precessing* around it at a specific frequency named the Larmor frequency (Figure 4.13a). This results in a net magnetization $\mathbf{M_0}$. The net magnetization $\mathbf{M_0}$ is the signal needed to generate an image, but until it is aligned with the strong $\mathbf{B_0}$, it is impossible to measure. In fact, the intensity of $\mathbf{B_0}$ is 1.5−3 T in clinical scanners and from 4.7 up to 21 T in the small-animal scanners used in preclinical research [93]. To be able to measure the net magnetization of the tissue, a pulsed field $\mathbf{B_1}$ perpendicular to and rotating around $\mathbf{B_0}$ with frequencies close to the Larmor frequency, which is in the radiofrequency range, is used to modify the orientation of $\mathbf{M_0}$ and obtain a measurable signal (Figure 4.13b). After removing the pulsed field, the magnetization vector tends to align again along $\mathbf{B_0}$ and continues to precess around it, producing a signal that can be measured by antennas located on the patient's body. This process is called

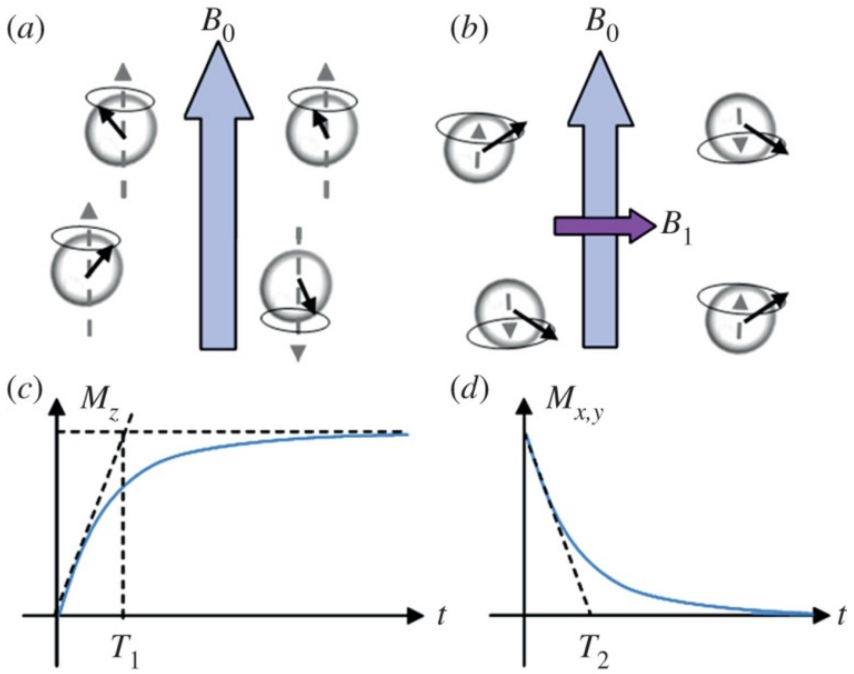

Figure 4.13 – Schematic representation of the MRI working principle.
(a) Water protons spin in a static magnetic field $\mathbf{B_0}$ and (b) after application of the radiofrequency-excitation $\mathbf{B_1}$. In (a) and (b), dashed gray arrows represent the M_z component of the magnetization field $\mathbf{M_0}$, and solid gray circles represent the $M_{x,y}$ component. (c) Restoration of M_z following an exponential law with time constant T_1. (d) Relaxation of $M_{x,y}$ following an exponential decay with time constant T_2.
Figure adapted from [94]. *Reproduced with permission.*

relaxation. The longitudinal component of $\mathbf{M_0}$ (Mz) is restored, according to an exponential law, with time constant T_1 (Figure 4.13c). The transverse component of $\mathbf{M_0}$ (Mxy) relaxes following an exponential decay with time constant T_2 (Figure 4.13d). Different soft tissues have different relaxation constants and can therefore be distinguished in MRI images. Protons are abundant in the human body, particularly in water and fat. For this reason, images obtained with MRI essentially map the location of water and fat in the body.

MRI has many advantages. It is a nonionizing technique with superior soft tissue contrast compared with CT and ultrasound. This makes it particularly suitable for imaging, e.g. the myocardium and the brain. With MRI, it is also possible to obtain images of any arbitrary plane in the human body. On the negative side, the technique is sensitive to motion, which makes imaging the heart particularly challenging. To deal with cardiac motion, images are acquired during different cardiac cycles and are then all combined with respect to the corresponding

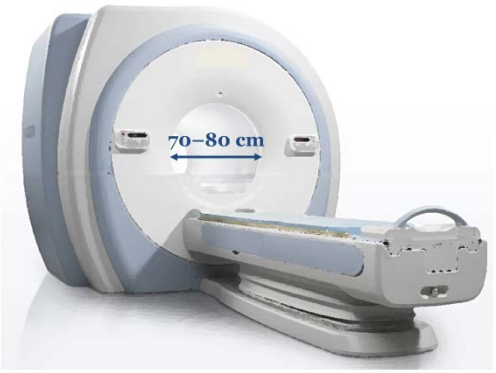

Figure 4.14 – Illustration of a clinical magnetic resonance imaging scanner.

cardiac phase by means of a technique called electrocardiogram (ECG) gating [95]. This implies that the MRI images of the heart are averaged over many cardiac cycles and not reconstructed from a single heartbeat, which can be problematic in patients with heart failure. Another disadvantage of MRI is the lower spatial resolution (a few millimeters) compared with CT and ultrasound (a fraction of a millimeter). Additionally, the technique is expensive and cannot be used in patients with implants that are not MRI compatible. The high cost is mostly because of the complexity of the equipment (Figure 4.14), particularly the high-intensity field magnet, the infrastructure around it and its maintenance. In addition, image acquisition is time consuming, with typical examination times of approximately 30−45 minutes, which also impacts the overall cost and patient's comfort. An example of a cardiac MRI can be seen in Figure 4.15. Both ultrasound imaging and MRI are largely used in clinical practice for diagnostic purposes. The next two paragraphs will focus on the evaluation of medical images and on relevant diagnostic indexes that can be measured to assess cardiac and vascular function.

4.3.3 Assessment of cardiac function

To assess the cardiovascular condition of a patient and diagnose possible pathologies, cardiac function is qualitatively and quantitatively evaluated. In clinical practice, cardiac function is primarily evaluated by echocardiography, i.e. ultrasound imaging applied to the heart [92,96,97]. However, MRI has gained importance when assessing the left ventricular myocardium, e.g. after myocardial infarction [98], in congenital heart disease [99] and when assessing specific pathologies such as myocarditis [100] and fibrosis [101].

The most widely used index of global cardiac function is the ejection fraction (EF) [92]. EF is defined as the fraction of blood ejected from the ventricle at each heartbeat. Specifically, it is calculated as the stroke volume divided by the end diastolic volume.

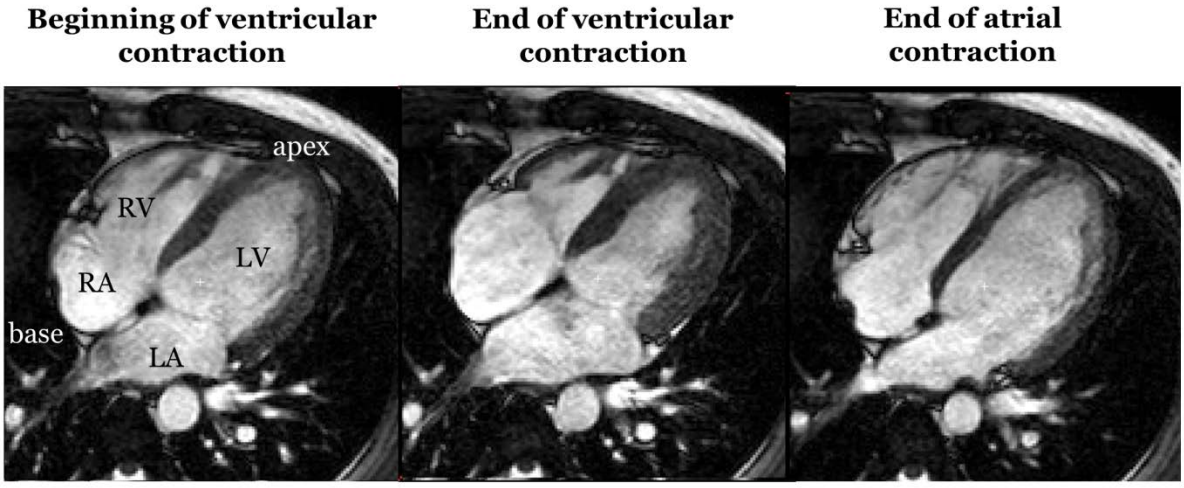

Figure 4.15 – Magnetic resonance images of the four cardiac chambers (4-chamber view) at three different time points in the cardiac cycle. The apex of the heart is located on the top right corner of the image. LV = left ventricle; RV = right ventricle; LA = left atrium; RA = right atrium.

Despite its widespread use in clinics, EF is sensitive to both preload and afterload [102] and cannot detect diastolic dysfunction, which is often referred to as heart failure with preserved EF [103]. Other types of measurement can better characterize global cardiac function, such as global longitudinal strain and AV-plane displacement. Global longitudinal strain has proven to be more sensitive than left ventricular EF as a measure of systolic function [104]. AV-plane displacement below 10 mm has been shown to be predictive of major in-hospital adverse cardiac events [26] and cardiovascular mortality [105]. Additionally, a recent study has shown that AV-plane displacement is the main determinant of maximal cardiac output and that AV-plane displacement can be preserved with lifelong endurance training [106]. Other measurements such as those of mitral or tricuspid annulus excursion should be considered as similar to the AV-plane displacement, since the annuli of the mitral and tricuspid valves are located in the AV plane (Figure 4.4). However, displacement measurements in the AV-plane region are also load dependent [107,108]. Methods based on calculating ratios between peak flow and myocardial velocities have been suggested to overcome this problem, but their load independency still needs to be fully confirmed [109,110].

A better understanding of physiological and pathophysiological function would be highly beneficial for suggesting new clinically useful indexes or helping to identify which of the currently available methods is preferable. For these reason, studies that focus on basic physiology are of high importance [13,14,28,111,112].

4.3.4 Assessment of vascular function

As highlighted in section 4.1.3, vascular function is crucial for preserving the heart's loading conditions and optimal pump efficiency. Furthermore, peripheral vascular disease is associated with stroke and leg ischemia [113]. For these reasons, several methods have been developed to assess vascular function in terms of arterial stiffness, which will be described briefly in the following sections.

Measuring arterial stiffness

Numerous methods have been suggested for estimating arterial stiffness *in vivo*, both locally and globally [114]. Estimations of global arterial stiffness are commonly made using the pulse wave velocity (PWV) technique and of local arterial stiffness by using echo-tracking or pulse waveform analysis [114]. The method based on PWV calculates the velocity at which the pressure and flow waves generated by the heart transmit through the arterial system, given that this velocity depends on arterial stiffness. The PWV can be calculated by detecting the time of arrival of the wave front between two locations of the arterial tree at a known distance and relate it to Young's modulus E of the arterial tree by means of the modified Moens–Korteweg equation [115]

$$PWV = \sqrt{\frac{Eh}{2R\rho(1 - \nu^2)}} \tag{4.3}$$

where h is the thickness, R the radius, ν the Poisson's ratio and ρ the density of the artery. Although it is used extensively in clinical research [116–118], this technique has several

limitations [119]. In particular, the Moens–Korteweg relation in (4.3) assumes constant vessel dimensions along the traveling path of the pulse wave and throughout the cardiac cycle. Furthermore, because measurements are performed over a large segment of the arterial tree, the true length of which is difficult to measure *in vivo*, errors of up to 30% may be introduced [115,117]. Some of these limitations have been overcome by using echo-tracking methods that estimate local arterial stiffness, e.g. by relating arterial diameter changes to pressure changes during the cardiac cycle [114]. These methods are usually based on images of the common carotid artery (Figure 4.16), where the arterial wall displacement generated by the pressure wave traveling in the arterial system is tracked over time. Such methods include the stiffness index [120], distensibility [121], local PWV [122], pulse wave imaging [20] and arterial wall strain [19,123].

In the late 1990s, the ultrasound-based technique SWE was introduced. Since then, SWE has been clinically applied for detection of liver fibrosis [115] and breast cancer [116]. In those applications, the technique was used successfully to measure soft-tissue stiffness and distinguish pathological from healthy tissue, thus improving diagnostics.

Later, preliminary studies by Couade et al. [28] and Bernal et al. [29] applied SWE to measure arterial stiffness. The advantage of SWE compared with the other methods previously mentioned is that SWE is capable of measuring intrinsic mechanical properties locally, quantitatively and multiple times during the heart cycle.

Figure 4.16 – Example of an ultrasound image of the common carotid artery. Diameter and wall thickness can be measured in the image as can change with age and pathology [124,125]. Ultrasound-based methods for the estimation of arterial stiffness use wall displacement during the heart cycle to indirectly derive the arterial mechanical properties.

Arterial shear wave elastography

The SWE technique takes advantage of the physical laws that relate the speed of shear waves to the shear modulus of the medium. By inducing shear waves in the tissue and measuring their speed, it is possible to derive the shear modulus, which can in turn be used as an indicator of the medium's stiffness. A higher shear wave speed indicates a stiffer medium. Figure 4.17 shows the three main steps performed during SWE, which are designed to:

1) generate a shear wave in the tissue by means of focused ultrasound beams,
2) track the shear wave by ultrafast plane wave imaging,
3) estimate the elastic modulus from the shear wave speed.

The generation of shear waves is achieved by strongly focusing the ultrasound beam in one or multiple locations [126,127]. In this way, an acoustic radiation force (ARF) is applied in the tissue, causing its motion. Starting from the focal point, shear waves propagate away from their origin in the direction parallel to the transducer, whereas the displacement of the tissue occurs in the direction perpendicular to that of propagation, as exemplified in Figure 4.17a. Shear waves in soft tissues travel at speeds in the range of a few meters per second. Therefore, imaging with a frame rate of 5–10 kHz is needed to track their displacement. This high frame rate cannot be achieved with conventional ultrasound, where crystals are activated sequentially to scan the medium line by line, but can be achieved by ultrafast plane wave imaging [128], where all the crystals are activated at the same time to generate a single-plane wave and the beam forming is done in post processing (Figure 4.17b). Finally, by tracking the axial motion of the tissue in the ultrasound images, it is possible to measure the speed of the shear wave and estimate the tissues' mechanical properties. The stiffness information is then displayed using, e.g. a color map (Figure 4.**17**c).

Large and relatively uniform organs such as the breast and liver can be considered as of infinite extent when compared with the wavelength of the shear wave, which is in the order of millimeters [15]. In such organs, shear waves can be assumed to travel in free space and, when considering the medium as purely elastic, one can derive the linear elastic shear modulus μ from the density ρ of the tissue and the shear wave speed c_s by:

$$\mu = \rho c_s^2. \tag{4.4}$$

Commercial SWE systems are based on these assumptions and return reliable estimations only when applied to large organs. Arteries are thin tubular structures with wall thickness ranging from fractions of millimeters in small arteries to a few millimeters in the aorta. This implies that the arterial wall thickness is comparable with the wavelength of the shear wave and arteries cannot therefore be considered as a medium of infinite extent in SWE applications. Nevertheless, commercial SWE systems have been used to examine arteries both *in vitro* [129] and *in vivo* [130].

When shear waves propagate in the arterial wall, there are multiple reflections at the interfaces between the wall and blood or surrounding tissue. Therefore, mechanical energy remains confined within the arterial wall and the artery behaves as a wave guide.

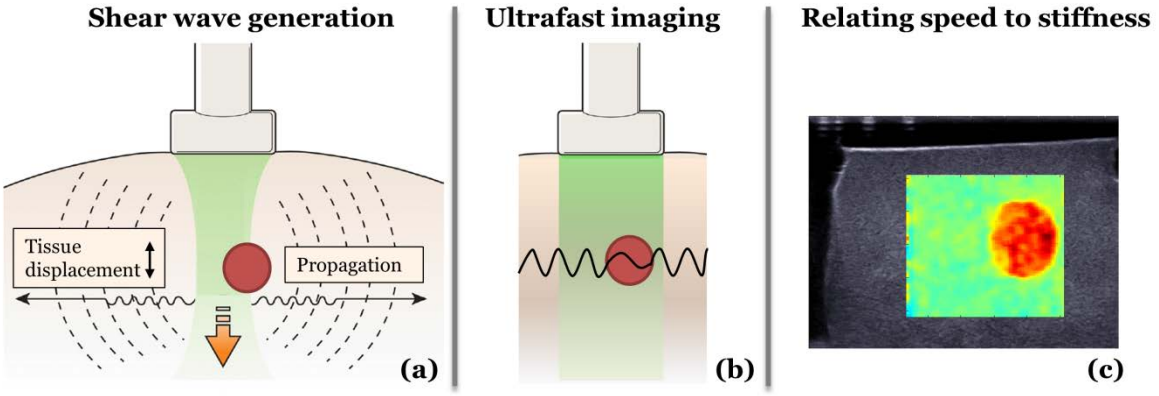

Figure 4.17 – Schematic representation of the three main steps involved in shear wave elastography. In (a), the orange arrow indicates the direction of the longitudinal ultrasound waves used to generate the transverse shear wave by a highly focused ultrasound beam, also called "push". The red circle represents a stiffer inclusion. In (b), all crystals in the transducer are simultaneously activated to generate plane waves, which are used to image the shear wave propagation at a high frame rate (~10 kHz). In (c), a color map is overlapped onto the conventional ultrasound B-mode image and the color represents the stiffness. In the displaced image, the red color indicates that there is a stiffer inclusion in a softer surrounding, which is shown in green.
Images (a) and (b) reproduced and modified with permission from [131] *under the Creative Commons Attribution Noncommercial License.*

Waves traveling in a guide exhibit velocity dispersion, because different frequencies travel at different speeds. In such cases, a single velocity value representing the group velocity of the wave as in equation (4.4) cannot be used. Instead, velocity should be considered as a function of frequency by measuring the phase velocity of the propagating wave.

As is the case for vessels, the conventional assumptions of infinite length, isotropy and purely elastic media are not valid for the heart either. In particular, the myocardium is highly anisotropic and therefore shear waves propagate at different speeds in different directions. In addition to this, the heart is located deep in the body and surrounded by the thoracic cage, which makes the generation of the shear waves with a small cardiac phased-array transducer challenging. Despite these complications, initial studies have shown the feasibility of performing cardiac SWE *in vivo* [22,132] and the sensitivity of the technique to anisotropy [132], which plays a significant role in the shear wave propagation [23].

Wave propagation in thin media

Guided wave propagation in thin media has been studied extensively. Lamb has derived an analytical solution for wave propagation in an elastic plate in a vacuum [133]. Additionally, an analytical solution for wave propagation in a hollow cylinder, geometry close to that of an artery, was derived by Gazis [134]. However, the latter solution includes a series of Bessel functions, which can only be determined numerically [135] and therefore limits its usability in SWE applications. A trade-off was reached by approximating the complex wave propagation in the artery with a zero-order antisymmetric Lamb wave mode [16,17], given that the fundamental phase velocity–frequency relation of a plate and a hollow cylinder merge at higher frequencies [17]. Based on Lamb's theory, Bernal et al. [16] derived the equation for the zero-order antisymmetric mode in a solid plate submerged in a nonviscous

incompressible fluid, assuming that the solid plate and surrounding fluid have similar densities and wavenumbers; the equation is given as:

$$4k_L^3\beta\cosh\left(k_L\frac{h}{2}\right)\sinh\left(\beta\frac{h}{2}\right)-\left({k_s}^2-2k_L^2\right)^2\sinh\left(k_L\frac{h}{2}\right)\cosh\left(\beta\frac{h}{2}\right)=k_s^4\cosh\left(k_L\frac{h}{2}\right)\cosh\left(\beta\frac{h}{2}\right) \tag{4.5}$$

where $k_L=\omega/c_L$ is the Lamb wavenumber, $k_S=\omega\sqrt{\rho/\mu}$ is the shear wavenumber, $\beta=\sqrt{k_L^2-k_s^2}$, ω is the angular frequency, h is the plate thickness and c_L is the frequency-dependent Lamb wave velocity. The thickness h and density ρ are input parameters and the elastic shear modulus μ can be derived by fitting the experimental dispersion curve to (4.5), where k_S and β are functions of μ.

5 Methodology and contributions

The general aim of this thesis was to improve our understanding of cardiovascular physiology and develop new methods for assisting clinicians during diagnosis and treatment of cardiovascular diseases. Both computer simulations and medical imaging were used to reach this goal. In the following sections, the methodology used in the four studies and the developed models and techniques will be described. Table 5.1 summarizes the main features of each study.

Table 5.1 – Overview of the studies included in this thesis.

	Study I *AV-plane physiology*	**Study II** *In vivo LA and LV short-axis areas*	**Study III** *Arterial–cardiac interaction during aging*	**Study IV** *Shear wave elastography*
Organ of interest			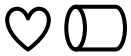	
Type of study	Modeling and simulations	Imaging – *in vivo*	Simulations	Imaging – *in vitro*
Imaging modality	–	MRI	–	US

MRI = magnetic resonance imaging; US = ultrasound.

5.1 Cardiovascular modeling

In the following sections, the cardiovascular models included in Studies I and III will be presented. First, a general overview of the models will be given, followed by a description of the equivalent bond graph models. Subsequently, the strategy used to assign the parameter value to each component will be described.

5.1.1 General description of the models

Atrioventricular–piston model

The objective of **Study I** was to develop a cardiac model based on the functioning of the heart as described in the introduction in section 4.1.1.

Three main features were included in the model:

1) The AV plane was modeled as a piston unit, moving in the base–apex direction.
2) The largest atrial cross section was smaller than the largest ventricular cross section (VSA).
3) The contraction force was the primary input to the model.

Figure 5.1 shows a schematic representation of the proposed cardiac model with the AV plane seen as a piston unit (AV piston) moving back and forth in the base–apex direction. This pump model represents only one side of the heart. In this thesis, focus was put on the left side of the heart but a similar model could also be used for the right. However, different pressure levels and parameters would be needed when applying the model to the right side.

The housing of the pump model is rigid and restricts external volume changes, similarly to the pericardial sac surrounding the heart. Even though external volume changes are limited, there are internal and reciprocal volume changes between the two chambers. A one-way valve (the mitral valve) is located between the upper chamber (the atrium) and the lower chamber (the ventricle). Another one-way valve (the aortic valve) is located between the ventricle and the outflow tube, representing the aorta. The AV piston is constructed with two different areas toward the atrium (A_1) and toward the ventricle (A_2). A_1 corresponds to the largest cross-section in the atrium and A_2 to the largest cross-section in the ventricle.

During ventricular systole, the AV piston is pulled toward the ventricle by the contraction force (Figure 5.1). This force is modeled as an external input acting on the AV piston (Figure 5.2). When the contraction force is applied (Figure 5.2a), the mitral valve closes, the aortic valve opens and the blood flows from the ventricle to aorta. An additional effect of the movement of the AV piston during systole is that atrial volume increases, aiding atrial filling. During ventricular diastole, the input force ceases (Figure 5.2b), aortic valve closes and, slightly later, mitral valve opens.

This sequence of events occurs since the piston experiences a hydraulic force (F_{hyd}) that can be expressed as:

$$F_{hyd} = A_2 \cdot P_v - A_1 \cdot P_a \tag{5.1}$$

where P_v is the ventricular pressure and P_a the atrial pressure. Before mitral valve opens, both P_v and A_2 are larger than P_a and A_1 respectively and therefore there is a net force pushing the AV piston toward the atrium. When P_v reaches the same value as P_a, the mitral valve opens. At this time point, the pressure in the atrium and in the ventricle is approximately the same, apart from a minor pressure drop caused by mitral valve resistance. Despite having the same pressure in the two chambers, there is still a net hydraulic force pushing the AV piston toward the atrium because of the difference in area between the piston's upper and lower extremity. This hydraulic force moves the piston back to its initial position and allows flow from the atrium to the ventricle.

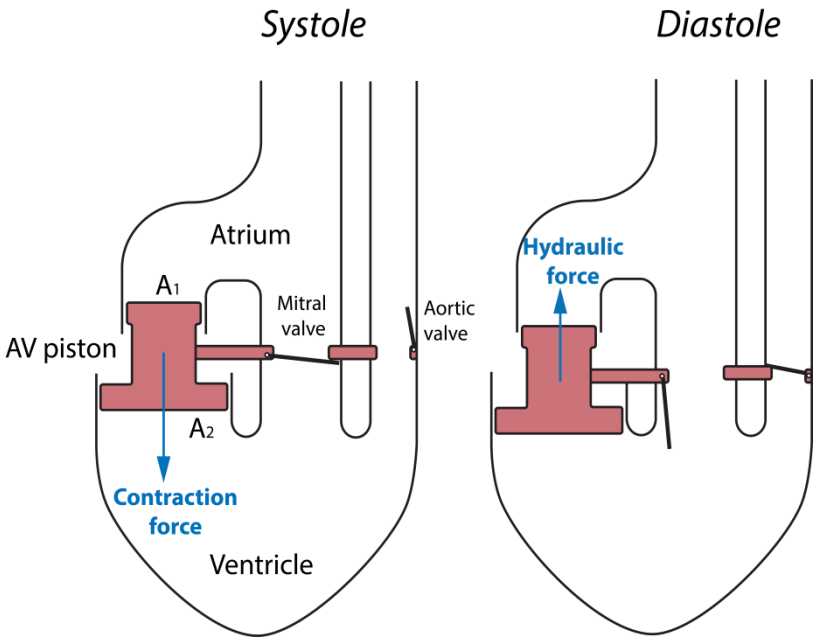

Figure 5.1 – Illustration of the cardiac model where the atrioventricular (AV) plane is continuously moving in the longitudinal direction to carry out the pumping action of the heart. During systole, the AV piston is pulled toward the ventricle by the ventricular contraction force, which is an external input to the model. During diastole, the AV piston moves toward the atrium because of the hydraulic force generated by the difference in area between the superior and inferior area of the piston.

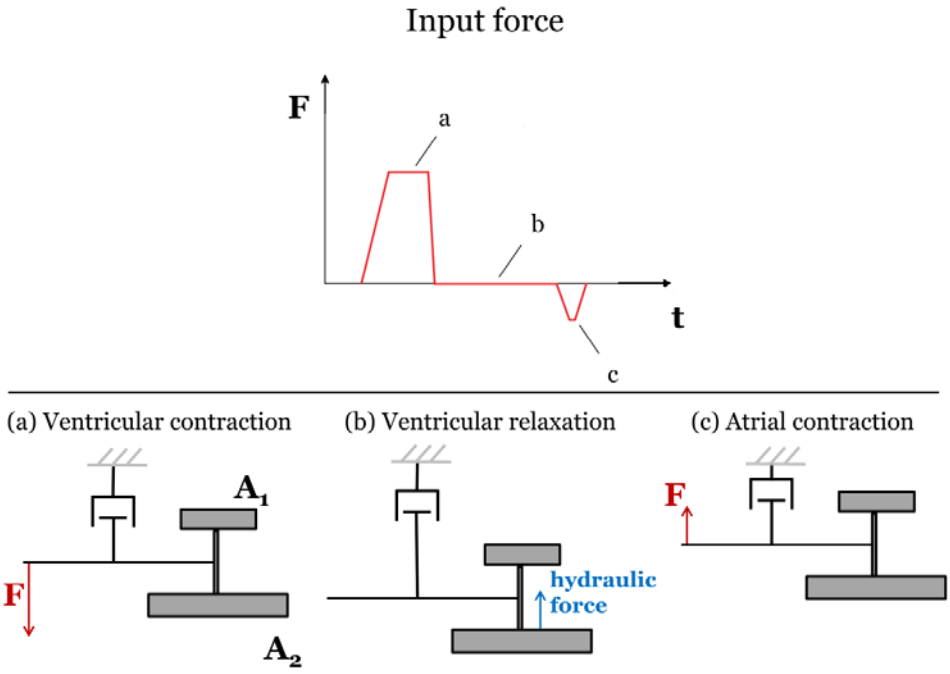

Figure 5.2 – Schematic representation of the input force (F) applied to the atrioventricular piston. (a) During ventricular contraction, the contraction force pushes the piston toward the ventricle. (b) During ventricular relaxation, there is no externally-applied force to the piston but the piston experiences a hydraulic force because of the difference in area between A_1 and A_2. (c) During atrial contraction, an external force is applied to the piston and pulls it toward the atrium.

In this model configuration, the difference in area between the upper and lower part of the piston is constant and no constraints are applied to the AV piston movement, therefore the mitral flow does not stop until the next input force is applied.

In summary, the higher pressure on the ventricular side initiates the piston return and causes mitral valve to open. Once the valve opens, the movement can continue because of the difference in area of the piston's extremities. The upward movement of the AV piston produces a redistribution of volume from the atrium to the ventricle, keeping the total pump volume approximately constant, apart from a minor compliance of the pump's housing. This return is a result of the AV piston's geometry since no external input is applied during diastole. At the end of the diastolic phase, an additional force, representing atrial contraction, is applied to the piston in the opposite direction of the ventricular contraction force (Figure 5.2c). The effect of the atrial contraction force is to lift the AV piston toward the atrium and allow further redistribution of blood from the atrium to the ventricle.

Cardiovascular-aging model

The objective of **Study III** was to model the global effect of cardiovascular aging on blood pressure. To reach this objective, established and validated lumped-parameter models for the left ventricle and arterial tree were used. The left ventricular pumping effect was modeled by the time-varying elastance model described in section 4.2.2 in the introduction. The systemic arterial tree was modeled by the four-element Windkessel model. An overview of the two models interconnect and represented by electrical equivalents is shown in Figure 5.3. The time-varying elastance profile can be expressed by many different mathematical functions [8,68,136]. Among these, the *double-Hill* function was chosen [68,137] and the time-varying elastance was therefore expressed as

$$E(t) = k\left(\frac{g_1}{1+g_1}\right)\left(\frac{1}{1+g_2}\right) + E_{ed} \tag{5.2}$$

where

$$g_1 = \left(\frac{t}{\tau_1}\right)^{m_1}, \quad g_2 = \left(\frac{t}{\tau_2}\right)^{m_2} \tag{5.3}$$

and k is defined by

$$k = \frac{E_{es} - E_{ed}}{max\left[\left(\frac{g_1}{1+g_1}\right)\left(\frac{1}{1+g_2}\right)\right]} \tag{5.4}$$

in order to guarantee that max(E) = $E_{es.}$

The parameters needed to define the double-Hill function are E_{es}, E_{ed}, m_1, m_2, τ_1, τ_2 and T. The maximum elastance value occurs at end systole (end of contraction in Figure 5.3) and

is represented by E_{es}. The minimum elastance value occurs during diastole (relaxation in Figure 5.3) and is represented by E_{ed}. The parameters m_1 and m_2 characterize the contraction and relaxation rate, respectively. A higher value of m1 results in a steeper rising of the E(t) during contraction, whereas a higher of m2 results in a faster relaxation. The time constants τ_1 and τ_2 are expressed in terms of the heart period T (e.g. τ_1 = 0.269T and τ_2 = 0.452T) and locate the inflection point of $\left(\frac{g_1}{1+g_1}\right)$ and $\left(\frac{1}{1+g_2}\right)$. By modifying τ_1 and τ_2, contraction and relaxation can be prolonged or reduced.

The double-Hill function was connected to the four-element Windkessel model characterized by the following parameters: characteristic impedance Z_c, inertance L, total arterial compliance C_{tot} and peripheral vascular resistance R_p (see section 4.2.3 for details). The mitral and aortic valves are considered to act as diodes, which are either fully open or fully closed and allow flow (equivalent to electrical current) in the forward direction only. The cardiac valves used the Study III also included a small resistance (0.003 mmHg·s/mL), representing the resistance to flow through the open valve leaflets, and a small inertance (3×10^{-5} mmHg·s^2/mL), representing blood inertia.

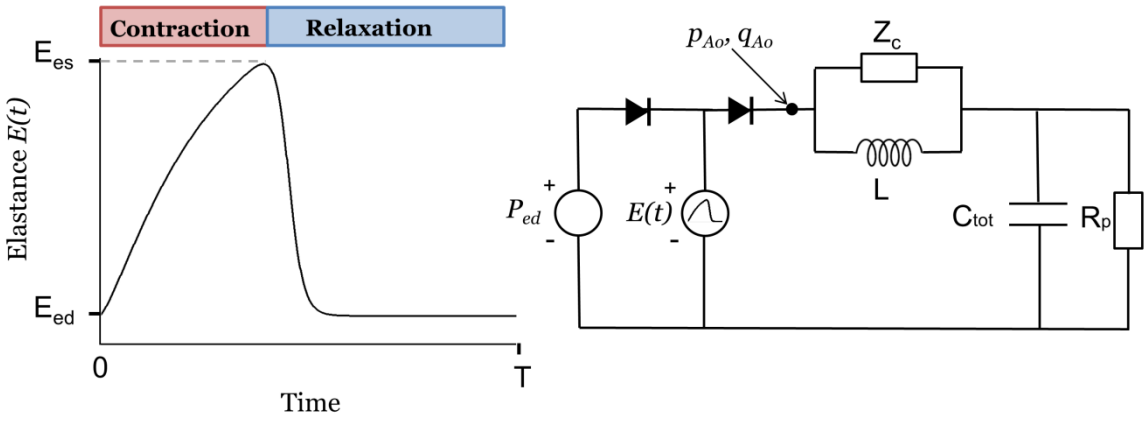

Figure 5.3 – Schematic representation of the time-varying elastance model E(t) and the four-element Windkessel model used to simulate cardiovascular changes with age in Study III. E_{es} = end-systolic elastance; E_{ed} = end-diastolic elastance; P_{ed} = end-diastolic pressure; p_{Ao} = aortic pressure; q_{Ao} = aortic flow; Z_c = characteristic impedance; L = inertance; C_{tot} = total arterial compliance; R_p = peripheral vascular resistance.

5.1.2 Equivalent bond graph models

Atrioventricular-piston model

The pump model in Figure 5.1 was converted to the bond graph formalism and connected to a simplified circulation model in a closed-loop, as can be seen in Figure 5.4. The bonds (half arrows) show the direction of energy transport. A 0-junction implies that the bonds attached to the junction have the same pressure and a 1-junction implies that the bonds attached to the junction have the same flow. The atrium and ventricle were modeled as compliance elements (C). The valves between the atrium and the ventricle and between the ventricle and the circulation were based on a previous study [138] and included a resistance-to-flow element (R) and an inertia element (I). A switch was connected to the two valves and controlled by the difference in pressure before and after the valve. The switch is on (the valve is open) when the pressure upstream is higher than the pressure downstream. The switch is off (the valve is closed) otherwise. The part highlighted in light red in Figure 5.4 represents the AV piston. The AV piston was described as two transformer elements (TF1 and TF2) with a transformation ratio equal to the atrial cross-section (A1) for the upper area and to the ventricular cross-section (A2) for the lower area. The contraction force was modeled as an effort source (Se) directly connected to the piston. The AV-piston part of the model belongs to the mechanical domain, whereas the rest of the model belongs to the hydraulic domain. The conversion between the two domains occurs at the level of the transformer elements that convert force to pressure through the transformation constant area.

The arterial side of the circulation is modeled as a three-element Windkessel model (Figure 5.4), which includes two resistor elements (R_{1art} and R_{2art}) representing characteristic impedance and peripheral resistance, respectively, and a compliance element (C_{art}) representing total arterial compliance. In addition, a vein compartment was inserted between the circulation and the atrium. The vein included a large compliance element, C_{vei}, serving as a volume reservoir for the blood to uncouple the pressure between the arterial and venous sides. A series (1-junction) of R and I elements was connected in parallel (0-junction) to C_{vei} to mimic a more realistic atrial filling.

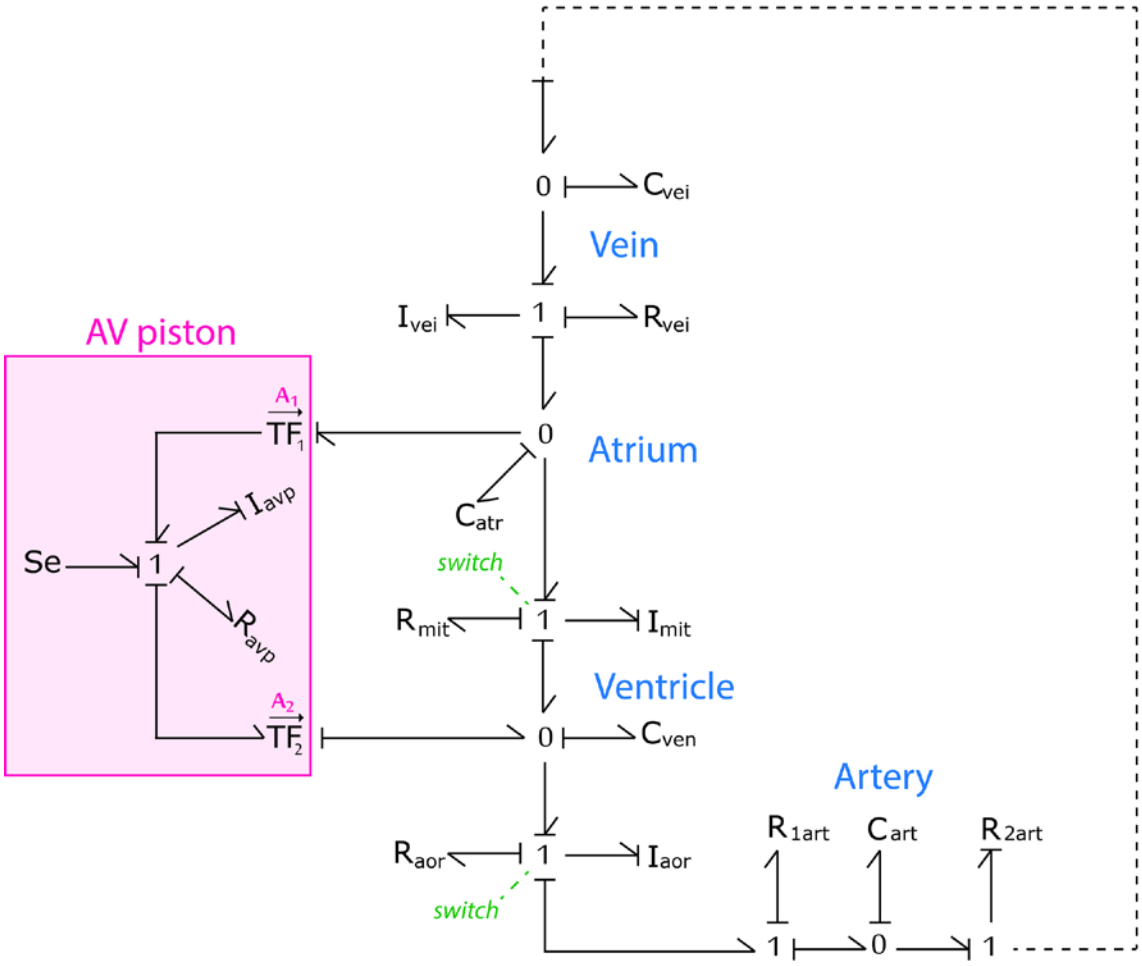

Figure 5.4 – Equivalent bond graph model of the cardiac piston model shown in Figure 5.1 connected to a simplified circulation model. The vein, atrium, ventricle and artery correspond to the hydraulic domain. The part highlighted in red represents the AV piston and corresponds to the mechanical domain. The transition between the two domains occurs because of the two transformer elements (TR) that convert force to pressure through the transformation coefficient area (A). The artery corresponds to a three-element Windkessel model.

Ventricular–arterial interaction model

Similarly to the piston model, the ventricular–arterial interaction model used in Study III was converted to the bond graph formalism (Figure 5.5). The time-varying elastance was represented as a time-varying compliance, i.e. a modulated C-element, since compliance is the inverse of elastance. The mitral and aortic valve models were the same as in the piston model. Filling pressure was represented by a constant effort source (Se). Characteristic impedance and peripheral vascular resistance were represented by an R-element, total arterial compliance by a C-element and inertance by an I-element.

5.1.3 Parameter selection

In this section, the methods used to assign parameters to the models' components will be described.

Atrioventricular-piston model

All parameters used for simulations are presented in Table 5.2 and Table 5.3. The values were either based on the literature or calculated. When based on the literature, the source is reported in Table 5.2. The magnitude of the contraction force applied on the AV piston (Table 5.3) was chosen to generate a realistic systolic pressure in the ventricle. Therefore, given the piston ventricular area A_2 and the ventricular systolic pressure p_{v_sys}, a first estimate of the maximum force during ventricular contraction was $F_{max} = p_{v\_sys} \cdot A_2$. This value was then empirically increased to overcome the resistance to motion and to generate the desired p_{v_sys}.

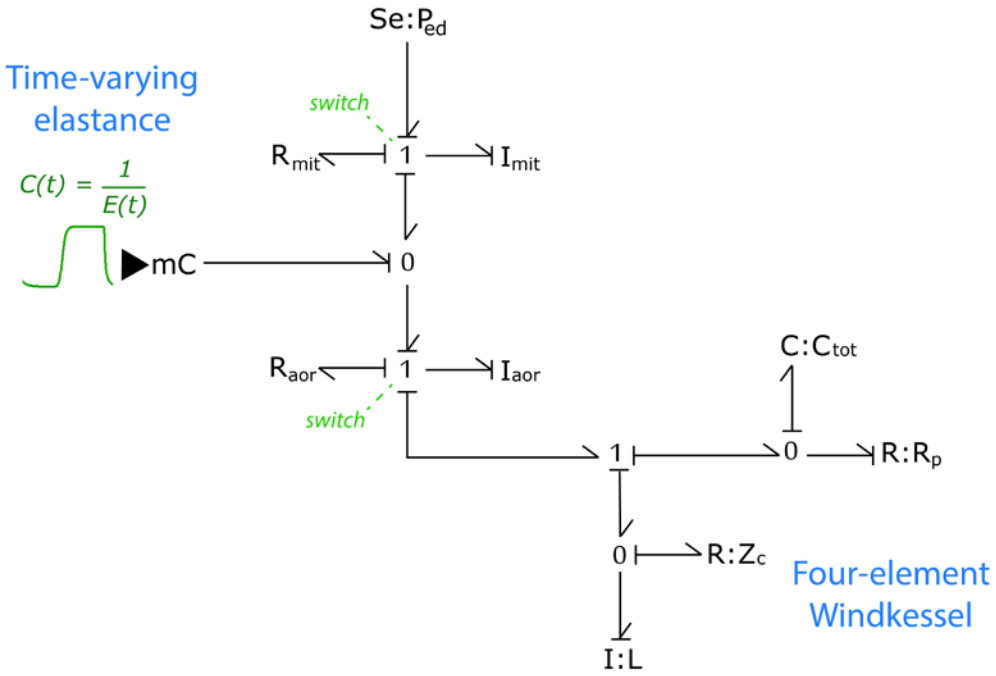

Figure 5.5 - Equivalent bond graph representation of the ventricular–arterial interaction model in Figure 5.3. The time-varying elastance is represented by a modulated C-element (mC). The filling pressure is represented by a constant effort source (Se). The notation X:Y means "bond graph element X at which is attributed the parameter Y".

Table 5.2 – Values for parameters used during simulations in Study I, corresponding to the bond graph elements in Figure 5.4.

	Description	**Value**	**Unit**	**Reference**
C_{vei}	Venous compliance	50	mL/mmHg	[139]
R_{vei}	Venous resistance	0.01	mmHg·s/mL	
I_{vei}	Venous inertia	0.0001	mmHg·s^2/mL	
C_{atr}	Atrial compliance	0.3	mL/mmHg	Minimum compliance value in [10,137]
R_{mit}	Resistance to flow in the mitral valve	0.008	mmHg·s/mL	Estimated from pressure drop across the valve in [97]
I_{mit}	Inertia to flow in the mitral valve	0.0002	mmHg·s^2/mL	
C_{ven}	Ventricular compliance	0.3	mL/mmHg	Minimum compliance value in [10,137]
R_{aor}	Resistance to flow in the aortic valve	0.005	mmHg·s/mL	Estimated from pressure drop across the valve in [97]
I_{aor}	Inertia to flow in the aortic valve	0.00002	mmHg·s^2/mL	
C_{art}	Arterial compliance	1.01	mL/mmHg	[8,140]
R_{1art}	Characteristic impedance	0.08	mmHg·s/mL	[8,140]
R_{2art}	Total peripheral resistance	1.28	mmHg·s/mL	[8,140]
I_{avp}	Inertia of the piston	30	mmHg·cm·s^2	
R_{avp}	Damping in the piston	300	mmHg·cm·s	
A_1	Piston area from atrial side	25	cm^2	From MRI images in Study II
A_2	Piston area from ventricular side	50	cm^2	From MRI images in Study II

Table 5.3 - Input values for the contraction force in Study I and as illustrated in Figure 5.2.

Input	Description	Value		Unit
		ventricular contraction	*atrial contraction*	
F_1	Maximum force, normal	7350	-1500	mmHg·cm^2
F_2	Maximum force, –30%	5145	-1500	mmHg·cm^2
	Total duration	0.35	0.2	s
	Rising	0.1	0.1	s
	Falling	0.01	0.1	s
	Period	0.95	0.95	s

Cardiovascular-aging model

The age range of interest in Study III was adult life (20 to 80 years of age) and the study investigated nonpathological aging, which will be referred to as “normal aging”. All parameters needed to simulate the time-varying elastance model and the Windkessel model have not been fully characterized for all age groups. However, many studies provide information about arterial stiffness and peripheral vascular resistance with age [116,141,142]. Similarly, information can be found about left ventricular structural and functional changes with age [143–145]. Based on these considerations, the method used to assign parameters for the simulation of cardiovascular aging was as follows:

1) Assign baseline parameters at the age of 20 years that provide physiological aortic pressure and flow waveforms.
2) For the subsequent decades, impose changes in total arterial compliance and peripheral resistance corresponding to the values reported in the literature.
3) Apply adaptation rules based on observations reported in the literature to derive the cardiac parameter changes.

The timing of the cardiac cycle (heart period T = 0.89 s, systolic and diastolic time constants, τ_1 = 0.269T and τ_2= 0.452T, respectively) were chosen according to a previous study [137] and kept constant for all ages. The inertance parameter L of the arterial model was also kept constant for all ages (L = 0.005 mmHg·s^2/mL). The other parameter values at the age of 20 years were chosen based on previous studies [146,147] and are reported in Table 5.4.

Table 5.4 – Model parameters at the age of 20 years used in Study III.

Arterial parameters			Cardiac parameters		
C_{tot} (mL/mmHg)	R_p (mmHg·s/mL)	Z_c (mmHg·s/mL)	E_{es} (mmHg/mL)	E_{ed} (mmHg/mL)	P_{ed} (mmHg)
2.800	0.800	0.020	1.000	0.025	5.000

The first age-related changes applied to the parameters were related to arterial compliance (inverse of arterial stiffness). Structural changes of the arterial wall result in an increase in arterial stiffness with age. In the range of 20 to 80 years, as investigated in Study III, the increase in stiffness was quantified by pulse wave velocity to be a factor of two [116,141], corresponding to a decrease in compliance of a factor of four [148]. Therefore, C_{tot} decreased linearly by a factor of four from 20 to 80 years. This change in compliance also affected the characteristic impedance parameter, since Z_c is proportional to $1/\sqrt{C}$ [147]. Vascular resistance was found to increase by 5% per decade based on a previous study of healthy middle-aged men and women [142], and increased from 0.8 mmHg s/mL at 20 years to 1.04 mmHg s/mL at 80 years. The arterial parameters described so far were prescribed, whereas the cardiac parameter changes that will be described below were derived using two adaptation rules. The three cardiac parameters that varied with age were found to be E_{es}, E_{ed} and the filling pressure, or pressure in the left atrium (P_{ed}).

The *first rule* used to derive these parameters with age is to normalize ventricular wall stress, which is preserved even when arterial systolic pressure increases [144,145]. A simplified expression of ventricular wall stress σ as a function of left ventricular pressure P_{lv}, radius r_i and wall thickness h is given by the law of Laplace:

$$\sigma = \frac{P_{LV} \cdot r_i}{2h}. \tag{5.5}$$

To keep wall stress constant when P_{LV} increases, considering an unchanged lumen radius as in concentric remodeling [38], h must increase proportionally to P_{LV}. If wall thickness increases and r_i is preserved, the left ventricular myocardial mass must necessarily increase (hypertrophy). This hypertrophy produces both a stronger contractile function (increase in E_{es}) and a left ventricle that is stiffer and more difficult to fill (higher E_{ed}). We assumed that the increases in E_{es} and E_{ed} were proportional to wall thickness and therefore proportional to P_{lv} ($P_{lv2}/P_{lv1} = E_{es2}/E_{es1} = E_{ed2}/E_{ed1}$). The increased wall thickness resulted in an increase in systolic pressure that, by applying the first rule again, caused even more hypertrophy.

The *second rule* is to increase P_{ed} in order to preserve end-diastolic volume, as previously reported in normotensive individuals [143]. An increase in P_{ed} has the effect of reducing peak systolic pressure and increasing end-diastolic volume. Since both rules affect the same parameters, they were applied multiple times in an iterative manner until they were both met and equilibrium was obtained (i.e. pressure changes of less than 1 mmHg and volume changes of less than 1 mL). A scheme summarizing the arterial and cardiac parameter selection process is shown in Figure 5.6.

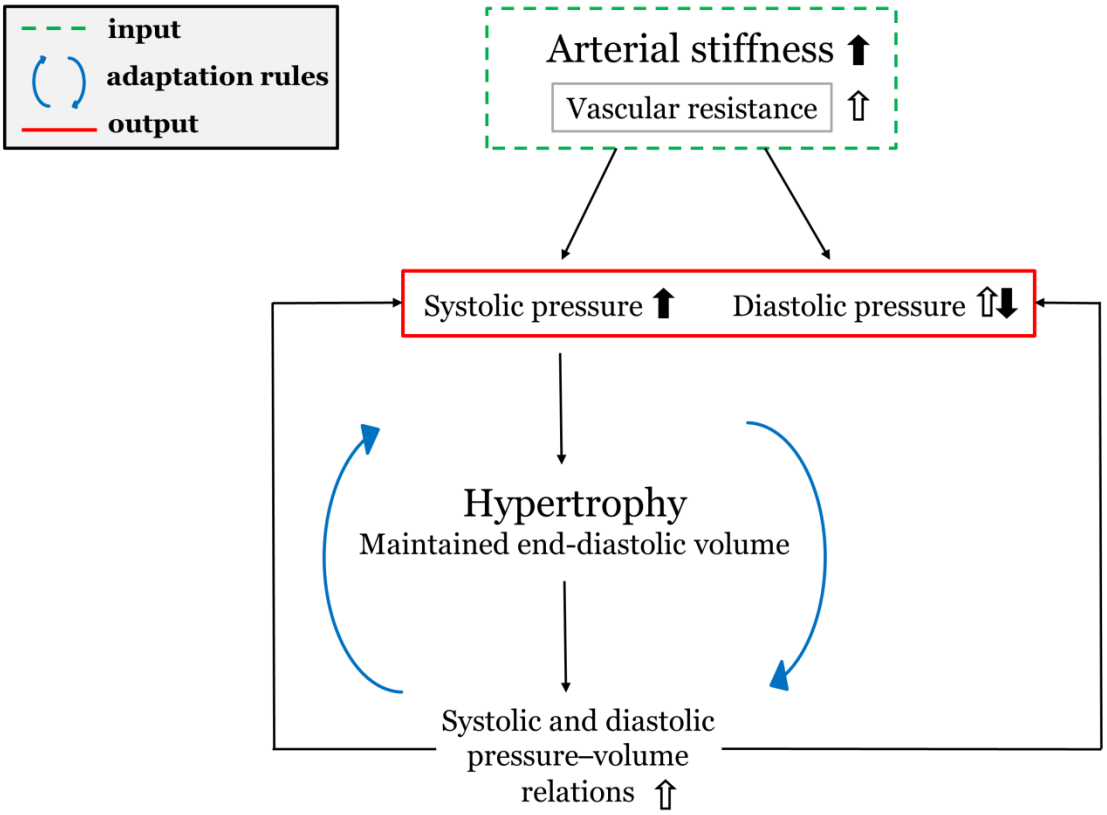

Figure 5.6 – Schematics of the events occurring during normal aging that were used to guide the selection of parameters of the ventricular–arterial model in Study III. The thick black and white arrows indicate parameter changes; the thin black arrows indicate how these parameter changes affect blood pressure and other cardiac parameters. Specifically, arterial stiffness and vascular resistance increase systolic and diastolic blood pressure. The systolic pressure increase induces hypertrophy, which in turn affects E_{es}, E_{ed} and systolic pressure itself (blue loop). Filling pressure is also increased to maintain end-diastolic volume. This loop is repeated until an equilibrium in pressure is reached.

The model output in terms of aortic systolic and diastolic pressure was compared with population data from a large clinical study, the Framingham Heart study [72]. The comparison was done by calculating the root-mean-square error (RMSE) between the simulation results and the population data at each decade (mean value between normotensive groups 1 and 2 in Figure 3 in Franklin *et al.* [72]. Then, a qualitative and quantitative comparison was done to validate the parameter selection method and assess if arterial changes alone or arterial and cardiac changes combined better explained the evolution of blood pressure with age. It should be noted that the model output is the aortic pressure, whereas blood pressure is clinically measured at the level of the brachial artery. Systolic pressure differs between the ascending aorta and the brachial artery. In order to account for this difference, the average systolic pressure amplification previously reported [149] was added to the aortic pressure computed by the model at each decade. The RMSE between the corrected pressure values and the population data was also computed.

5.1.4 Simulations

All models developed and used in this thesis work were drawn by means of the bond graph formalism and simulated using the software platform Dymola (Dassault Systèmes, France) and the bond-graph library (version 2.4) [86]. The DASSL solver was used, with an adaptive step size and a tolerance equal to 0.0001.

5.2 Hydraulic forces physical model

One of the aims of **Study II** was to illustrate the effect of hydraulic forces on the AV piston described in the atrioventricular piston model described in section 5.1.1. For this purpose, a physical model in Plexiglas representing the left atrium and ventricle was constructed. A 3D drawing of the physical model is shown in Figure 5.7. The physical model was constructed with two cylindrical chambers of different diameters. The smaller chamber (the atrium) was connected to a larger chamber (the ventricle) by a hollow piston with two different heads. At one extremity, the piston's head was as large as the atrial chamber in cross section, while at the other extremity, the piston's head was as large as the ventricular chamber in cross section. The piston was hollow in order to represent the open mitral valve and to guarantee that the pressures in the two chambers were the same. The physical model was connected to a water column allowing for pressurization of the two chambers. To appreciate the action of hydraulic force, the pressure needed to be sufficiently high so that F_{hyd} = *(large area – small area)* * *pressure* was larger than the friction impeding the piston's movement. A water column of approximately 140 cm of water allowed a smooth and clearly visible hydraulic return. The physical model was pressurized by water, but could also be pressurized by air.

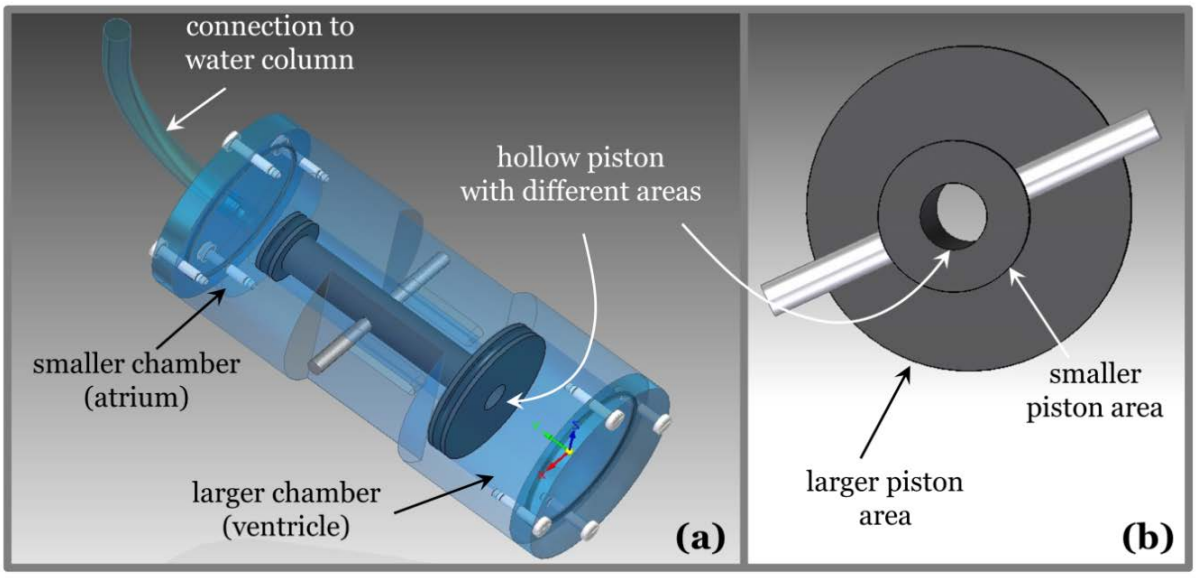

Figure 5.7 – (a) Schematics of the physical model of the left ventricle and atrium built to exemplify the effect of hydraulic forces. (b) Close-up of the hollow piston with different areas where the enclosure of the physical model is removed.

5.3 *In vivo* measurements of atrial and ventricular short-axis areas

An additional aim of **Study II** was to assess the presence and the magnitude of hydraulic forces. To achieve this, measurements of atrial cross section, ventricular cross section and left ventricular diastolic pressure are needed. The reason for measuring the largest cross section in the two cardiac chambers is shown schematically in Figure 5.8. The two configurations in Figure 5.8a are equivalent because of the theory of hydrostatic forces on curved surfaces, according to which the widest area of a container submerged in a liquid is needed to calculate the longitudinal component of the hydraulic force acting on the container walls, independently of the curvature of the surface. This is because the radial component of the force is counterbalanced by the walls of the container, i.e. these represent the pericardium and the surrounding tissues in the case of the heart.

Atrial and ventricular cross sections (corresponding to the short-axis areas described in the medical literature) were measured in medical images of healthy volunteers. Pressure measurements, however, require invasive techniques, which are preferably not performed on heathy individuals. Thus, average left atrial pressure values were taken from a previous study [150].

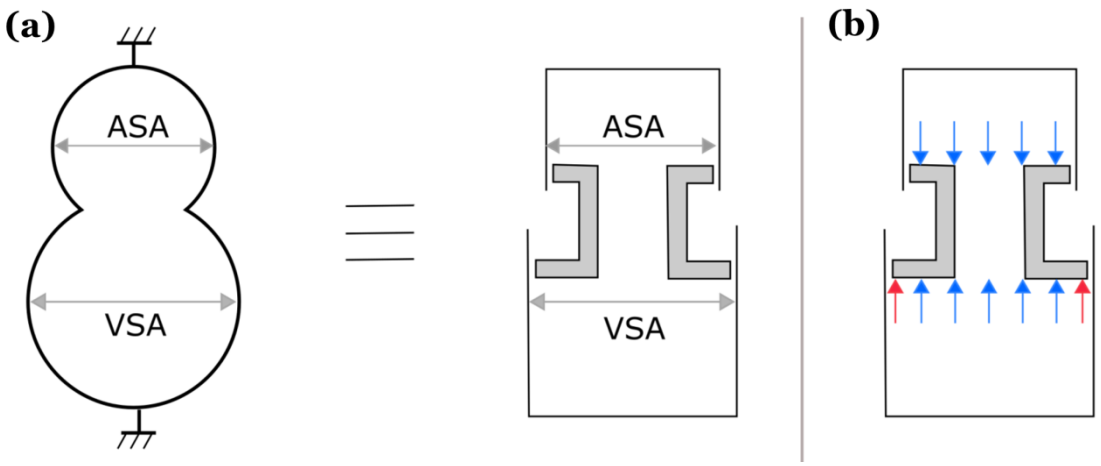

Figure 5.8 – Schematics representation of the left side of the heart compared with the physical model. (a) The two configurations are equivalent based on the theory of hydrostatic forces on curved surfaces. (b) Forces acting on the two different extremities of the piston. The blue arrows counterbalance each other, whereas the red arrows represent the net force that pushes the piston upwards. ASA = atrial short-axis area; VSA = ventricular short-axis area.

5.3.1 Study population

In Study II, dimensions of the atria short-axis area (ASA) and ventricular short-axis area (VSA) corresponding respectively to cross sections A1 and A2 in the AV-plane model of Study I were measured in 10 heathy volunteers (5 women, age 24 ± 3 years). The volunteers had previously been studied for other purposes [14]. The study was approved by the local ethical board and carried out according to relevant guidelines. All subjects provided written informed consent. Cardiovascular magnetic resonance (CMR) was used to retrieve 30 frames of each volunteer's heart throughout the cardiac cycle. More precisely, CMR with steady-state free precession cine images were obtained using a 1.5 T scanner (Philips Intera, Philips, Best, Netherlands). For details of the CMR image acquisition parameters, the reader is referred to a previously study [14].

5.3.2 Area measurements

CMR images were viewed and analyzed using the freely available software Segment (version 2.0 R4636, Medviso AB, Lund, Sweden) as shown in Figure 5.9. The ASA was manually delineated for all subjects in multiple slices for each time frame. The atrial appendage was included in the ASA when visible. At each time point, the largest area among the multiple slices was chosen as the final measurement of the ASA. Concerning the VSA, the contour was initially delineated with the automatic segmentation function of the Segment software and subsequently manually adjusted for increased accuracy. Two contours were drawn: one including the myocardium (VSA_{Epi}) and one excluding the myocardium (VSA_{Endo}). Similarly to the ASA, multiple slices of the VSA near the AV plane were measured, and the largest epicardial and endocardial areas at each time point were selected as VSA_{Endo} and VSA_{Epi}, respectively.

5.3.3 Diastolic filling forces comparison

To understand the contribution of hydraulic forces in relation to other forces, its magnitude was estimated and compared with previous measurements of the peak driving force acting during left ventricular filling. The hydraulic force was calculated as *Force = (Pressure) × (Difference in Area)*, assuming that mean LV diastolic pressure is equal to 10 mmHg in heathy individuals [150]. The difference in area was calculated as (VSA_{Endo} – ASA) or (VSA_{Epi} – ASA) at mid diastasis. The peak driving force during diastolic filling was previously estimated in a population of young healthy subjects to be approximately 25 mN/g [151]. This force is calculated per unit of mass in motion, also referred to as inertial load. The inertial load was assumed to arise from the left ventricular mass, the portion of blood in motion and the roots of the great vessels. The left ventricular mass is approximately 125 g [152], and the blood and great vessels were assumed to be in the range 75–275 g, resulting in a total inertial load of 200–400 g. Finally, the peak driving force of 25 mN/g multiplied by 200–400 g yields a force of 5–10 N.

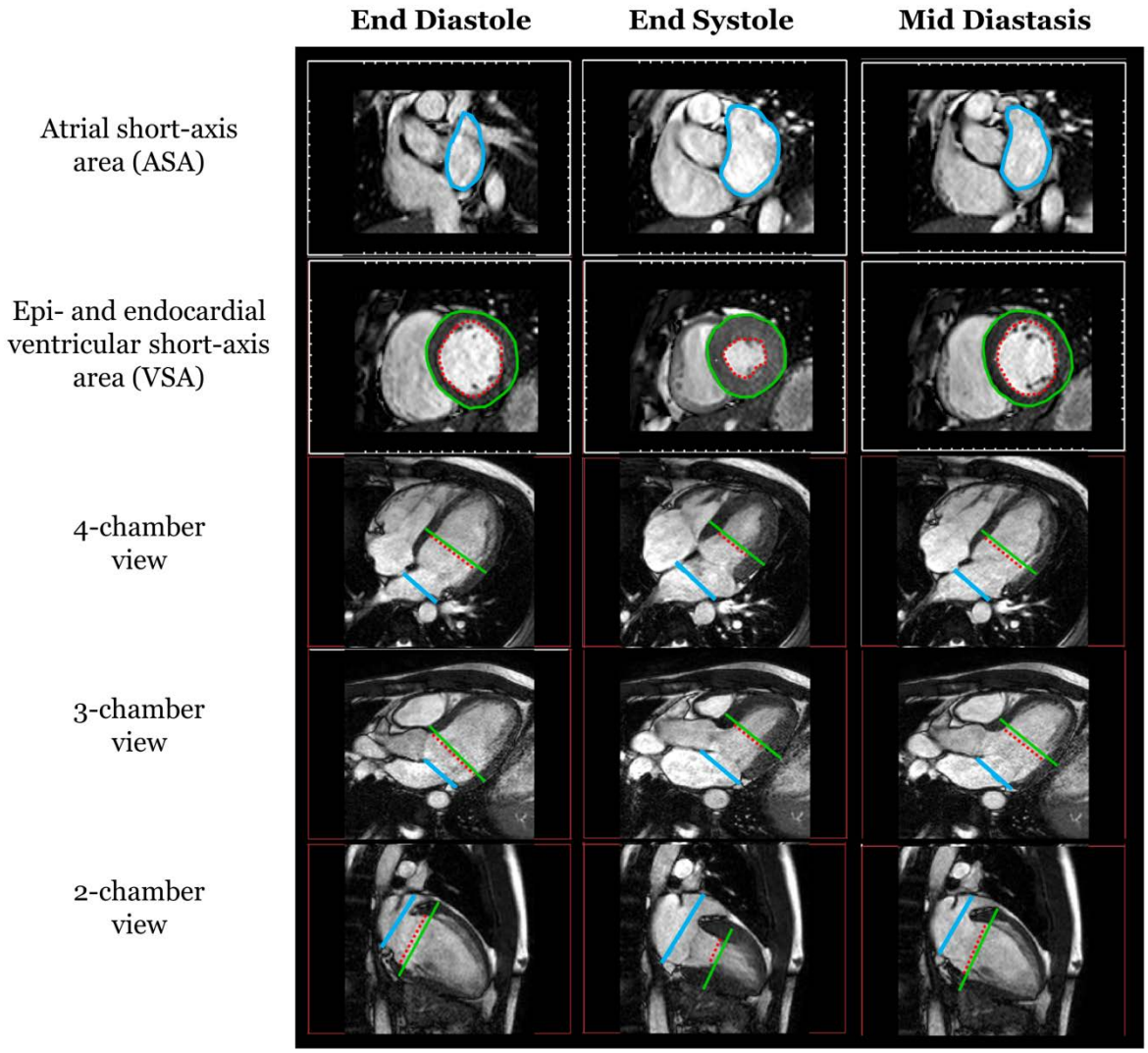

Figure 5.9 – Overview of ASA and VSA measurements in magnetic resonance images. The five views (columns) are shown at end diastole, end systole and the mid diastasis phase of the cardiac cycle (rows). The blue line is the manually delineated ASA, the dashed red line is VSA_{Endo} and the green line is VSA_{Epi}. The short-axis view corresponds to the imaging plane at the level of the blue, respectively green and red, lines in the four-chamber view, three-chamber view and two-chamber view.

5.4 Shear wave elastography

The following sections contain a summary of the materials, methods and software developed to assess the accuracy of the ultrasound-based SWE in **Study IV**.

5.4.1 Phantom construction

Two sets of phantoms were constructed. The first set was fabricated to study the effect of the tissue's macroscopic shape on shear modulus estimation and consisted of phantoms with three different geometries: a plate, a cylinder and a hollow cylinder. This first study will be referred to as the *geometry study*. The second set consisted of arterial phantoms, i.e. hollow cylinders having different stiffness values, which were fabricated to assess the accuracy of SWE for the arterial geometry. This second study will be referred to as the *accuracy study*. The number of phantoms constructed for each phantom geometry is reported in Table 5.5.

All phantoms were constructed of an aqueous poly(vinyl alcohol) (PVA) solution. By using PVA, the phantom's stiffness can be adjusted by freezing and then thawing the material multiple times during manufacturing. An increased number of freeze/thaw (F/T) cycles corresponds to an increased stiffness. The solution contained 87% in mass percentage of de-ionized water, 10% PVA (Sigma-Aldrich, St. Louis, MO, USA) and 3% graphite powder (Merck KGaA, Darmstadt, Germany), which was heated to approximately 65 °C, under constant stirring. The solution, when still liquid, was poured into phantom molds of different shapes.

For the geometry study, the plate phantom was created by pouring the solution in a plastic container of 16 cm length and 13 cm width until the level reached a height of approximately 1 cm. The solid cylinder phantom was created by using the mold shown in Figure 5.10 without the metal rod in the middle, and the hollow cylinder was created with the same mold but preserving the metal rod during the F/T procedure. For the accuracy study, all nine phantoms were constructed by pouring the PVA solution into the mold shown in Figure 5.10. Finally, the phantoms underwent a certain number of F/T cycles, as reported in Table 5.5. A cycle corresponded to 12 hours at −23 °C followed by 12 hours at a room temperature of approximately 22 °C.

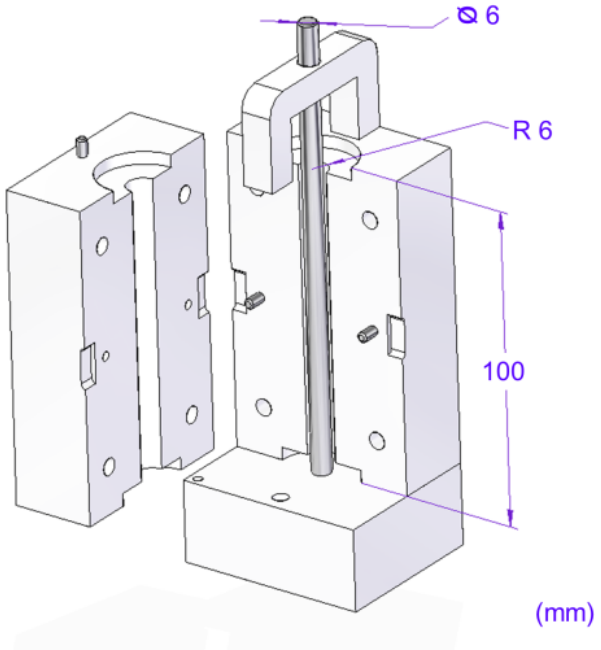

Figure 5.10 – Schematics of the mold used to manufacture the solid and hollow cylinder phantoms. R = outer radius of the cylinders.

Table 5.5 – Number of phantoms constructed for each geometry in Study IV.

	Phantom geometry			**Number of F/T cycles**
	Plate	*Solid cylinder*	*Hollow cylinder*	
Geometry study	2	2	2	3
Accuracy study	-	-	3	3
	-	-	3	4
	-	-	3	5

F/T = freeze/thaw.

5.4.2 Shear wave elastography setup

For the geometry study, the plate phantom was submerged in water in a container, whereas the cylinder and the hollow cylinder phantoms were connected to a customized enclosure, filled with and surrounded by water but not pressurized. For the accuracy study, the hollow cylinder phantoms were connected to the enclosure and pressurized at 60, 80, 100 and 120 mmHg by a water column (Figure 5.11).

The ARF generation and the ultrafast imaging of the propagating shear wave were performed using the commercial ultrasound system Aixplorer with the linear transducer SL 15-4 (SuperSonic Imagine, Aix-en-Provence, France). The ultrasound system was modified with a customized research package that allowed the selection of a region of interest (ROI) where the ARF would be applied. The pushing line was automatically placed in the middle of the ROI and adapted by the Aixplorer system according to the ROI

dimensions. The push focal points were spaced at intervals of 5 mm (Figure 5.12). The user did not have direct control of the push line, but could relocate it by modifying the ROI location and size. The research package also allowed the B-mode images of the shear wave propagation in the form of in-phase and quadrature (IQ) data to be exported. IQ data represent a convenient way of storing radiofrequency data [153].

The Aixplorer system generates shear waves within a tissue by locating multiple pushes (i.e. ARF focal points) along a line at different depths. This is often referred to as a *pushing line* or *supersonic push* [127]. It is worth noting that, in arterial applications, a single push would be sufficient to induce shear waves within the arterial wall [16].

For the geometry study, the pushing line was placed such that the second focal point would lie in the middle of the phantom. For the accuracy study, the pushing line was placed in such a way that the second focal point would lie in the middle of the phantom wall (Figure 5**.12**) and SWE measurements were performed on both the anterior and posterior phantom walls.

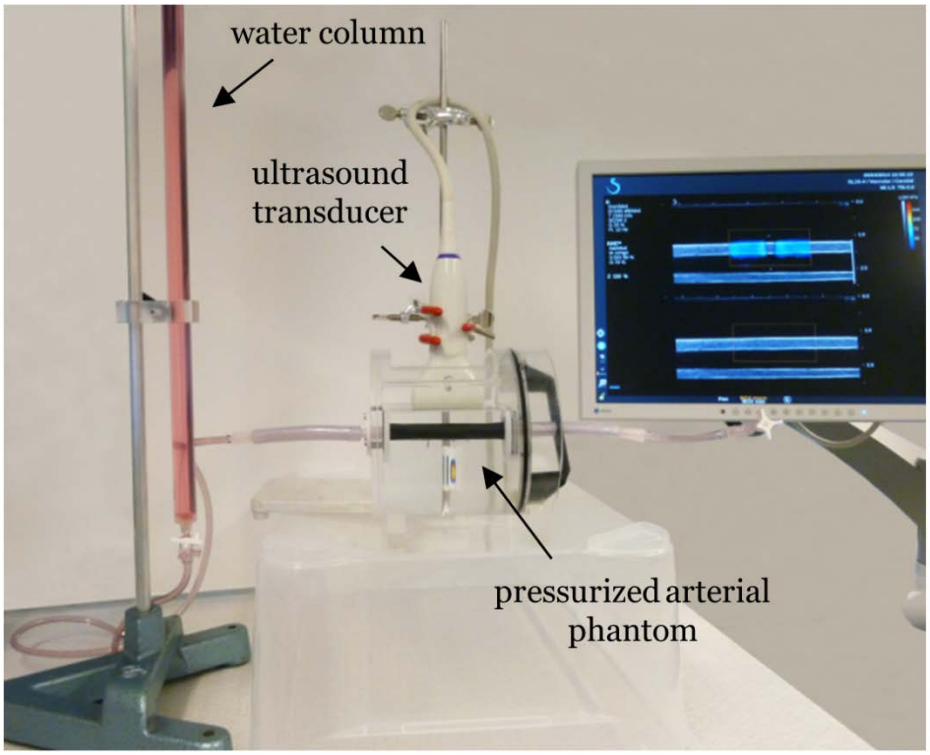

Figure 5.11 – Photograph of the shear wave elastography measurements on a pressurized arterial phantom.

5.4.3 Software development

After the ARF generation in the phantom wall, the shear wave propagation was imaged with 42 frames acquired by ultrafast imaging at a pulse repetition frequency (PRF) of 8000 Hz. When no angle compounding is applied in ultrafast imaging [128], the PRF corresponds to the frame rate since all transducer elements are excited simultaneously. The software development was carried out in MATLAB (R2013b, Mathworks, Natick, MA, USA). A B-mode image was displayed, where five adjacent lines perpendicular to the pushing line were manually selected in close proximity to the push location. A 2-D autocorrelation algorithm [154] was used to measure the incremental displacement field in the axial direction generated during the propagation of the shear wave. An example of the shear wave propagation field can be seen in Figure 5.13, also referred to as an axial incremental displacement map.

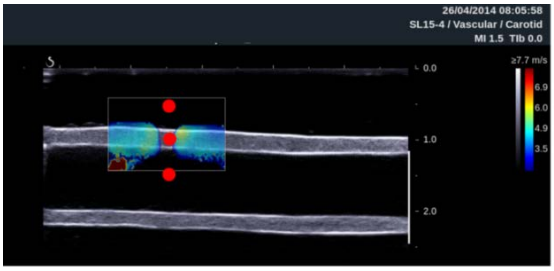

Figure 5.12 – Location of the focal points of the pushing line during shear wave generation in the anterior wall of a hollow cylinder phantom.

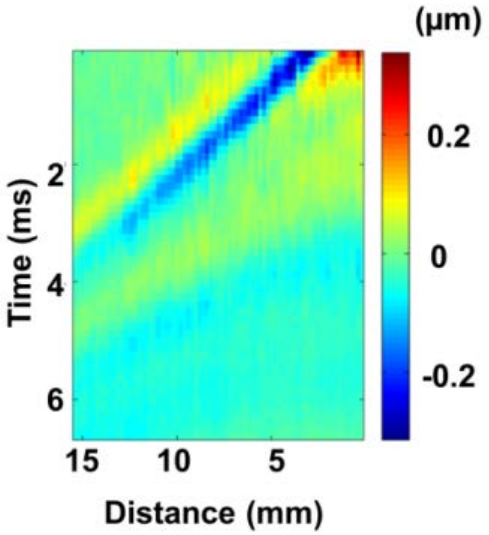

Figure 5.13 – Example of an axial incremental displacement map showing the shear wave propagation in a hollow cylinder phantom. The x-axis represents the distance traveled, the y-axis represents the time of travel and the pixel color represents the axial tissue displacement from the previous time step, i.e. the previous row on the y-axis. The amplitude of the incremental displacement is in the order of a fraction of a micrometer, whereas the total cumulative displacement is in the order of micrometers.

From the axial incremental displacement map, the subsequent post processing steps differed depending on the velocity to be measured, i.e. group or phase velocity.

- *The group velocity* c_g was calculated by computing the Radon transform of the axial displacement map as previously suggested [155]. The Radon transform computes the sum of the pixel values along a particular line in the image, oriented at all possible angles. Therefore, the maximum of the Radon transform corresponds to the angle θ created by the main shear wave front and the x-axis, as shown in Figure 5.14 on the axial displacement map. This angle is related to the speed of the shear wave according to the following relations:

$$\tan(\theta) = \frac{N_x}{N_t} \tag{5.6}$$

$$N_x = \frac{x_t}{\Delta x}, \quad N_t = \frac{t_t}{\Delta t} \tag{5.7}$$

  where N_x and N_t are the number of pixels in the spatial and time dimensions, respectively, and Δx and Δt are the pixel dimensions. The propagation distance is x_t and the propagation time is t_t. The shear wave speed corresponding to the group velocity can therefore be calculated as:

$$c_g = \frac{x_t}{t_t} = \tan(\theta)\frac{\Delta x}{\Delta t}. \tag{5.8}$$

- *The phase velocity* $c_p(f)$ was calculated by Fourier analysis as shown in Figure 5.14. First, the axial incremental displacement map was converted to the frequency domain, or *k*-space. In *k*-space, the *x*-axis is the temporal frequency and the *y*-axis is the spatial frequency, or wavenumber. The k-space was additionally converted to a phase velocity map by dividing each frequency *f* by the wave number *k*, since

$$c_p = \frac{f}{k}. \tag{5.9}$$

  Finally, the phase velocity curve was obtained by selecting the maximum intensity of the phase velocity map at each frequency. This phase velocity curve was then fitted to the plate model equation (4.5) to retrieve the shear modulus μ. The fit was performed considering the entire bandwidth and only for frequencies above 500 Hz. This cutoff was applied because wave propagation in a hollow cylinder can be more closely approximated with wave propagation in a plate at high frequency.

For the geometry study, both group velocity and phase velocity were calculated for all phantoms. After analyzing the results of the geometry study, only the phase velocity for frequencies above 500 Hz was calculated for the accuracy study since it was found to be the most accurate shear modulus estimation method for confined geometries such as hollow cylinders.

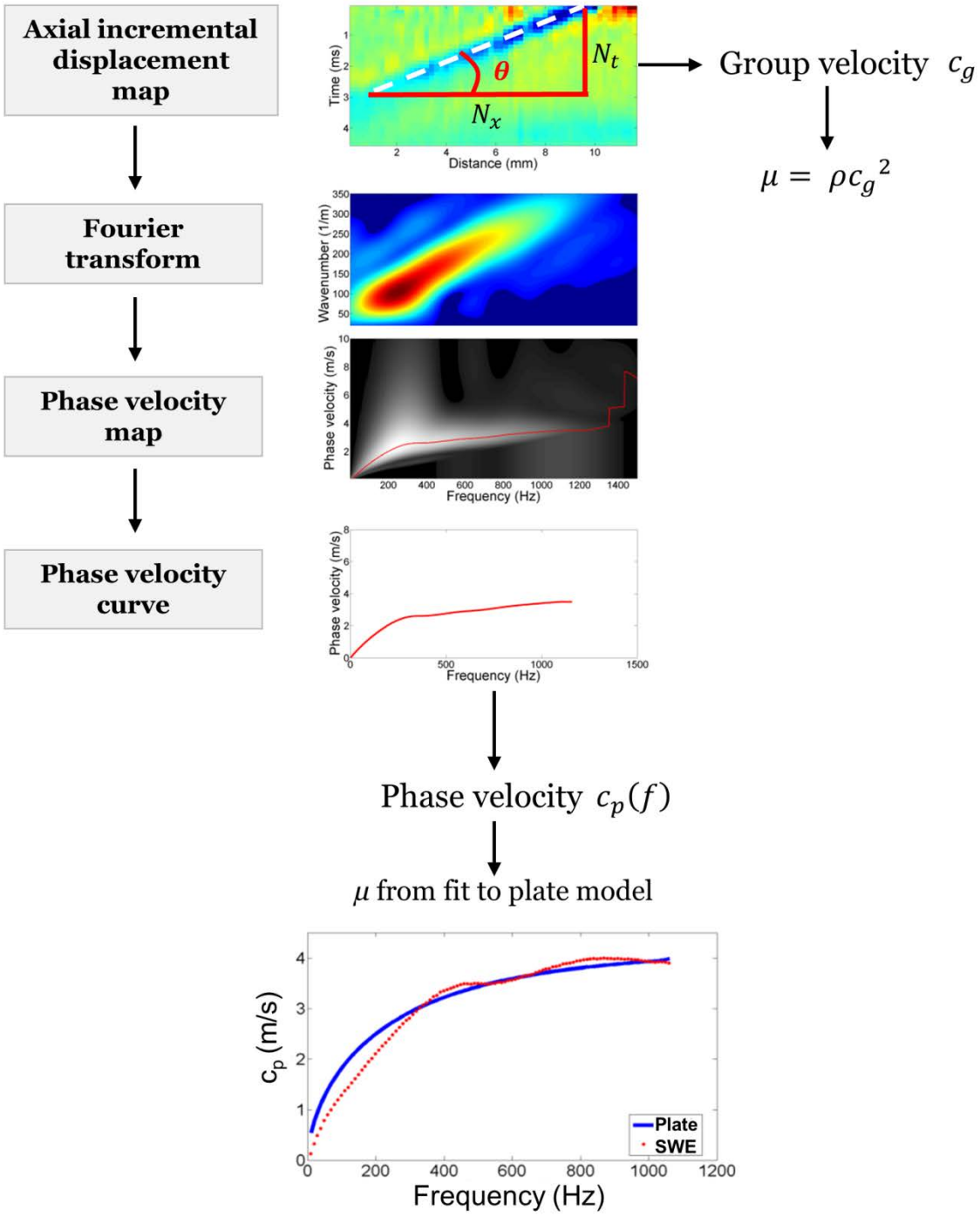

Figure 5.14 – Schematics of the post processing steps used to calculate the shear modulus by group or phase velocity analysis. Group velocity is calculated from the axial displacement map using equations (5.6–5.8). The phase velocity curve is obtained by Fourier analysis. The maximum intensity of the phase velocity map is selected as the phase velocity curve, which is then fit to the plate model in eq. (4.5) to retrieve the shear modulus.

5.4.4 Mechanical testing

The gold standard for characterizing material properties is direct mechanical testing, which in most cases means that the material is compressed or stretched by a known force while the displacement generated in the material is measured. Similarly, one can apply a known deformation while measuring the force generated by the material to oppose this deformation. To validate the shear modulus values obtained by SWE and quantify the error introduced by the technique, the phantoms' material properties, i.e. their shear moduli, were measured by mechanical testing and compared with the SWE results. The phantoms were tested under the same stress conditions as in SWE measurements. Specifically, the phantoms for the accuracy study were pressurized and prestretched in the same way during mechanical testing as they were during ultrasound measurements. Details on the mechanical tests for both the geometry study and the accuracy study can be found in Maksuti et al. [156] and Larsson [157]. An overview of the SWE setup for the accuracy study and the mechanical testing setup can be seen in Figure 5.15.

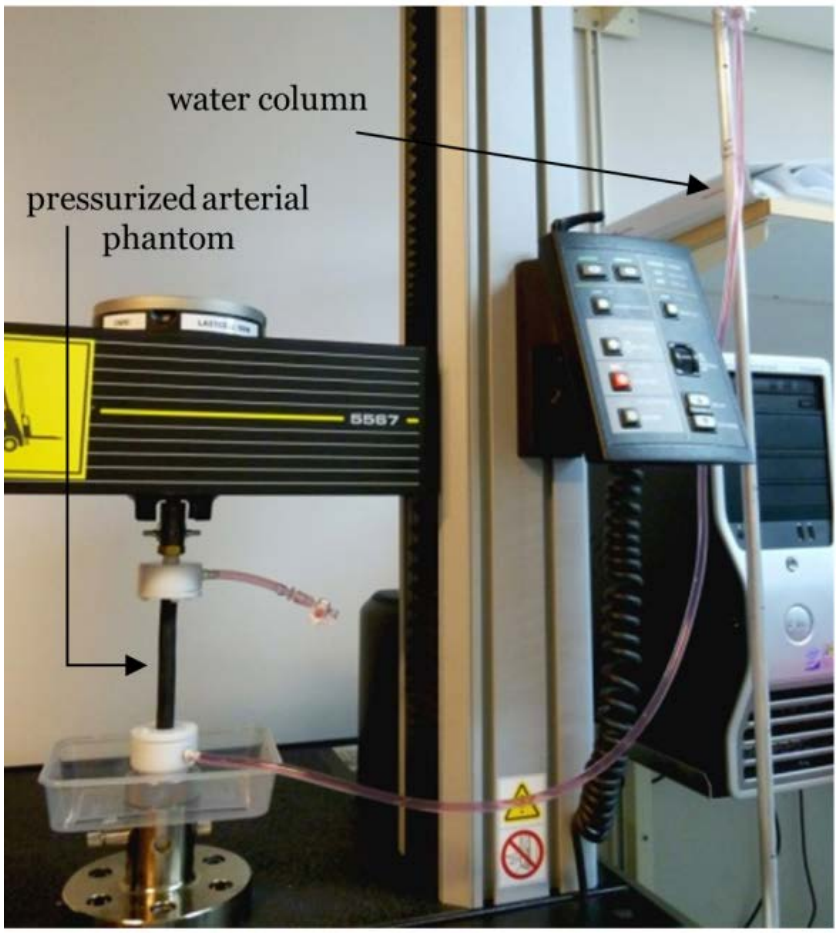

Figure 5.15 – A pressurized arterial phantom undergoing mechanical testing.

5.4.5 Shear wave elastography and mechanical testing comparison

For the geometry study, the difference between the shear modulus estimated using group velocity, phase velocity full bandwidth and phase velocity above 500 Hz, and the shear modulus measured by mechanical testing were compared with a zero-mean distribution using a one-sample *t*-test. For the accuracy study, the difference in shear modulus by SWE between the anterior and posterior walls was also tested with a one-sample *t*-test. Moreover, the errors between SWE measurements and mechanical testing were grouped for different pressure levels, number of F/T cycles and anterior or posterior wall, and compared using a paired-sample *t*-test to assess the presence of systematic errors. The statistical analysis was performed in MATLAB and data are expressed as means ± SD. A p-value of 0.05 was considered to indicate statistical significance.

6 Results

The main results of the four studies are shown in this chapter. Additional results can be found in the articles in the appendix.

Study I: Atrioventricular piston model

The atrioventricular model output reproduced normal physiology in terms of magnitude and direction of changes of the pressure and flow variables in the different compartments of the model. Specifically, left ventricular pressure ranged from 8 to 130 mmHg, aortic pressure from 75 to 130 mmHg and left atrial pressure was approximately 8 mmHg, as can be seen in Figure 6.1. In addition, the AV-piston velocity in the model reproduced the three main features of the AV-plane velocity profile well as measured by ultrasound tissue velocity imaging (Figure 6.2), namely the peak systolic velocity s', the peak early diastolic velocity e' occurring during rapid filling and the peak late diastolic velocity a' occurring during atrial contraction.

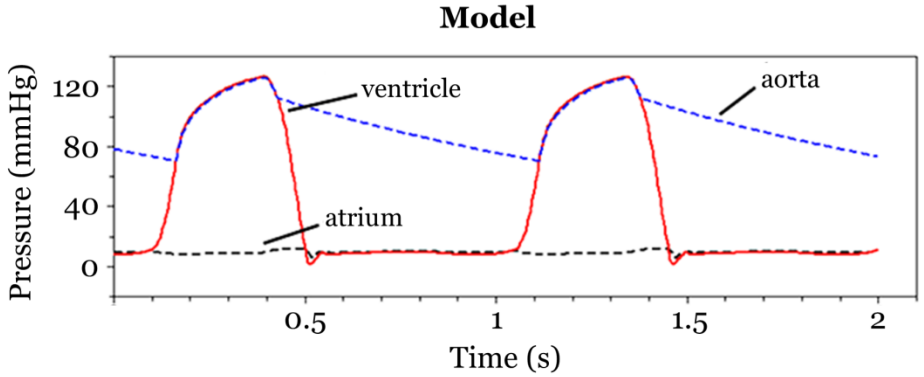

Figure 6.1 – Simulated pressures using the atrioventricular-piston model.

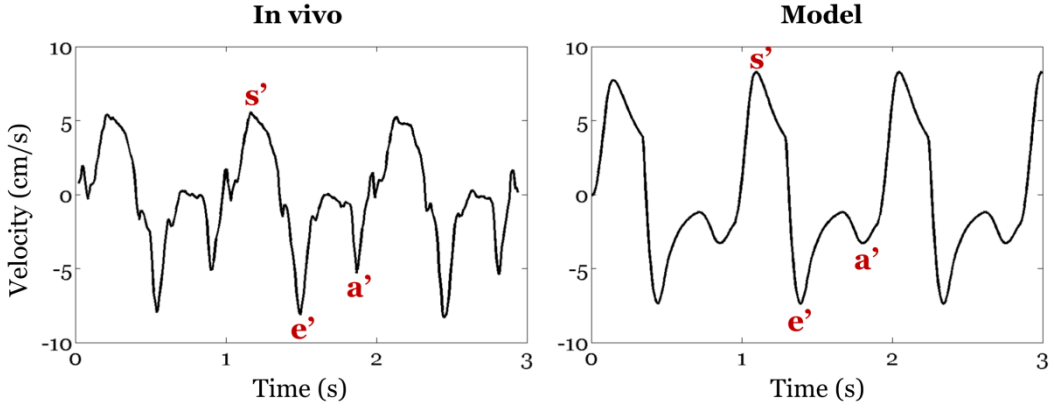

Figure 6.2 – Comparison between the atrioventricular(AV)-plane velocity in a heathy subject (*in vivo*) and the simulated AV-piston velocity using the AV-piston model.

The AV piston velocity was influenced by the magnitude of the systolic contraction force and by the difference in area between the atrial and ventricular piston sides. A reduction of the force by 10% produced a decrease in s' and e' of 11% and 13%, respectively. If A_1 was set equal to A_2, eliminating the hydraulic force, the velocity at mid diastasis decreased from 1.1 cm/s to 0.4 cm/s.

Study II: Demonstration and quantification of hydraulic forces

The physical model of the left atrium and ventricle shown in Figure 6.3 illustrates the effect of hydraulic forces. The two chambers of the Plexiglas model are at the same pressure because of a cavity in the middle of the piston, which allows water to freely move from one chamber to the other. In Figure 6.3, the water column (a) is needed to generate a high enough pressure to overcome friction during the piston's spontaneous displacement. In (b), the piston is manually moved toward the largest chamber while water is being relocated within the smaller chamber and the water column. This phase represents ventricular contraction. Once the piston is released, it moves back to its initial position under the effect of hydraulic forces (c). This phase represents ventricular filling.

The geometry of the physical model can be compared to that of the left side of the heart as previously explained in relation to Figure 5.8. Similarly to the physical model, in the heart, the VSA must be larger than the ASA in order to generate a hydraulic force on the AV-plane acting in the apex-to-base direction.

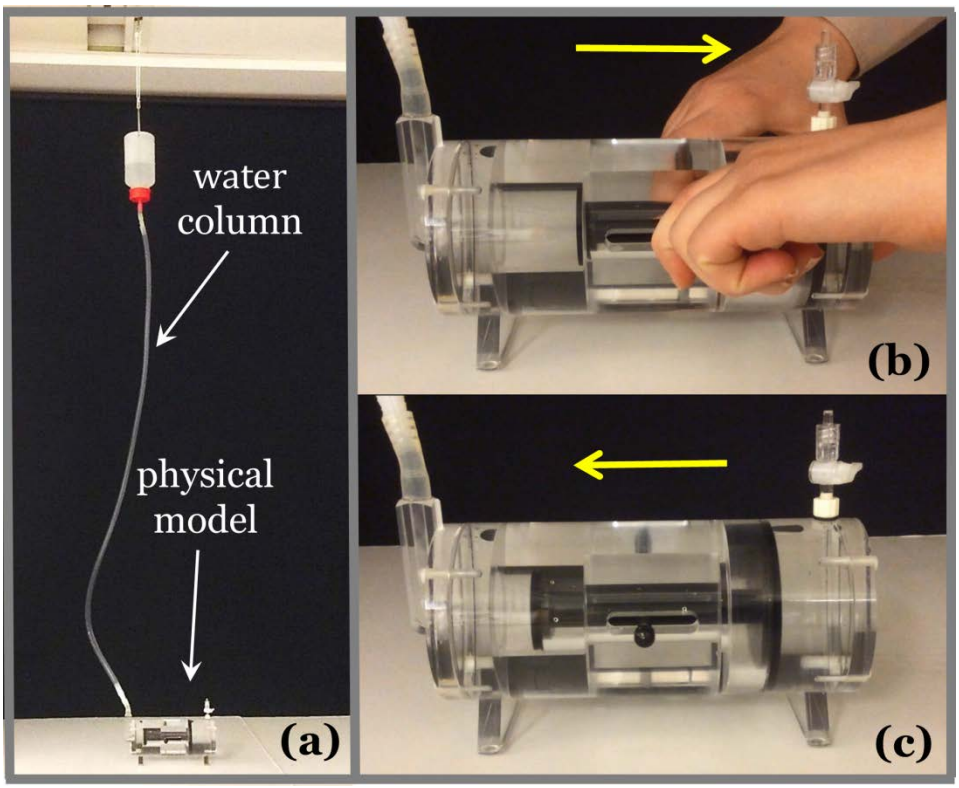

Figure 6.3 – Photographs of the physical model showing hydraulic forces in action. (a) Overview of the physical model connected to a water column for pressurization; (b) piston manually moved to mimic ventricular contraction; (c) piston moving under the effect of hydraulic forces – this is similar to what occurs during ventricular filling.

In vivo measurements in heathy volunteers showed that VSA was greater than ASA during the largest part of diastole, enabling the creation of hydraulic forces that aid filling. This can be seen in Figure 6.4, where VSA_{Epi} is larger than ASA during all of diastole and VSA_{Endo} is larger than ASA for 75% of the diastolic phase. In addition, measurements of the cross-sectional areas for each individual during diastasis are reported in Table 6.1. VSA is greater than ASA for all subjects during diastasis, generating hydraulic forces in the range 0.2–2.1 N when considering VSA_{Endo}, and in the range 2.0–5.0 N when considering VSA_{Epi}. The hydraulic force is therefore of the same order of magnitude as the estimated peak driving force during left ventricular rapid filling (5–10 N, see section 5.3.3).

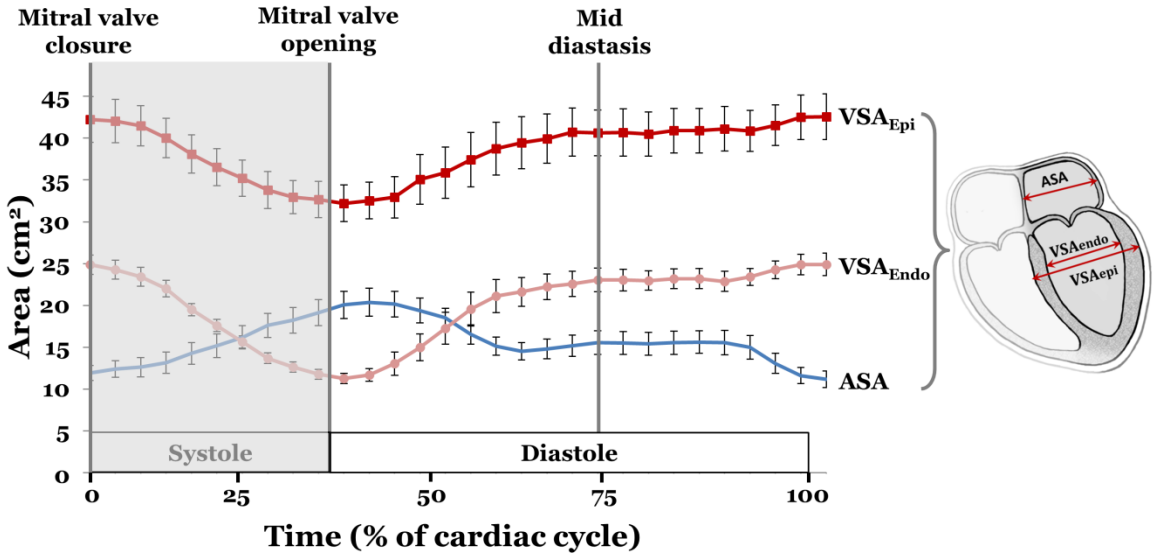

Figure 6.4 – Time-resolved atrial and ventricular short-axis areas in the left ventricle. The three curves represent the mean value for all subjects (n=10) for the corresponding area. Vertical lines denote end diastole (mitral valve closure), end systole (mitral valve opening), and mid diastasis. It can be noted that VSA_{Epi} is larger than ASA for the entire duration of diastole, and that VSA_{Endo} is larger than ASA for the majority of the duration of diastole. The error bars denote the standard error of the mean.

Table 6.1 – Maximum left ventricular short-axis areas for all subjects at mid diastasis.

Subject	ASA (cm^2)	VSA_{Endo} (cm^2)	VSA_{Epi} (cm^2)	Hydraulic force* with VSA_{Endo} (N)	Hydraulic force* with VSA_{Epi} (N)
1	15.3	22.7	38.2	1.0	3.1
2	12.3	22.7	40.5	1.4	3.8
3	11.9	16.5	27.2	0.6	2.0
4	14.9	20.6	34.0	0.8	2.5
5	24.3	26.4	52.1	0.3	3.7
6	21.6	23.3	39.9	0.2	2.4
7	14.9	23.8	38.8	1.2	3.2
8	11.0	19.8	35.1	1.2	3.2
9	12.3	28.1	50.1	2.1	5.0
10	16.7	28.1	53.1	1.5	4.8

*Assuming mean left ventricular diastolic pressure is equal to 10 mmHg.

Study III: Ventricular–arterial aging

Simulations of the ventricular–arterial interaction model at different decades when only arterial aging and when arterial and cardiac aging combined are included are shown in Figure 6.5. The simulations are compared with population data. The comparison shows that when cardiac and arterial age-related changes are combined, simulated systolic and diastolic pressures better reproduce the trends shown in the population data. When performing a quantitative comparison, the normalized RMSE for the simulations with arterial and cardiac changes combined was lower than for arterial changes alone (5.1 vs 10.7%).

The gray line in Figure 6.5 indicates the amplified systolic pressure introduced to account for aortic–brachial pressure differences. When this amplification is added, the model's systolic pressure better reproduces the population data at young ages. At older ages, the amplified pressure underestimates the population data for arterial changes alone and overestimates the population data for cardiac and arterial changes combined. Also, when this amplification was included, the normalized RMSE for the simulations with arterial and cardiac changes combined was lower than for arterial changes alone (5.9 vs 7.7%).

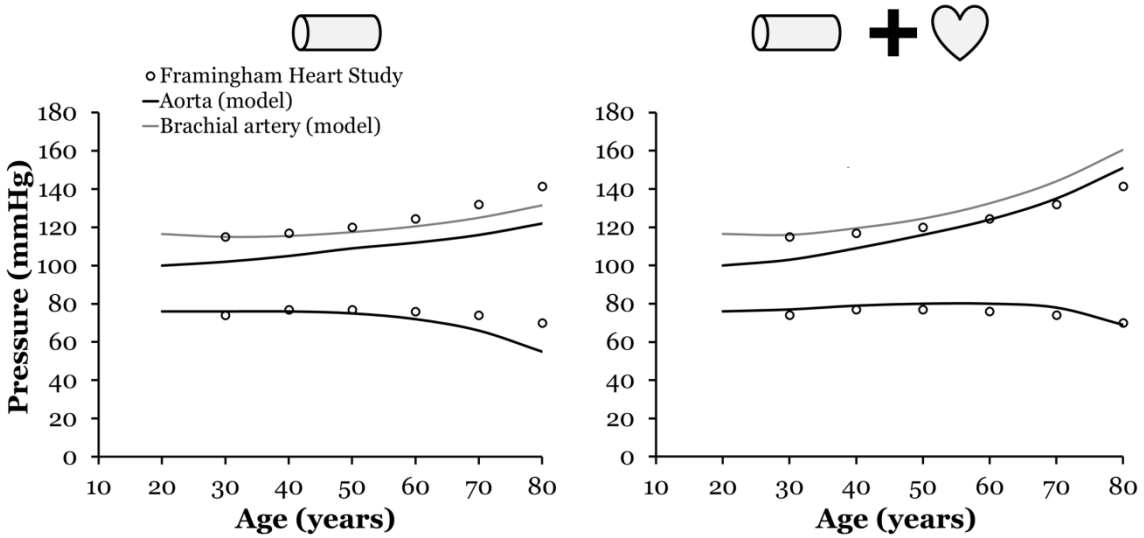

Figure 6.5 – Comparison between simulated arterial pressures and population data when considering arterial aging alone (left) and arterial and cardiac aging combined (right). The upper line represents the systolic pressure and the lower line the diastolic pressure in each figure part. The thin gray line indicates systolic pressure when accounting for aortic-to-brachial pressure amplification.

Study IV: Arterial stiffness by shear wave elastography

An experimental setup including tissue-mimicking phantoms of different geometries, pressurized arterial phantoms and in-house software was developed to measure arterial stiffness by SWE. Shear modulus estimations were then validated by mechanical testing. The main results from the SWE geometry and accuracy study are presented in this section.

Geometry study

The comparison between the three shear modulus estimation methods (group velocity, phase velocity full bandwidth and phase velocity above 500 Hz) and mechanical testing showed that phantom/organ geometry significantly influences shear wave propagation and the estimation of mechanical properties (Figure 6.6). Group velocity analysis underestimated the shear modulus in all three confined geometries. In the plate phantom, phase velocity analysis considering the full bandwidth resulted in the best estimation, with no statistically significant difference from mechanical testing. For the solid cylinder, all methods were significantly different from mechanical testing but phase velocity analysis resulted in a more accurate shear modulus estimate than did group velocity analysis. For the hollow cylinder (arterial phantom), the analysis of phase velocity above 500 Hz resulted in the most accurate estimation ($\mu = 30.6 \pm 3.2$ kPa), with no significant difference from the reference value obtained by mechanical testing ($\mu = 30.5 \pm 0.4$ kPa). Comparison of the different shear modulus estimation methods with the gold standard measurement suggested that phase velocity analysis at high frequencies should be used to derive μ in hollow cylindrical geometries, e.g. in arteries.

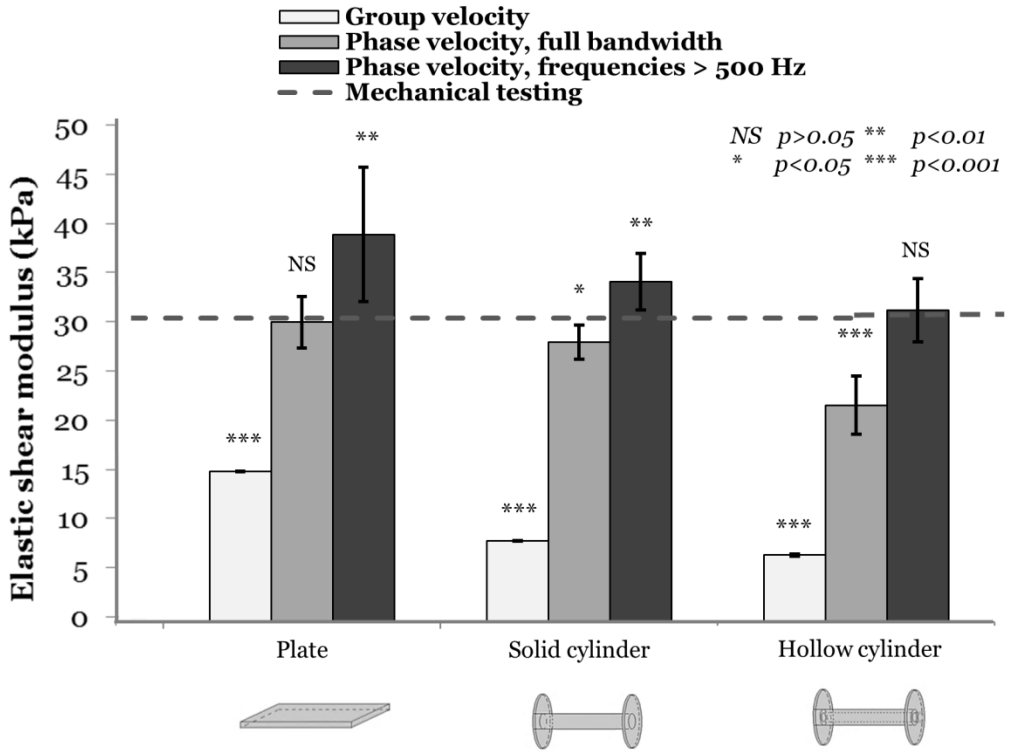

Figure 6.6 – Results from the geometry study. The p-value indicates the statistical significance between the different analysis methods and mechanical testing, with n= 12 (2 phantoms, 3 repeated pushes for left and right shear waves). NS = non-significant.

Accuracy study

Shear modulus obtained with SWE by phase velocity analysis at frequencies above 500 Hz and mechanical testing for pressurized arterial phantoms is shown in Figure 6.7. As expected, phantom stiffness increased with the number of F/T cycles and with increasing intraluminal pressure. SWE showed good agreement with mechanical testing at all different pressure levels and number of F/T cycles with a mean absolute error of 5.6 ± 4.1 kPa, corresponding to a relative error of 8.8 ± 6.0%. The relative error did not vary significantly between measurements when grouped for different values of intraluminal pressure, F/T cycles and measurement location in the anterior or posterior wall. This implies that significant systematic errors where not present.

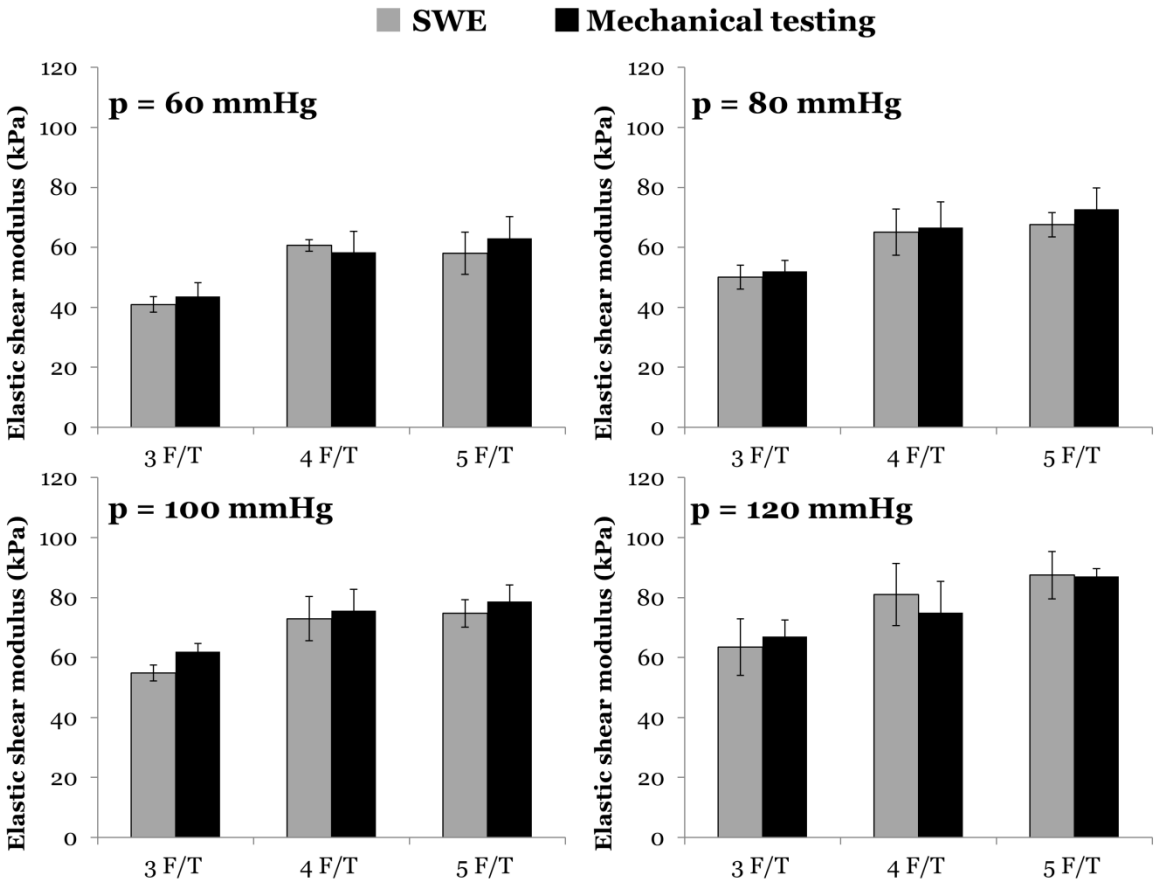

Figure 6.7 – Results from the accuracy study. Shear wave elastography (SWE) values are estimated by phase velocity analysis at frequencies above 500 Hz. F/T = freeze/thaw.

7 Discussion

The application of engineering principles to medicine has only been recognized in the last few decades as a separate field of research, namely biomedical engineering. However, history offers many examples of engineering work combined with medicine, as demonstrated by, among others, Leonardo da Vinci, William Harvey and Arthur Guyton. The human body is a physical system and can therefore be studied in engineering terms. Furthermore, well-designed medical devices can characterize, enhance or substitute some of the human body's functions. However, biology in general presents a higher level of complexity than engineering because of the high interpersonal variations and the large number of chemical and physical interactions occurring simultaneously in the human body. Therefore, the field of biomedical engineering faces many challenges.

The aim of cardiovascular imaging and modeling, which is also the aim of this thesis work, is to help clinicians and the medical devices industry to better understand the mechanisms involved in cardiovascular pathophysiology, in order to improve cardiac diagnostic procedures, devices design and their interaction with the cardiovascular system. Cardiovascular pathophysiology still has many unresolved issues that can be addressed via an engineering approach. In particular, mechanisms involved in cardiac mechanics, more specifically in diastolic ventricular filling, are being investigated extensively in current cardiovascular research [28,29,49,158–161] and were addressed in the first two studies of this thesis. Studies I and II described the contribution of hydraulic forces to ventricular filling, which to my knowledge has not been quantified systematically previously. This was done by modeling cardiac function as a piston pump with the AV plane as a piston unit and by assessing the prerequisites for the generation of hydraulic forces *in vivo* in magnetic resonance images. The heart works in close connection with the vascular system and therefore the arterial–cardiac interaction must be taken into account when evaluating cardiac function. Study III exemplified and quantified the contribution of the heart and the arterial system to blood pressure changes with age. Increased arterial stiffness has been shown to be an independent risk factor for cardiovascular events [73,162] and is one of the main causes of blood pressure changes during aging [36], as confirmed by the results in Study III. However, commercially available techniques for measuring arterial stiffness suffer from several limitations [115,163] and therefore new techniques are being developed [21]. In Study IV, the ultrasound-based technique SWE was further developed for measurements of arterial stiffness and validated against a reference method. SWE has the potential to measure arterial stiffness locally and multiple times during the cardiac cycle.

During this thesis work, ultrasound imaging and MRI were chosen as suitable imaging modalities since they do not make use of ionizing radiation and are therefore suitable for initial diagnostic purposes and screening of heathy volunteers in basic research. In the following paragraphs, the main outcomes and implications of the four studies will be described, followed by a general discussion about the limitations of the methodology.

7.1 Hydraulic forces and cardiac function

7.1.1 *In silico:* modeling

The cardiac model developed in Study I offers a novel approach to cardiac modeling. The model is based on physiological observations rather than predefined mathematical functions derived from experimental measurements. The advantage of this approach is that it reproduces both the desired outputs and aids understanding of the underlying physical principles of cardiac mechanics. The major use of the model in Study I was to test whether the pumping function by longitudinal movements of the AV plane could be a relevant mechanism in cardiac pumping. The model reproduced physiological pressure outputs well (Figure 6.1), both in terms of magnitude and direction of changes, supporting the hypothesis that longitudinal function and hydraulic return are significant contributors to cardiac pumping. In addition, the model was able to reproduce atrioventricular plane velocity curves (Figure 6.2). Few previous models have addressed AV interactions *per se*, but have considered the AV-plane motion as a local phenomenon [164] or assumed that atrial and ventricular cross sections are equal [165]. A recent 3D model studied the effect of boundary conditions, in particular of the presence of the pericardium, on AV-plane displacement magnitude [166]. To my knowledge, no model in the scientific literature has addressed and modeled AV-piston motion as the main source contributing to cardiac pumping function.

All models are simplified abstractions of reality and can only reproduce part of a system's behavior. This necessarily applies also to the cardiac model suggested in this thesis. When more closely analyzing the model output, the following two observations can be made: the peak early systolic velocity e' occurs before mitral valve opening, which does not correspond to what happens in the real heart where e' occurs immediately after mitral valve opening; and the AV piston does not reach an equilibrium position during diastasis. These observations suggest that a more accurate modeling of myocardial mechanical properties and elastic recoil are necessary to accurately reproduce timing of the main cardiac events. Specifically, the myocardium was modeled with a constant compliance value throughout the heart cycle (further explanation below), which is an incorrect assumption, given that the myocardium becomes much stiffer during the contraction phase than it is during diastole. Additionally, no elastic recoil was included in the piston unit. These simplifications were motivated by the intention to develop a linear model, with the minimum number of parameters necessary to capture and describe the contribution of hydraulic forces alone. The aim was therefore not to fully reproduce cardiac mechanics in a single complex and comprehensive model. Additionally, faults can more easily be identified in simple models. The main advantage of increasing model complexity could be the ability to better differentiate the contribution of the different factors affecting the system's dynamics. However, there is a risk inherent in complex models related to the large number of parameters, which give rise to parameter identification problems and complicates the validation process.

Another simplification in the model was the absence of passive tension [30], which prevents the myocardium from stretching excessively. In the model, if there is a difference in area between the two piston heads, there is a force pushing the piston toward the atrium

and no other force impedes this movement. This implies that the AV piston does not reach any equilibrium position and keeps moving toward the atrium until the next ventricular contraction starts.

Ongoing work aims at integrating elastic recoil and passive forces into the model, by e.g. adding a spring to the piston unit. This spring would represent both elastic recoil, when compressed, and passive forces, when stretched. By adding this component, the AV-piston reaches equilibrium if diastasis is sufficiently long.

Parameter selection is a complex task in cardiovascular modeling since most cardiovascular parameters cannot be measured directly. Increasing the number of parameters in a model substantially increases the complexity of the parameter selection process. This may result in arbitrary and empirical choices that can influence the model's output in unpredictable ways. Even for simpler models, such as the Windkessel model, a unique and physically consistent parameter selection can be challenging to achieve [140]. A possible solution is to use a systematic approach and define parameters' values based on theoretical assumptions and the system's geometry [10]. Another interesting approach is to implement adaptation rules based on known physiological control mechanisms present in the cardiovascular system that automatically assign parameter values [167]. In this thesis, a combination of these approaches was used. In Study I, the parameters of the AV-piston model were based on literature findings and theoretical assumptions. In Study III, the arterial changes were based on literature values and cardiac changes were based on adaptation rules.

The theoretical assumptions used to derive the parameters of the AV-piston model (Figure 5.4) in Study I will be now briefly described. Concerning the vein compartment, given that the compliance of the entire circulation is approximately 170 mL/mmHg [139], the systemic venous compliance was assumed to be in the order of 50 mL/mmHg. Atrial and ventricular compliances were chosen as constant and equal to 0.3 mL/mmHg. The reason for choosing a constant compliance was, as previously mentioned, to keep the model as simple as possible with the aim of investigating only the hydraulic force effect, and not that in combination with myocardial complex mechanics. Chamber compliance was also needed for numerical reasons—a completely stiff chamber would have resulted in numerical instability and output oscillations. The constant compliance value was chosen to be equal to the minimum compliance (or maximum elastance) in the time-varying elastance model [10,137], which represents the maximum chamber stiffness. An increase/decrease of 20% in the constant value of atrial compliance had very little influence on output variables in the AV-piston model. The same change in the constant ventricular compliance slightly influenced mitral flow and duration of isovolumetric phases. However, it should be noted that in the AV-piston model, most of the volume changes in the cardiac chambers are caused by movements of the AV piston rather than by changes in the compliance as described by the time-varying elastance model. Therefore, a direct comparison of the two approaches is difficult to make. Finally, resistance to flow in the valves was set to a constant value in order to generate the maximum pressure drop across the valve reported by echocardiography data for healthy individuals [97].

7.1.2 *In vitro:* physical model

The physical model constructed in Study II served to illustrate in a simple and intuitive way the effect of hydraulic forces on a hollow piston with different areas (Figure 6.3). This is similar to what occurs in the human heart when the atrial cross section is smaller than the ventricular cross section, and there is a negligible pressure difference between the two chambers.

7.1.3 *In vivo:* left atrial and ventricular short-axis areas

Measurements of short-axis areas by MRI in healthy volunteers showed that VSA is larger than ASA for almost all of diastole (Figure 6.4). VSA was measured when both including and excluding the LV myocardium. The rationale for excluding the myocardium is that the blood is in direct contact with the endocardial border. The rationale for including the myocardium is that the interstitial pressure within the myocardium [168] and possibly the blood pressure in the coronary arteries, which is highest during diastole, may generate intramyocardial erectile hydraulic forces that contribute to filling [34,35]. When considering the myocardium in the measurement of VSA, VSA was greater than ASA for the entire duration of diastole. The largest difference between VSA and ASA occurs during diastasis, when the transmitral pressure gradient present during early filling has evened out [169]. Therefore, the difference in short-axis area between the two cardiac chambers represents the basis for the generation of a hydraulic force pushing the AV plane toward the base of the heart. This implies that the hydraulic force aids LV lengthening during diastole and facilitates LV filling. The hydraulic force reaches its maximum intensity during diastasis, when elastic stored energy has already been consumed. This mechanism is therefore complementary to elastic recoil, which is predominant during rapid filling in early diastole. The comparison between hydraulic forces and the previously estimated peak driving force shows that they are of similar magnitude. Based on the results of Study II and on other known mechanisms of diastolic filling that act on a molecular level (see section 4.1.1), the forces acting during diastole can be summarized schematically as in Figure 7.1. These results bring new insights to diastolic function and have important clinical implications. Specifically, they suggest that the macroscopic geometry of the atrium in relation to the ventricular geometry is important for an effective filling of the left ventricle. Notably, atrial enlargement is a typical sign of elevated filling pressure and diastolic dysfunction [170]. In addition, an increase in left atrial size is a risk factor for atrial fibrillation and thrombus formation, as well as an indication for negative prognosis in heart failure [171]. Nevertheless, the mechanisms generating the enlargement of the atrium and the effect of increased atrial size are not completely understood.

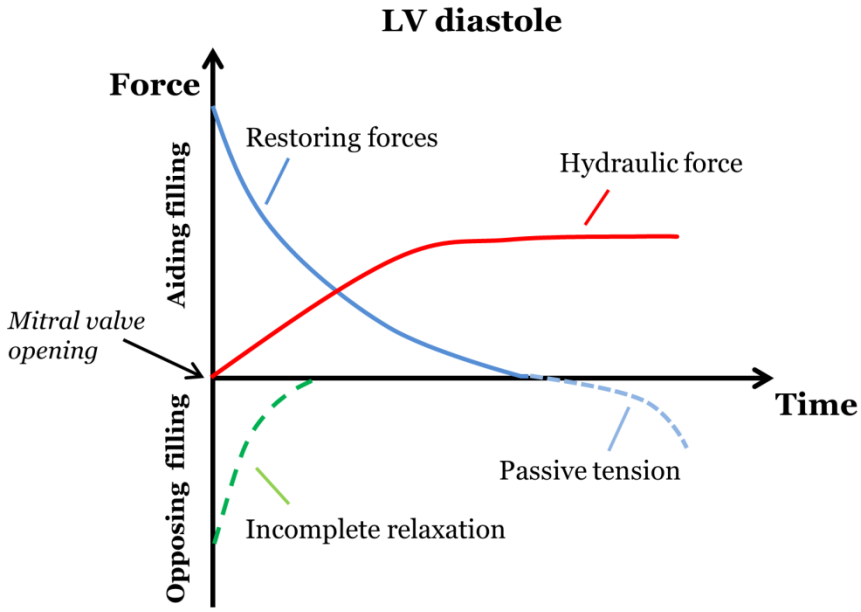

Figure 7.1 – Schematic representation of the forces acting during left ventricular filling. Restoring forces, passive tension and incomplete relaxation act on a molecular level within the myocardium. The hydraulic force is generated on a macroscopic level and is a consequence of the diastolic blood chamber pressure acting on the anatomic surfaces of the heart.

In clinical practice, atrial long-axis area is a diagnostic index of diastolic function [96], whereas the short-axis area is not usually measured. The physics behind the hydraulic force generation suggest that ASA, in relation to VSA, is a particularly important index for diastolic function assessment. If the sensitivity and specificity of short-axis area measurements are confirmed by future clinical studies, this might have a significant impact on both recommendations for diastolic function assessment and in cardiac surgery, where a reduction in atrial size could be complementary to other invasive interventions in treating impaired diastolic function.

7.1.4 Additional implications of longitudinal pumping

An incorrect mental model of the deformation pattern of the heart *in situ*, such as a pumping action achieved by squeezing, generates misunderstandings that might have negative outcomes on, e.g. the interpretation of medical images, the design of medical devices [172] and the modeling of cardiac function [173,174]. The heart's pumping mechanism is still described as a squeezing action with large volume changes in many physiology books [57,175], during physiology classes and in cardiac illustrations and animations (the reader is invited to search the web for images and videos of "the cardiac cycle"), despite the fact that the constancy of total heart volume is well known within the research community and is clearly visible in medical images (Figure 4.12 and Figure 4.15). However, neither these research outcomes nor the medical images are easily available to a large public and their interpretation is less straightforward than colorful and nicely drawn medical animations. Therefore, an effort should be made to more effectively spread what is already known in the research community to the general public, including students,

healthcare professionals and engineers in the medical technology industry. Study I shows an example of how knowledge of longitudinal cardiac pumping can be integrated into cardiac models. Study II shows how this knowledge can be used to generate hypotheses about forces involved in diastolic filling and how the preliminary modeling work could guide *in vivo* studies. Additionally, based on the knowledge generated during this thesis work four important implications can be identified that derive from the awareness of cardiac longitudinal pumping as opposed to a squeezing mechanism (Figure 4.5). These implications will be briefly described below.

The flow through the valves measured by Doppler ultrasound does not perfectly correspond to the flow through the valve leaflets, since the cardiac valves are attached to the moving AV plane. Therefore, there is a relative motion of blood with respect to the leaflets that is not captured by the Doppler signal, which measures the movement of blood with respect to the transducer. This implies, for instance, that blood can be relocated from the atria to the ventricles without actually moving with respect to the transducer—the valves themselves move while the ventricles lengthen. Valve motion is in the range of 1–2 cm and is therefore not a negligible contribution.

Measurements of mitral annulus excursion, often referred to as mitral annular plane systolic excursion (MAPSE) [176], and tricuspid annulus displacement, often referred to as tricuspid annular plane systolic excursion (TAPSE) [177], are not only local myocardial measurements but are rather the sum of the longitudinal displacement from the apex to the AV-plane region [178], since the apex is fixed in the longitudinal direction. Therefore, MAPSE and TAPSE can be considered as global measures of ventricular systolic and diastolic function [178]. Furthermore, MAPSE and TAPSE are tightly related to AV-plane displacement measurements since both the mitral and tricuspid valves are located in the AV plane.

Another implication of longitudinal pumping concerns open-heart surgery. An important prerequisite for preserving the total heart volume and enabling longitudinal pumping is that the pericardium is intact, limiting large cardiac volume changes [13,46,47]. During heart surgery, the pericardium is cut and usually not sewn together again before closing the chest. This implies that myocardial displacement patterns and hemodynamics in patients undergoing open-heart surgery vary from other less-invasive innervations and from before the intervention [179]. This occurs because of the positive effect of the intervention itself, such as, e.g. valve replacement or improvement of coronary arterial blood supply, but also because of the reduced constraints caused by the open pericardium, which might produce negative effects on cardiac mechanics. Notably, reduced longitudinal function after open-heart surgery is a known phenomenon, particularly on the right side of the heart [179]. However, the underlying mechanisms causing this reduction and abnormal septal motion remain unclear [179–181]. Clinical studies where the pericardium is sewn together at the end of open-heart surgery are therefore appropriate, although it should be taken into account that pericardial closure may in the short term result in an increased risk of postoperative cardiac tamponade, i.e. accumulation of blood in the limited pericardial space.

Medical devices or prostheses such as percutaneous valves with integrated stents are usually tested to withstand repeated radial deformations. However, both the aortic and

pulmonary outflow tracts are attached to the AV plane and undergo a much more complex deformation pattern than simple radial expansion. Data show that these devices are prone to rupture [182] and that more accurate patient-specific deformation patterns and modeling are useful in predicting fracture location [172].

7.2 Cardiovascular aging

Aging is a complex process that is difficult to describe and predict systematically. However, some key factors that drive the most significant changes can be identified. This can help find targets to aim for so as to delay or reduce the negative effects of aging. The aim of Study III was to focus on the biomechanical interactions between the heart and the vascular system. The common understanding is that arterial changes, such as an increase in arterial stiffness and increase in vascular peripheral resistance, can explain blood pressure changes with age [36]. Compensatory hypertrophy is well known, but despite this, the role of the heart in blood pressure changes is often not taken into account. Simulation results compared with longitudinal population data showed that also the heart, and not only the arterial system, contributes to the blood pressure changes with age. Notably, simulations with arterial changes alone did not properly reproduce the population data. When cardiac changes where included, the agreement between simulations and population data improved (Figure 6.5). The changes in arterial properties were assumed to initiate the blood pressure changes. Cardiac remodeling followed, further contributing to the development of blood pressure.

Both an increase in arterial stiffness and an increase in cardiac contractility, as a consequence of hypertrophy, produce a systolic pressure increase. On the other hand, an increase in E_{ed} produces a decrease in systolic and diastolic pressure. The combination of these parameter changes allowed a stable solution for each age decade to be reached that respected both the rules set for the parameter selection (Figure 5.6). However, in the real cardiovascular system, these changes occur continuously and are not discrete events. This implies that once this vicious cycle is initiated, blood pressure development continues until it turns into hypertension. Treating arterial stiffness might therefore prevent hypertrophy, reducing the risk of further hypertension. Notably, the most effective drugs for treatment of hypertension act on mechanisms that involve both the heart and the arterial system. For instance, beta blockers have the effect of reducing heart rate and contractility, which corresponds to a reduction of E_{es} in the model, and therefore a reduction in systolic pressure. Angiotensin-converting enzyme inhibitors and angiotensin receptor blockers inhibit the renin–angiotensin system, causing an immediate vasodilatation and reduction of both cardiac and vascular remodeling in the long term. The effects of these drugs are therefore useful to limit or slow down the vicious cycle of cardiac remodeling induced by increased systolic pressure (Figure 5.6).

It still remains unclear which vascular changes occur first—whether it is the increase in arterial stiffness or in peripheral resistance. Arterial stiffness increases because of the fatigue and fracture of elastin within the arterial wall and consequent transfer of stress to the stiffer collagen [36,183]. Structural and functional changes of the peripheral vasculature may be the cause of the resistance increase with age [184]. However, this could also be the result of a regulatory mechanism to maintain coronary perfusion, given that

coronary arteries fill with blood during diastole and an adequate pressure level in the aorta during this phase is necessary to guarantee coronary flow. During aging, the increase in arterial stiffness causes systolic pressure to increase and diastolic pressure to drop. At the same time, an increase in peripheral resistance causes both systolic and diastolic pressure to rise. Therefore, the increase in resistance has, on the one hand, the negative effect of increasing systolic pressure, but, on the other hand, the positive effect of preserving the diastolic pressure necessary for coronary perfusion.

Modeling and simulations done in Studies I and III were found to provide a useful tool for understanding cardiovascular physiology and testing hypotheses difficult to assess with clinical studies. Another important advantage of simulations is the low cost, both in economic terms and in terms of the time needed to carry out the study. Clinical evidence from, e.g. randomized clinical trials, remains the most reliable source of information when developing new treatments, but simulations and an understanding of the physical principles can be powerful tools to integrate existing knowledge and can guide future clinical studies.

The approach used in Study III for normal aging can be applied to pathological conditions or gender-specific differences in blood pressure changes, when enough data on arterial parameters and cardiac remodeling are available. Additionally, physiological and pathological changes in diastolic myocardial stiffness could be included in the model. SWE of the myocardium has the potential to be able to provide this type of information [24].

7.3 Arterial shear wave elastography

Given the impact of arterial stiffness on blood pressure and on cardiovascular health, quantitative methods for arterial stiffness measurements are of high importance. In Study IV, in-house SWE analysis software was developed and used to validate the technique for arterial application. Results show that SWE, with a suitable wave propagation analysis, was capable of accurately measuring stiffness in arterial phantoms with a 10% relative error when compared with mechanical testing. In particular, the geometry study showed that phase velocity analysis at high frequencies (>500 Hz) should be used in arterial-like geometries. Notably, group velocity analysis, which is the only analysis method currently available in commercial devices, largely underestimated the shear modulus in confined geometries such as the artery (Figure 6.6). These results are of particular relevance, as clinical studies reporting elastic modulus values in arteries based on group velocity analysis have been reported [185]. The clinical value of measuring shear wave group velocity in arteries still remains to be assessed, but results from Study IV clearly show that the elastic shear modulus was largely underestimated when using group velocity analysis. Estimating the Young's modulus requires additional assumptions such as homogeneity, isotropy and incompressibility and therefore the accuracy of the Young's moduli obtained by SWE and group velocity analysis in arteries can be questioned. Clinical scanners can be set to display group velocity values instead of elastic modulus and this would be recommended, since velocity is the physical quantity actually measured by the ultrasound scanner and could have potential clinical value despite not being able to quantify the tissue's mechanical properties. It can be noted in equation (4.4) that there is a nonlinear relation between the shear wave speed and the shear modulus. Therefore,

differences in shear modulus, and correspondingly in the Young's modulus reported by the commercial devices, are largely amplified compared with the initial speed measurements. When it is desired to quantify mechanical properties in terms of shear modulus, more accurate models are needed to relate the speed measurements to the shear modulus. Figure 6.6 shows that phase velocity analysis and a plate model could quantify the mechanical properties of arterial phantoms.

SWE was tested using phase velocity analysis and a zero-order antisymmetric plate model submerged in water, as previously suggested by Bernal et al. [16]. To the author's knowledge, an accuracy study of phase velocity analysis was missing in the literature. Therefore, a validation of the previously suggested method by comparison with mechanical testing was needed before further applying the method in *ex vivo* or *in vivo* settings. Results from this study showed good agreement between the shear modulus measured by SWE and mechanical testing, at all different pressure and phantom stiffness levels (Figure 6.**7**). The absolute error between the two techniques was 5.6 ± 4.1 kPa in the evaluated stiffness range of 40–100 kPa. Therefore, the study represents a further step toward the clinical applicability of arterial SWE.

Phase velocity analysis offered a better estimation than group velocity analysis in the confined arterial geometry. However, the use of a plate model is a simplification of the actual arterial geometry and can, as demonstrated, only be used at higher frequencies. Specifically, the experimental dispersion curve in the hollow cylinder differs from that in the plate model, mainly at low frequencies [16,17]. In the phantom setup, the two dispersion curves converged at frequencies above approximately 500 Hz, suggesting that only high frequencies should be used when assessing the accuracy of arterial SWE. This is explained by the fact that, at high frequencies, the wavelength of shear waves is smaller than the arterial wall thickness and therefore the curvature of the cylinder can be approximated to that of a plate [17]. The cutoff at 500 Hz was chosen based on experimental observations in the arterial phantoms. Ongoing work aims at assessing how phase velocity dispersion is influenced by arterial geometry and stiffness, in both phantom and simulation experiments. Experimental and simulation results show that thickness influences dispersion more than diameter does. In particular, an underestimation in wall thickness of 0.1–0.2 mm introduces an error of 4–9 kPa in the estimated shear modulus of 21–26 kPa [186]. Arterial thickness should therefore be measured in arterial SWE with an accuracy of 0.1 mm, which is the pixel size in the Aixplorer system. The influence of diameter is negligible above a certain frequency, depending on the arterial stiffness and the diameter itself. These results suggest that the use of a plate model at high frequencies is justifiable for arterial applications and that a suitable cutoff frequency should be identified for arteries *in vivo*. The choice of the cutoff frequency is a trade-off between (*i*) obtaining the large bandwidth needed to obtain repeatable results [187] and (*ii*) being able to approximate the cylindrical geometry with a plate model in the selected frequency range.

Although the SWE accuracy assessment was performed on arterial phantoms, measured shear moduli (range 40–100 kPa) are in agreement with data previously obtained in porcine carotid artery (range 24–45 kPa) [16] and in a healthy individual during diastole (80 ± 10 kPa) [17]. However, arterial stiffness varies in a wide range of elastic shear modulus values, from a few kilopascals to hundreds of kilopascals [188,189]. Additional

investigations with harder phantom material or *ex vivo* arteries should be carried out to fully assess SWE performances for arterial applications.

Other aspects such as anisotropy, viscosity and effect of surrounding tissue might cause errors in the shear modulus estimation. Concerning anisotropy, SWE has been applied in a feasibility study on equine aortic tissue under dynamic uniaxial loading with the ultrasound probe placed at different orientations [190]. The analysis was based on group velocity and the authors reported Young's modulus values significantly higher than those retrieved with mechanical testing, suggesting the need for a more adequate model for accurate modulus estimation. The comparison with the reference method could also be done by converting the modulus retrieved from mechanical testing to the corresponding shear wave speed according to (4.4) and comparing the SWE-based speed with the equivalent mechanical testing speed. Nevertheless, the study illustrated the feasibility of using SWE to detect differences in stiffness depending on arterial wall fiber orientation with respect to the ultrasound transducer. Fibers in large arteries are mostly oriented in the circumferential direction [191] and therefore imaging shear wave propagation along the cross section of the artery might be of clinical relevance. After ARF generation, shear waves travel along the circumference of the artery [192], but tracking wave propagation with a single transducer might not be sufficient since it only provides the axial velocity component [193]. Viscosity does also influence dispersion [194,195] and could provide clinically relevant information in arterial function assessments. However, the pros and cons of further complicating the wave propagation model used to derive the mechanical properties should be carefully evaluated in feasibility studies. A complex model requires many input parameters, which may vary between patients and which cannot always be measured. Adding complexity could therefore make the technique less robust and less reproducible.

One of the advantages of SWE is that it can be implemented in a standard ultrasound system and does not require a dedicated device. Reference values for changes in arterial shear modulus that are of clinical relevance have not yet been established. Such values would be useful in determining the resolution needed in arterial SWE applications to distinguish between different pathological conditions. Atherosclerotic plaque characterization is another relevant arterial SWE application, which offers many challenges because of the heterogeneity of the plaque [196].

7.4 General limitations

The methodologies used in this thesis work have some limitations. First, modeling is a simplification of reality and therefore cannot fully capture the system's behavior. In the AV-piston model, many nonlinear interactions between the system's components were neglected and all parameters were considered constant over time, despite the fact that they are known to change throughout the cardiac cycle. This was done with the aim of keeping the complexity of the model low and the parameter selection task simple. For instance, the atrial and ventricular short-axis areas were kept constant despite results from Study II showing that they vary with time. For this reason, a quantitative comparison of the model output with clinical data cannot be carried out. Figure 6.2 represents a qualitative comparison that demonstrates that the main features of the AV-plane movements were

captured by the model. The model in Study I can be seen as a framework to be further developed with other parameter choices, which could include time-varying short-axis areas. Additionally, more realistic myocardial mechanical properties should be included. Similarly, the model in Study III cannot fully capture all factors influencing blood pressure with age. These also depend on the fact that blood pressure varies, even among healthy individuals of the same age, as shown by studies reporting different normal blood pressure values [72,197]. Similarly, contradictory results can be found for cardiac output variation with age [143,198]. Despite these limitations, the model was able to capture the commonly accepted trends of blood pressure changes with age and highlighted the important contribution of the heart.

The medical imaging techniques used in this thesis work also have limitations worth mentioning. In particular, the low time resolution is one limitation of MRI that is relevant when imaging moving organs such as the heart. This resulted in the fact that the time-resolved slices analyzed in Study II were not acquired during the same heartbeat, but were averaged over different heartbeats. Cardiac chamber volumes and heart rate can vary between heartbeats, but heart rate changes are less than 25% in healthy individuals at rest [199]. The comparison between hydraulic forces and previously measured peak driving forces was a rough approximation of both. Methods for more precisely quantifying these two forces are not available with current technology and are challenging to develop because the tangible effect of the two forces is similar, i.e. they both aid LV filling.

The myocardium is constituted of blood, which is a liquid; muscle fibers, which are organized as an anisotropic solid; and a variable amount of interstitial connective tissue. This complex structure makes it challenging to define the hydraulic forces acting within the myocardium and the stress distribution generated along the muscle fibers. Therefore, including the myocardial cross section in VSA_{Epi} is a simplification of the real *in vivo* scenario. A method for including the contribution of the LV myocardium in the hydraulic force calculation still remains to be developed. Three-dimensional finite element modeling of the total heart can possibly help in clarifying this issue in the future.

The number of subjects participating in Study II (n=10) was limited, but sufficiently well-powered for a proof-of-concept. Notably, the difference between VSA and ASA was statistically significant. Larger clinical and modeling studies are needed to determine the significance of hydraulic forces in diastolic physiology and pathology.

SWE was tested on homogeneous, static, pressurized arterial phantoms, which are a simplification of real arteries. Arteries are heterogeneous, anisotropic and dynamic organs and therefore SWE application *in vivo* might be more challenging than in the experimental setup presented in Study IV. Despite this limitation, a controlled setup offers the advantage of being able to control variables that can influence the measurements. Additionally, in a laboratory environment it is possible to change significant variables one by one, such as pressure or arterial stiffness. Finally, the motion of the artery might influence SWE measurement. This is not a critical limitation since a single SWE measurement requires a few milliseconds, which is much shorter than the duration of the heart cycle (approximately 1 s). The technique is therefore capable of measuring arterial stiffness multiple times during the cardiac cycle [17,200].

8 Conclusions

The studies presented in this thesis generated new knowledge about cardiac function and developed novel methods for quantifying blood pressure changes with age and for measuring arterial stiffness. Results suggest that cardiac pumping function can to a large extent be explained by internal longitudinal movements and that hydraulic forces contribute to the displacement in the apex-to-base direction of the AV plane. Additionally, results show that both the heart and the arteries contribute to the blood pressure changes during aging and that arterial stiffness, which initiates blood pressure changes, can be accurately measured in arterial phantoms by SWE. This validation represents an important step toward clinical applicability of SWE. The specific conclusions for each of the four studies included in this thesis are summarized below.

Study I — The suggested cardiac model generated realistic pressure output and AV-piston velocity profiles. The agreement between the simulation and normal physiology supports the hypothesis that the heart functions by means of longitudinal motion of the AV plane, which can be considered as a piston unit generating reciprocal blood volume changes while keeping the total heart volume approximately constant.

Study II — The difference in short-axis area between the LV and LA demonstrates that a hydraulic force acts on the AV plane during LV diastolic filling. This force is a consequence of cardiac anatomy and assists the movement of the AV plane during diastole. A comparison of the hydraulic force with elastic restoring forces indicates that they are of the same order of magnitude. This emphasizes the importance of atrial chamber size in relation to the ventricular size in the assessment of diastolic function.

Study III — The study showed that both the arterial system and the heart contribute to systolic and diastolic blood pressure changes in normal aging (20−80 years). The increase in arterial stiffness and vascular resistance initiate the systolic pressure increase. As a consequence of this, a cardiac remodeling process starts, further augmenting the systolic pressure and mitigating the decrease in diastolic pressure.

Study IV — The study showed that SWE can accurately measure stiffness in arterial phantoms if phase velocity analysis is used, with an average relative error of 8.8 ± 6.0% when compared with mechanical testing. Moreover, group velocity and the infinite medium assumption currently implemented in clinical devices *incorrectly* estimated shear modulus values in confined geometries such as arteries. Shear modulus estimated using group velocity should therefore not be considered a quantitative measure of arterial stiffness.

9 Future work

Results from the studies presented in this thesis contribute to our understanding of cardiac pumping function and cardiovascular physiology, and suggest new methods for measuring arterial stiffness. The main findings related to hydraulic forces contributing to LV filling pave the way for further studies aimed at better characterizations of diastolic function. First, the clinical usefulness of measuring atrial and ventricular short-axis areas should be evaluated. Second, the relationship between the peak diastolic velocity and displacement of the mitral annulus to ASA and VSA could be assessed. Third, methods and models for measuring elastic restoring forces and hydraulic return could be developed. Additionally, to further assess the importance of hydraulic forces, animal studies with acute changes in atrial size, while preserving left ventricular myocardial properties and dimensions, could be performed. Reducing left atrial size during cardiac surgery is also an option that could be explored as adjunct therapy in mitral valve disease and atrial fibrillation. Finally, the existence and importance of longitudinal cardiac function should be more effectively communicated to students and to professionals who develop medical devices that interact with the cardiovascular system.

The suggested cardiovascular aging modeling could be applied to specific patient groups to identify the main driving factors generating specific blood pressure patterns. This could possibly influence the choice of drug therapies. In addition, the rule for changes in E_{ed} could be refined, taking into account more complex remodeling processes such as fibrosis. In particular, myocardial SWE might provide diastolic myocardial stiffness information. Additionally, the collection of more data on ventricular dimensions and diastolic filling pressure during normal aging would allow for a more accurate modeling of left ventricular stiffening.

Arterial SWE could be clinically applied in the near future. However, before the technique is recommended in the clinical setting, a safety study including pressure mapping during acoustic radiation force generation should be conducted. Furthermore, a critical review of the major error sources in arterial SWE should be performed to identify the factors that still need to be addressed before the technique can be reliably applied to measure arterial stiffness. Additionally, the sensitivity of SWE in detecting arterial stiffening could be assessed *in vivo* in a pilot study including healthy volunteers of different ages. In such a study, the acquisition should be ECG-triggered to keep track of the cardiac cycle phase. Systolic and diastolic blood pressure should also be measured during the SWE acquisition.

10 Other scientific contributions

Peer-reviewed articles

E. Maksuti, F. Bini, S. Fiorentini, G. Blasi, M. W. Urban, F. Marinozzi, and M. Larsson. "Influence of wall thickness and diameter on arterial shear wave elastography: a phantom and finite element study", *Physics in Medicine and Biology*. *Under review*.

E. Widman, **E. Maksuti**, C. Amador, M. W. Urban, K. Caidahl, and M. Larsson, "Shear wave elastography quantifies stiffness in ex vivo porcine artery with stiffened arterial region", *Ultrasound in Medicine & Biology*, *in press.*

E. Widman, **E. Maksuti**, D. Larsson, M. W. Urban, A. Bjällmark, and M. Larsson, "Shear wave elastography plaque characterization with mechanical testing validation: a phantom study", *Physics in Medicine & Biology*, vol. 60, p. 3151, 2015.

M. Broome, **E. Maksuti**, A. Bjällmark, B. Frenckner, and B. Janerot-Sjoberg, "Closed-loop real-time simulation model of hemodynamics and oxygen transport in the cardiovascular system", *Biomedical Engineering Online,* vol. 12, p. 69, 2013.

F. de Vico Fallani, L. Astolfi, F. Cincotti, D. Mattia, D. la Rocca, **E. Maksuti**, S. Salinari, F. Babiloni, B. Vegso, G. Kozmann, and Z. Nagy, "Evaluation of the brain network organization from EEG signals: a preliminary evidence in stroke patient", *The Anatomical Record (Hoboken)*, vol. 292, pp. 2023–31, Dec 2009.

Conference proceedings

E. Widman, **E. Maksuti**, C. Amador, M. W. Urban, K. Caidahl, and M. Larsson, "Evaluating arterial and plaque elasticity with shear wave elastography in an ex vivo porcine model", *IEEE International Ultrasonics Symposium (IUS), Taiwan*, 2015.

E. Widman, **E. Maksuti**, C. Amador, M. W. Urban, K. Caidahl, and M. Larsson, "Evaluating arterial and plaque elasticity with shear wave elastography in an ex vivo porcine model", *Ultrasonics Symposium (IUS), 2014 IEEE International, Chicago, IL, USA*, 2014.

E. Maksuti, J. Johnson, A. Bjällmark, and M. Broomé, "Physical modeling of the heart with the atrioventricular plane as a piston unit", *CMBE2013 – 3rd International Conference on Mathematical and Computational Biomedical Engineering, Hong Kong*, 2013.

M. Broomé, **E. Maksuti**, A. Waldenström, and A. Bjällmark, "Simulation of arterial hypertension and progressive arteriosclerosis with 0D multipurpose cardiovascular model", *CMBE2013 – 3rd International Conference on Mathematical and Computational Biomedical Engineering, Hong Kong*, 2013.

E. Widman, **E. Maksuti**, M. Larsson, A. Bjällmark, K. Caidahl, and J. D'hooge, "Shear wave elastography for characterization of carotid artery plaques – a feasibility study in an experimental setup", *IEEE International Ultrasonics Symposium (IUS), Dresden, Germany*, 2012.

Conference abstracts

E. Maksuti, F. Bini, S. Fiorentini, G. Blasi, M. W. Urban, F. Marinozzi, and M. Larsson, Influence of wall thickness and diameter in arterial shear wave elastography – an in vitro and in silico study. *IEEE International Ultrasonics Symposium (IUS), Tours, France*, 2016.

E. Maksuti, M. Carlsson, H. Arheden, M. Broomé, and M. Ugander, "Hydraulic forces contribute to left ventricular diastolic filling", *Journal of Cardiovascular Magnetic Resonance*, vol. 17, Suppl 1, p. 79, 2015. Presented at the *SCMR/EuroCMR joint Scientific Sessions, Nice, France*, 2015.

E. Maksuti, N. Westerhof, B. Westerhof, M. Broomé, and N. Stergiopulos, "Cardiac and arterial contribution to blood pressure changes with age", *Artery Research*, vol. 12, p. 22, 2015. Presented at *Artery 15 conference, Krakow, Poland*, 2015.

E. Maksuti, M. Carlsson, H. Arheden, M. Ugander, and M. Broomé, "Lumped-parameter modeling of cardiac longitudinal function", *Conference of the IEEE Engineering in Medicine and Biology Society, Milan, Italy*, 2015.

E. Maksuti and M. Broomé, "Simulation of right ventricular failure in patients with left ventricular assist device", *Conference of the IEEE Engineering in Medicine and Biology Society, Milan, Italy*, 2015.

E. Maksuti and M. Broomé, "Simulation of pulsatile left ventricular assist device therapy", *Medicinteknikdagarna, Uppsala, Sweden*, 2015.

E. Maksuti, D. Larsson, E. Widman, M. W. Urban, M. Larsson, and A. Bjällmark, "Influence of confined geometries in shear wave elastography – an experimental study", *Medicinteknikdagarna, Uppsala, Sweden*, 2015.

E. Widman, **E. Maksuti**, M. Larsson, A. Bjällmark, T. Nordenfur, K. Caidahl, and J. D'hooge, "Shear wave elastography of the arterial wall – where we are today", *Medicinteknikdagarna, Stockholm, Sweden*, 2013.

E. Maksuti, J. Johnson, A. Bjällmark, and M. Broomé, "The heart as a displacement pump: a novel cardiac model", *Medicinteknikdagarna, Stockholm, Sweden*, 2013.

T. Nordenfur, **E. Maksuti**, E. Widman, A. Bjällmark, and M. Larsson, "A comparison of shear wave elastography pushing sequences", *Medicinteknikdagarna, Stockholm, Sweden*, 2013.

E. Maksuti, E. Widman, M. Larsson, A. Bjällmark, A. Caidahl, and J. D'hooge, "Feasibility of shear wave elastography for carotid plaque characterization – a phantom study", presented at the *Euroecho and other Imaging Modalities, Athens, Greece*, 2012.

E. Widman, **E. Maksuti**, M. Larsson, A. Bjällmark, K. Caidahl, and J. D'hooge, "An experimental validation study for plaque characterization using shear wave elastography", presented at the *Medicinteknikdagarna, Lund, Sweden*, 2012.

11 References

1 WHO. WHO | Global atlas on cardiovascular disease prevention and control. Published Online First: 2011.http://www.who.int/cardiovascular_diseases/publications/atlas_cvd/en/ (accessed 17 Mar 2015).

2 Frank O. The basic shape of the arterial pulse. First treatise: mathematical analysis. 1899. *J Mol Cell Cardiol* 1990; 22:255–77.

3 Westerhof N, Lankhaar J-W, Westerhof BE. The arterial Windkessel. *Med Biol Eng Comput* 2009; 47:131–141.

4 Cellier FE. Continuous-System Simulation by Use of Digital Computers: A State-of-the-Art Survey and Prospectives for Development. In: *Proceedings Simulation*.; 1975. pp. 18–25.

5 Pluijmert M, Lumens J, Potse M, Delhaas T, Auricchio A, Prinzen FW. Computer Modelling for Better Diagnosis and Therapy of Patients by Cardiac Resynchronisation Therapy. *Arrhythmia Electrophysiol Rev* 2015; 4:62–7.

6 Kulhánek T, Tribula M, Kofránek J, Mateják M. Simple models of the cardiovascular system for educational and research purposes. *MEFANET J* 2014; 2:56–63.

7 Kuijpers NHL, Dassen W, van Dam PM, van Dam EM, Hermeling E, Lumensm Joost, *et al.* CircAdapt: A user-friendly learning environment for (patho) physiology of heart and circulation. In: *Computing in Cardiology*.Krakow: IEEE; 2012. pp. 969–972.

8 Shi Y, Lawford P, Hose R. Review of zero-D and 1-D models of blood flow in the cardiovascular system. *Biomed Eng Online* 2011; 10:33.

9 Lopez-Perez A, Sebastian R, Ferrero JM. Three-dimensional cardiac computational modelling: methods, features and applications. *Biomed Eng Online* 2015; 14:35.

10 Broomé M, Maksuti E, Bjällmark A, Frenckner B, Janerot-Sjöberg B. Closed-loop real-time simulation model of hemodynamics and oxygen transport in the cardiovascular system. *Biomed Eng Online* 2013; 12:69.

11 Mynard JP, Smolich JJ. One-dimensional haemodynamic modeling and wave dynamics in the entire adult circulation. *Ann Biomed Eng* 2015; 43:1443–60.

12 Chabiniok R, Wang VY, Hadjicharalambous M, Asner L, Lee J, Sermesant M, *et al.* Multiphysics and multiscale modelling, data–model fusion and integration of organ physiology in the clinic: ventricular cardiac mechanics. *Interface Focus* 2016; 6:20150083.

13 Carlsson M, Cain P, Holmqvist C, Stahlberg F, Lundbäck S, Arheden H. Total heart volume variation throughout the cardiac cycle in humans. *Am J Physiol Heart Circ Physiol* 2004; 287:H243-50.

14 Carlsson M, Ugander M, Mosén H, Buhre T, Arheden H. Atrioventricular plane

displacement is the major contributor to left ventricular pumping in healthy adults, athletes, and patients with dilated cardiomyopathy. *Am J Physiol Heart Circ Physiol* 2007; 292:H1452-9.

15 Sarvazyan AP, Urban MW, Greenleaf JF. Acoustic waves in medical imaging and diagnostics. *Ultrasound Med Biol* 2013; 39:1133–46.

16 Bernal M, Nenadic I, Urban MW, Greenleaf JF. Material property estimation for tubes and arteries using ultrasound radiation force and analysis of propagating modes. *J Acoust Soc Am* 2011; 129:1344–54.

17 Couade M, Pernot M, Prada C, Messas E, Emmerich J, Bruneval P, *et al.* Quantitative assessment of arterial wall biomechanical properties using shear wave imaging. *Ultrasound Med Biol* 2010; 36:1662–76.

18 Messas E, Pernot M, Couade M. Arterial wall elasticity: state of the art and future prospects. *Diagn Interv Imaging* 2013; 94:561–9.

19 Larsson M, Heyde B, Kremer F, Brodin L-Å, D'hooge J. Ultrasound speckle tracking for radial, longitudinal and circumferential strain estimation of the carotid artery--an in vitro validation via sonomicrometry using clinical and high-frequency ultrasound. *Ultrasonics* 2015; 56:399–408.

20 Li RX, Luo J, Balaram SK, Chaudhry FA, Shahmirzadi D, Konofagou EE. Pulse wave imaging in normal, hypertensive and aneurysmal human aortas in vivo: a feasibility study. *Phys Med Biol* 2013; 58:4549–62.

21 Teixeira R, Vieira MJ, Gonçalves A, Cardim N, Gonçalves L. Ultrasonographic vascular mechanics to assess arterial stiffness: a review. *Eur Heart J Cardiovasc Imaging* 2016; 17:233–46.

22 Couade M, Pernot M, Messas E, Bel A, Ba M, Hagege A, *et al.* In vivo quantitative mapping of myocardial stiffening and transmural anisotropy during the cardiac cycle. *IEEE Trans Med Imaging* 2011; 30:295–305.

23 Urban MW, Qiang B, Song P, Nenadic IZ, Chen S, Greenleaf JF, *et al.* Investigation of the effects of myocardial anisotropy for shear wave elastography using impulsive force and harmonic vibration. *Phys Med Biol* 2016; 61:365–382.

24 Pernot M, Lee W-N, Bel A, Mateo P, Couade M, Tanter M, *et al.* Shear Wave Imaging of Passive Diastolic Myocardial Stiffness: Stunned Versus Infarcted Myocardium. *JACC Cardiovasc Imaging* 2016; 9:1023–1030.

25 Dusuboğlu D, Polat B, Ecrengul H, Tanriverdi H, Kaftan A, Kiliç M. Assessment of systolic function by atrioventricular plane displacement in patients with diastolic dysfunction. *Acta Cardiol* 2004; 59:409–415.

26 Nammas W, El-Okda E. Atrioventricular plane displacement: does it predict in-hospital outcome after acute myocardial infarction? *Eur Rev Med Pharmacol Sci* 2012; 16 Suppl 1:16–21.

27 Remme EW, Opdahl A, Smiseth OA. Mechanics of left ventricular relaxation, early diastolic lengthening, and suction investigated in a mathematical model. *Am J Physiol Heart Circ Physiol* 2011; 300:H1678-87.

28 Opdahl A, Remme EW, Helle-Valle T, Lyseggen E, Vartdal T, Pettersen E, *et al.*

Determinants of left ventricular early-diastolic lengthening velocity: independent contributions from left ventricular relaxation, restoring forces, and lengthening load. *Circulation* 2009; 119:2578–86.

29 Chung CS, Shmuylovich L, Kovács SJ. What global diastolic function is, what it is not, and how to measure it. *Am J Physiol Heart Circ Physiol* 2015; 309:H1392-406.

30 Granzier HL, Irving TC. Passive tension in cardiac muscle: contribution of collagen, titin, microtubules, and intermediate filaments. *Biophys J* 1995; 68:1027–1044.

31 Helmes M, Trombitás K, Granzier H. Titin develops restoring force in rat cardiac myocytes. *Circ Res* 1996; 79:619–26.

32 Opitz CA, Kulke M, Leake MC, Neagoe C, Hinssen H, Hajjar RJ, *et al.* Damped elastic recoil of the titin spring in myofibrils of human myocardium. *Proc Natl Acad Sci U S A* 2003; 100:12688–93.

33 Lundbäck S. Cardiac pumping and function of the ventricular septum. *Acta Physiol Scand Suppl* 1986; 550:1–101. Available online at: http://www.grippingheart.com/pdf/thesis.pdf (accessed 27 Oct 2016)

34 Lunkenheimer A, Lunkenheimer PP. Zum Bewegungsablauf Des Herzens. Herz Kreislauf. 1983; 15:416–424.

35 Lunkenheimer PP. The hydraulic function of intramyocardial fluids subject to the erectile properties of the ventricular wall of mammalian hearts. *Zentralblatt für Veterinärmedizin R A* 1975; 22:632–644.

36 O'Rourke MF. Arterial aging: pathophysiological principles. *Vasc Med* 2007; 12:329–341.

37 Slotwiner DJ, Devereux RB, Schwartz JE, Pickering TG, de Simone G, Ganau A, *et al.* Relation of age to left ventricular function in clinically normal adults. *Am J Cardiol* 1998; 82:621–6.

38 Ganau A, Saba PS, Roman MJ, de Simone G, Realdi G, Devereux RB. Ageing induces left ventricular concentric remodelling in normotensive subjects. *J Hypertens* 1995; 13:1818–22.

39 Ioannou C V., Morel DR, Katsamouris AN, Katranitsa S, Startchik I, Kalangos A, *et al.* Left ventricular hypertrophy induced by reduced aortic compliance. *J Vasc Res* 2009; 46:417–425.

40 Laurent S. Arterial stiffness in arterial hypertension. *Curr Hypertens Rep* 2006; 8:179–80.

41 Vlachopoulos C, Aznaouridis K, Stefanadis C. Prediction of cardiovascular events and all-cause mortality with arterial stiffness: a systematic review and meta-analysis. *J Am Coll Cardiol* 2010; 55:1318–27.

42 Liao J, Farmer J. Arterial stiffness as a risk factor for coronary artery disease. *Curr Atheroscler Rep* 2014; 16:387.

43 Molina DK, DiMaio VJM. Normal Organ Weights in Women: Part I-The Heart. *Am J Forensic Med Pathol* 2015; 36:176–81.

44 Molina DK, DiMaio VJM. Normal organ weights in men: part I-the heart. *Am J Forensic Med Pathol* 2012; 33:362–7.

45 Carlsson M. *Aspects on Cardiac Pumping. PhD thesis, Lund, Sweden.* 2007.

46 Watkins MW, LeWinter MM. Physiologic role of the normal pericardium. *Annu Rev Med* 1993; 44:171–80.

47 Baker AE, Dani R, Smith ER, Tyberg J V, Belenkie I. Quantitative assessment of independent contributions of pericardium and septum to direct ventricular interaction. *Am J Physiol* 1998; 275:H476-83.

48 Torrent-Guasp F. Systolic ventricular filling. *Eur J Cardio-Thoracic Surg* 2004; 25:376–386.

49 Ritman EL. Commentaries on viewpoint: is left ventricular volume during diastasis the real equilibrium volume, and what is its relationship to diastolic suction? *J Appl Physiol* 2008; 105:1015–6; author reply 1019.

50 Robinson TF, Factor SM, Sonnenblick EH. The heart as a suction pump. *Sci Am* 1986; 254:84–91.

51 Zhang W, Chung CS, Shmuylovich L, Kovács SJ. Is left ventricular volume during diastasis the real equilibrium volume, and what is its relationship to diastolic suction? *J Appl Physiol* 2008; 105:1012–4.

52 Rushmer RF. Initial ventricular impulse. A potential key to cardiac evaluation. *Circulation* 1964; 29:268–83.

53 Hoffman EA, Ritman EL. Invariant total heart volume in the intact thorax. *Am J Physiol* 1985; 249:H883-90.

54 Steding-Ehrenborg K, Carlsson M, Stephensen S, Arheden H. Atrial aspiration from pulmonary and caval veins is caused by ventricular contraction and secures 70% of the total stroke volume independent of resting heart rate and heart size. *Clin Physiol Funct Imaging* 2013; 33:233–40.

55 Smiseth OA, Frais MA, Kingma I, Smith ER, Tyberg J V. Assessment of pericardial constraint in dogs. *Circulation* 1985; 71:158–64.

56 Fabiato A. Calcium-induced release of calcium from the cardiac sarcoplasmic reticulum. *Am J Physiol* 1983; 245:C1-14.

57 Guyton A, Hall J. *Textbook of medical physiology*. 12th ed. Saunders Elsevier; 2011.

58 Jöbsis PD, Ashikaga H, Wen H, Rothstein EC, Horvath KA, McVeigh ER, *et al.* The visceral pericardium: macromolecular structure and contribution to passive mechanical properties of the left ventricle. *Am J Physiol Heart Circ Physiol* 2007; 293:H3379-87.

59 Lee JM, Boughner DR. Mechanical properties of human pericardium. Differences in viscoelastic response when compared with canine pericardium. *Circ Res* 1985; 57:475–81.

60 Krams R, Janssen M, Van der Lee C, Van Meegen J, De Jong JW, Slager CJ, *et al.* Loss of elastic recoil in postischemic myocardium induces rightward shift of the

systolic pressure-volume relationship. *Am J Physiol Hear Circ Physiol* 1994; 267:H1557-1564.

61 The Lancet. Editorial: Starling's law survives. *Lancet* 1974; 304:818.

62 Maestrini D. [The law of the heart from its discovery to the present time]. *Minerva Med* 1958; 49:Varia, 28-36.

63 Liska J, Lundbäck S, Semb BK. In vitro flow characteristics of a new pump with a high inherent sensitivity to venous return. *ASAIO Trans* 1991; 37:592–7.

64 Stergiopulos N, Westerhof N. Role of total arterial compliance and peripheral resistance in the determination of systolic and diastolic aortic pressure. *Pathol Biol (Paris)* 1999; 47:641–7.

65 Ioannou C V., Stergiopulos N, Katsamouris AN, Startchik I, Kalangos A, Licker MJ, *et al.* Hemodynamics induced after acute reduction of proximal thoracic aorta compliance. *Eur J Vasc Endovasc Surg* 2003; 26:195–204.

66 Westerhof N, Stergiopulos N, Noble MIM. Resistance. In: *Snapshots of Hemodynamics*.Boston, MA: Springer US; 2010. pp. 31–36.

67 Chirinos JA, Segers P, Gillebert TC, Gupta AK, De Buyzere ML, De Bacquer D, *et al.* Arterial properties as determinants of time-varying myocardial stress in humans. *Hypertension* 2012; 60:64–70.

68 Stergiopulos N, Meister JJ, Westerhof N. Determinants of stroke volume and systolic and diastolic aortic pressure. *Am J Physiol* 1996; 270:H2050-9.

69 Burkhoff D, Mirsky I, Suga H. Assessment of systolic and diastolic ventricular properties via pressure-volume analysis: a guide for clinical, translational, and basic researchers. *Am J Physiol Heart Circ Physiol* 2005; 289:H501-12.

70 Westerhof N, Stergiopulos N, Noble MIM. Cardiac Power and Ventriculo-Arterial Coupling. In: *Snapshots of Hemodynamics*.Boston, MA: Springer US; 2010. pp. 107–114.

71 Redfield MM, Jacobsen SJ, Borlaug BA, Rodeheffer RJ, Kass DA. Age- and gender-related ventricular-vascular stiffening: a community-based study. *Circulation* 2005; 112:2254–62.

72 Franklin SS, Gustin W, Wong ND, Larson MG, Weber MA, Kannel WB, *et al.* Hemodynamic Patterns of Age-Related Changes in Blood Pressure : The Framingham Heart Study. *Circulation* 1997; 96:308–315.

73 Palatini P, Casiglia E, Gąsowski J, Głuszek J, Jankowski P, Narkiewicz K, *et al.* Arterial stiffness, central hemodynamics, and cardiovascular risk in hypertension. *Vasc Health Risk Manag* 2011; 7:725–39.

74 Karnopp D, Margolis DL, Rosenberg RC. *System dynamics modeling, simulation, and control of mechatronic systems*. 4th ed. Wiley; 2006.

75 Reymond P, Merenda F, Perren F, Rüfenacht D, Stergiopulos N. Validation of a one-dimensional model of the systemic arterial tree. *Am J Physiol Heart Circ Physiol* 2009; 297:H208-22.

76 Prahl Wittberg L, van Wyk S, Fuchs L, Gutmark E, Backeljauw P, Gutmark-Little I. Effects of aortic irregularities on blood flow. *Biomech Model Mechanobiol* 2016; 15:345–60.

77 Cheng Y, Oertel H, Schenkel T. Fluid-Structure Coupled CFD Simulation of the Left Ventricular Flow During Filling Phase. *Ann Biomed Eng* 2005; 33:567–576.

78 Fritz T, Wieners C, Seemann G, Steen H, Dössel O. Simulation of the contraction of the ventricles in a human heart model including atria and pericardium : Finite element analysis of a frictionless contact problem. *Biomech Model Mechanobiol* 2014, 13(3):627-41.

79 Suga H, Sagawa K, Shoukas AA. Load independence of the instantaneous pressure-volume ratio of the canine left ventricle and effects of epinephrine and heart rate on the ratio. *Circ Res* 1973; 32:314–22.

80 Stergiopulos N, Westerhof BE, Westerhof N. Total arterial inertance as the fourth element of the windkessel model. *Am J Physiol* 1999; 276:H81-8.

81 Maksuti E, Bjällmark A, Broomé M. Modelling the heart with the atrioventricular plane as a piston unit. *Med Eng Phys* 2015; 37:87–92.

82 Senzaki H, Chen CH, Kass DA. Single-beat estimation of end-systolic pressure-volume relation in humans. A new method with the potential for noninvasive application. *Circulation* 1996; 94:2497–506.

83 Mynard JP, Davidson MR, Penny DJ, Smolich JJ. A simple, versatile valve model for use in lumped parameter and one-dimensional cardiovascular models. *Int j numer method biomed eng*; 28:626–41.

84 Paynter HM, Briggs P. *Analysis and design of engineering systems: class notes from M.I.T. course 2.751*. Cambridge, MA: M.I.T. Press; 1961.

85 Cellier FE. *Continuous System Modeling*. Springer; 1991. http://www.springer.com/us/book/9780387975023 (accessed 9 Mar2016).

86 Zimmer D, Cellier F. The Modelica multi-bond graph library. *Proc 5th Int Model Conf* Published Online First: 2006.http://mathpros.com/papers/bond_graph/Multi-bond_Graph_Library.pdf (accessed 11 Apr 2014).

87 Petzold L. Description of DASSL: A differential/algebraic system solver. *No SAND-82-8637; CONF-820810-21 Sandia Natl Labs, Livermore, CA* Published Online First: 1982.http://www.osti.gov/scitech/biblio/5882821 (accessed 11 Apr 2014).

88 Scatliff JH, Morris PJ. From Roentgen to magnetic resonance imaging: the history of medical imaging. *N C Med J* 2014; 75:111–3.

89 Sivaraman A. High intensity focused ultrasound for Focal Therapy of prostate cancer. *Arch Esp Urol* 2016; 69:311–316.

90 Foundation for Research on Information Technologies in Society (IT'IS). http://www.itis.ethz.ch/virtual-population/tissue-properties/database/acoustic-properties/speed-of-sound/ (accessed 14 Sep 2016).

91 Raynor BD. Routine ultrasound in pregnancy. *Clin Obstet Gynecol* 2003; 46:882–9.

92 Thomas JD, Popović ZB. Assessment of Left Ventricular Function by Cardiac Ultrasound. *J Am Coll Cardiol* 2006; 48:2012–2025.

93 Bruker. BioSpec series. https://www.bruker.com/products/mr/preclinical-mri/biospec/overview.html (accessed 17 Oct 2016).

94 Lacroix L-M, Delpech F, Nayral C, Lachaize S, Chaudret B. New generation of magnetic and luminescent nanoparticles for in vivo real-time imaging. *Interface Focus* 2013; 3:20120103.

95 Lanzer P, Barta C, Botvinick EH, Wiesendanger HU, Modin G, Higgins CB. ECG-synchronized cardiac MR imaging: method and evaluation. *Radiology* 1985; 155:681–6.

96 Nagueh SF, Smiseth OA, Appleton CP, Byrd BF, Dokainish H, Edvardsen T, *et al.* Recommendations for the Evaluation of Left Ventricular Diastolic Function by Echocardiography: An Update from the American Society of Echocardiography and the European Association of Cardiovascular Imaging. *J Am Soc Echocardiogr* 2016; 29:277–314.

97 Baumgartner H, Hung J, Bermejo J, Chambers JB, Evangelista A, Griffin BP, *et al.* Echocardiographic assessment of valve stenosis: EAE/ASE recommendations for clinical practice. *Eur J Echocardiogr* 2009; 10:1–25.

98 Captur G, Manisty C, Moon JC. Cardiac MRI evaluation of myocardial disease. *Heart* Published Online First: 27 June 2016. doi:10.1136/heartjnl-2015-309077

99 Banka P, Geva T. Advances in pediatric cardiac MRI. *Curr Opin Pediatr* Published 2016.

100 Kadkhodayan A, Chareonthaitawee P, Raman S V., Cooper LT. Imaging of Inflammation in Unexplained Cardiomyopathy. *JACC Cardiovasc Imaging* 2016; 9:603–617.

101 Mewton N, Liu CY, Croisille P, Bluemke D, Lima JAC. Assessment of myocardial fibrosis with cardiovascular magnetic resonance. *J Am Coll Cardiol* 2011; 57:891–903.

102 Cikes M, Solomon SD. Beyond ejection fraction: an integrative approach for assessment of cardiac structure and function in heart failure. *Eur Heart J* 2016; 37:1642–50.

103 Udelson JE. Heart failure with preserved ejection fraction. *Circulation* 2011; 124:e540-3.

104 Smiseth OA, Torp H, Opdahl A, Haugaa KH, Urheim S. Myocardial strain imaging: how useful is it in clinical decision making? *Eur Heart J* 2016; 37:1196–207.

105 Berg J, Lindgren P, Kahan T, Schill O, Persson H, Edner M, *et al.* Health-related quality of life and long-term morbidity and mortality in patients hospitalised with systolic heart failure. *JRSM Cardiovasc Dis* 2014; 3:2048004014548735.

106 Steding-Ehrenborg K, Boushel RC, Calbet JA, Åkeson P, Mortensen SP. Left ventricular atrioventricular plane displacement is preserved with lifelong endurance training and is the main determinant of maximal cardiac output. *J Physiol* 2015; 593:5157–66.

107 Jacques DC, Pinsky MR, Severyn D, Gorcsan J. Influence of alterations in loading on mitral annular velocity by tissue doppler echocardiography and its associated ability to predict filling pressures. *Chest* 2004; 126:1910–1918.

108 Oğuzhan A, Arinç H, Abaci A, Topsakal R, Eryol NK, Özdoğru I, *et al.* Preload dependence of Doppler tissue imaging derived indexes of left ventricular diastolic function. *Echocardiography* 2005; 22:320–325.

109 Garcia MJ, Smedira NG, Greenberg NL, Main M, Firstenberg MS, Odabashian J, *et al.* Color M-mode Doppler flow propagation velocity is a preload insensitive index of left ventricular relaxation: Animal and human validation. *J Am Coll Cardiol* 2000; 35:201–208.

110 Pelà G, Regolisti G, Coghi P, Cabassi A, Basile A, Cavatorta A, *et al.* Effects of the reduction of preload on left and right ventricular myocardial velocities analyzed by Doppler tissue echocardiography in healthy subjects. *Eur J Echocardiogr* 2004; 5:262–71.

111 Arvidsson PM, Kovács SJ, Töger J, Borgquist R, Heiberg E, Carlsson M, *et al.* Vortex ring behavior provides the epigenetic blueprint for the human heart. *Sci Rep* 2016; 6:22021.

112 Bauman L, Chung CS, Karamanoglu M, Kovács SJ. The peak atrioventricular pressure gradient to transmitral flow relation: Kinematic model prediction with in vivo validation. *J Am Soc Echocardiogr* 2004; 17:839–844.

113 Banerjee A, Fowkes FG, Rothwell PM. Associations Between Peripheral Artery Disease and Ischemic Stroke: Implications for Primary and Secondary Prevention. *Stroke* 2010; 41:2102–2107.

114 Hamilton PK, Lockhart CJ, Quinn CE, McVeigh GE. Arterial stiffness: clinical relevance, measurement and treatment. *Clin Sci (Lond)* 2007; 113:157–170.

115 Nichols W, O'Rourke M, Vlachopoulos C. *McDonald's Blood Flow in Arteries: Theoretical, Experimental and Clinical Principles*. CRC Press; 2011, page 55.

116 Scuteri A, Morrell CH, Orrù M, Strait JB, Tarasov K V, Ferreli LAP, *et al.* Longitudinal perspective on the conundrum of central arterial stiffness, blood pressure, and aging. *Hypertension* 2014; 64:1219–27.

117 Davies JM, Bailey MA, Griffin KJ, Scott DJA. Pulse wave velocity and the non-invasive methods used to assess it: Complior, SphygmoCor, Arteriograph and Vicorder. *Vascular* 2012; 20:342–9.

118 Huybrechts SAM, Devos DG, Vermeersch SJ, Mahieu D, Achten E, de Backer TLM, *et al.* Carotid to femoral pulse wave velocity: a comparison of real travelled aortic path lengths determined by MRI and superficial measurements. *J Hypertens* 2011; 29:1577–82.

119 Laurent S, Marais L, Boutouyrie P. The Noninvasive Assessment of Vascular Aging. *Can J Cardiol* 2016; 32:669–79.

120 Kawasaki T, Sasayama S, Yagi S, Asakawa T, Hirai T. Non-invasive assessment of the age related changes in stiffness of major branches of the human arteries. *Cardiovasc Res* 1987; 21:678–87.

121 Hoeks AP, Brands PJ, Smeets FA, Reneman RS. Assessment of the distensibility of superficial arteries. *Ultrasound Med Biol* 1990; 16:121–8.

122 Brands PJ, Willigers JM, Ledoux LAF, Reneman RS, Hoeks APG. A noninvasive method to estimate pulse wave velocity in arteries locally by means of ultrasound. *Ultrasound Med Biol* 1998; 24:1325–1335.

123 Ribbers H, Lopata RGP, Holewijn S, Pasterkamp G, Blankensteijn JD, de Korte CL. Noninvasive two-dimensional strain imaging of arteries: validation in phantoms and preliminary experience in carotid arteries in vivo. *Ultrasound Med Biol* 2007; 33:530–40.

124 Lim TK, Lim E, Dwivedi G, Kooner J, Senior R. Normal value of carotid intima-media thickness--a surrogate marker of atherosclerosis: quantitative assessment by B-mode carotid ultrasound. *J Am Soc Echocardiogr* 2008; 21:112–6.

125 Krejza J, Arkuszewski M, Kasner SE, Weigele J, Ustymowicz A, Hurst RW, *et al.* Carotid artery diameter in men and women and the relation to body and neck size. *Stroke* 2006; 37:1103–5.

126 Sarvazyan AP, Rudenko O V, Swanson SD, Fowlkes JB, Emelianov SY. Shear wave elasticity imaging: a new ultrasonic technology of medical diagnostics. *Ultrasound Med Biol* 1998; 24:1419–35.

127 Bercoff J, Tanter M, Fink M. Supersonic shear imaging: a new technique for soft tissue elasticity mapping. *IEEE Trans Ultrason Ferroelectr Freq Control* 2004; 51:396–409.

128 Tanter M, Fink M. Ultrafast imaging in biomedical ultrasound. *IEEE Trans Ultrason Ferroelectr Freq Control* 2014; 61:102–19.

129 Ramnarine K V, Garrard JW, Dexter K, Nduwayo S, Panerai RB, Robinson TG. Shear wave elastography assessment of carotid plaque stiffness: in vitro reproducibility study. *Ultrasound Med Biol* 2014; 40:200–9.

130 Garrard JW, Ramnarine K. Shear-wave elastography in carotid plaques: comparison with grayscale median and histological assessment in an interesting case. *Ultraschall Med* 2014; 35:1–3.

131 Kwak JY, Kim E-K. Ultrasound elastography for thyroid nodules: recent advances. *Ultrasonography* 2014; 33:75–82.

132 Song P, Bi X, Mellema DC, Manduca A, Urban MW, Greenleaf JF, *et al.* Quantitative Assessment of Left Ventricular Diastolic Stiffness Using Cardiac Shear Wave Elastography: A Pilot Study. *J Ultrasound Med* 2016; 35:1419–27.

133 Lamb H. On Waves in an Elastic Plate. *Proc R Soc A Math Phys Eng Sci* 1917; 93:114–128.

134 Gazis DC. Three-Dimensional Investigation of the Propagation of Waves in Hollow Circular Cylinders. I. Analytical Foundation. *J Acoust Soc Am* 1959; 31:568.

135 Gazis DC. Three-Dimensional Investigation of the Propagation of Waves in Hollow Circular Cylinders. II. Numerical Results. *J Acoust Soc Am* 1959; 31:573.

136 Beyar R, Hausknecht MJ, Halperin HR, Yin FC, Weisfeldt ML. Interaction between

cardiac chambers and thoracic pressure in intact circulation. *Am J Physiol* 1987; 253:H1240-52.

137 Mynard JP, Davidson MR, Penny DJ, Smolich JJ. A simple, versatile valve model for use in lumped parameter and one-dimensional cardiovascular models. *Int j numer method biomed eng* 2012; 28:626–641.

138 Cellier F, Nebot A. Object-oriented Modeling in the Service of Medicine. *Proc 6th Asia Simul Conf* Published Online First: 2005. http://people.inf.ethz.ch/fcellier/Pubs/BG/ICSC_05.pdf (accessed 11 Apr 2014).

139 Milnor WR. *Hemodynamics*. Williams & Wilkins; 1989. https://books.google.com/books?id=wA5vQgAACAAJ&pgis=1 (accessed 4 Apr 2016).

140 Segers P, Rietzschel ER, De Buyzere ML, Stergiopulos N, Westerhof N, Van Bortel LM, *et al.* Three- and four-element Windkessel models: assessment of their fitting performance in a large cohort of healthy middle-aged individuals. *Proc Inst Mech Eng H* 2008; 222:417–28.

141 Boutouyrie P, Vermeersch SJ. Determinants of pulse wave velocity in healthy people and in the presence of cardiovascular risk factors: Establishing normal and reference values. *Eur Heart J* 2010; 31:2338–2350.

142 Segers P, Rietzschel ER, De Buyzere ML, Vermeersch SJ, De Bacquer D, Van Bortel LM, *et al.* Noninvasive (input) impedance, pulse wave velocity, and wave reflection in healthy middle-aged men and women. *Hypertension* 2007; 49:1248–55.

143 Lakatta EG. Changes in cardiovascular function with aging. *Eur Heart J* 1990; 11 Suppl C:22–9.

144 Grossman W, Jones D, McLaurin LP. Wall stress and patterns of hypertrophy in the human left ventricle. *J Clin Invest* 1975; 56:56–64.

145 Segers P, Stergiopulos N, Schreuder JJ, Westerhof BE, Westerhof N. Left ventricular wall stress normalization in chronic pressure-overloaded heart: a mathematical model study. *Am J Physiol Hear Circ Physiol* 2000; 279:H1120-1127.

146 Cole RT, Lucas CL, Cascio WE, Johnson TA. A LabVIEW model incorporating an open-loop arterial impedance and a closed-loop circulatory system. *Ann Biomed Eng* 2005; 33:1555–73.

147 Segers P, Stergiopulos N, Westerhof N. Quantification of the contribution of cardiac and arterial remodeling to hypertension. *Hypertension* 2000; 36:760–5.

148 Vardoulis O, Papaioannou TG, Stergiopulos N. On the estimation of total arterial compliance from aortic pulse wave velocity. *Ann Biomed Eng* 2012; 40:2619–26.

149 Avolio AP, Van Bortel LM, Boutouyrie P, Cockcroft JR, McEniery CM, Protogerou AD, *et al.* Role of pulse pressure amplification in arterial hypertension: Experts' opinion and review of the data. Hypertension. 2009; 54:375–383.

150 Bouchard RJ, Gault JH, Ross J. Evaluation of Pulmonary Arterial End-Diastolic Pressure as an Estimate of Left Ventricular End-Diastolic Pressure in Patients with Normal and Abnormal Left Ventricular Performance. *Circulation* 1971; 44:1072–1079.

151 Shmuylovich L, Kovács SJ. Load-independent index of diastolic filling: model-based derivation with in vivo validation in control and diastolic dysfunction subjects. *J Appl Physiol* 2006; 101:92–101.

152 Maceira AM, Prasad SK, Khan M, Pennell DJ. Normalized left ventricular systolic and diastolic function by steady state free precession cardiovascular magnetic resonance. *J Cardiovasc Magn Reson* 2006; 8:417–426.

153 National Instruments. What is I/Q data? White Pap. 2016. http://www.ni.com/tutorial/4805/en/ (accessed 15 Oct 2016).

154 Loupas T, Powers JT, Gill RW. An axial velocity estimator for ultrasound blood flow imaging, based on a full evaluation of the Doppler equation by means of a two-dimensional autocorrelation approach. *IEEE Trans Ultrason Ferroelectr Freq Control* 1995; 42:672–688.

155 Song P, Zhao H, Urban M, Manduca A, Pislaru S, Kinnick R, *et al.* Improved Shear Wave Motion Detection Using Pulse-Inversion Harmonic Imaging with a Phased Array Transducer. *IEEE Trans Med Imaging* 2013; 32:2299–2310.

156 Maksuti E, Widman E, Larsson D, Urban MW, Larsson M, Bjällmark A. Arterial Stiffness Estimation by Shear Wave Elastography: Validation in Phantoms with Mechanical Testing. *Ultrasound Med Biol* 2016; 42:308–21.

157 Larsson D. Accuracy Assessment of Shear Wave Elastography for Arterial Applications by Mechanical Testing. *Master thesis, KTH, Stockholm, Sweden*. 2014.

158 Biesiadecki BJ, Davis JP, Ziolo MT, Janssen PML. Tri-modal regulation of cardiac muscle relaxation; intracellular calcium decline, thin filament deactivation, and cross-bridge cycling kinetics. *Biophys Rev* 2014; 6:273–289.

159 Arutunyan AH. Atrioventricular plane displacement is the sole mechanism of atrial and ventricular refill. *Am J Physiol Heart Circ Physiol* 2015; 308:H1317-20.

160 Arvidsson PM, Carlsson M, Kovács SJ, Arheden H. Letter to the Editor: Atrioventricular plane displacement is not the sole mechanism of atrial and ventricular refill. *Am J Physiol Heart Circ Physiol* 2015; 309:H1094-6.

161 Arutunyan AH. Reply to “Letter to the Editor: Atrioventricular plane displacement is not the sole mechanism of atrial and ventricular refill”. *Am J Physiol Heart Circ Physiol* 2015; 309:H1097-9.

162 Quinn U, Tomlinson L a, Cockcroft JR. Arterial stiffness. *JRSM Cardiovasc Dis* 2012; 1:1–8.

163 Davies JM, Bailey MA, Griffin KJ, Scott DJA. Pulse wave velocity and the non-invasive methods used to assess it: Complior, SphygmoCor, Arteriograph and Vicorder. *Vascular* 2012; 20:342–9.

164 Korakianitis T, Shi Y. Effects of atrial contraction, atrioventricular interaction and heart valve dynamics on human cardiovascular system response. *Med Eng Phys* 2006; 28:762–79.

165 Lisauskas J, Singh J, Courtois M, Kovács SJ. The relation of the peak Doppler E-wave to peak mitral annulus velocity ratio to diastolic function. *Ultrasound Med Biol* 2001; 27:499–507.

166 Fritz T, Wieners C, Seemann G, Steen H, Dössel O. Simulation of the contraction of the ventricles in a human heart model including atria and pericardium. *Biomech Model Mechanobiol* 2014; 13:627–41.

167 Arts T, Delhaas T, Bovendeerd P, Verbeek X, Prinzen FW. Adaptation to mechanical load determines shape and properties of heart and circulation: the CircAdapt model. *Am J Physiol Heart Circ Physiol* 2005; 288:H1943-54.

168 Dongaonkar RM, Stewart RH, Geissler HJ, Laine GA. Myocardial microvascular permeability, interstitial oedema, and compromised cardiac function. *Cardiovasc Res* 2010; 87:331–9.

169 Courtois M, Kovács SJ, Ludbrook PA. Transmitral pressure-flow velocity relation. Importance of regional pressure gradients in the left ventricle during diastole. *Circulation* 1988; 78:661–71.

170 Rossi A, Temporelli PL, Quintana M, Dini FL, Ghio S, Hillis GS, *et al.* Independent relationship of left atrial size and mortality in patients with heart failure: an individual patient meta-analysis of longitudinal data (MeRGE Heart Failure). *Eur J Heart Fail* 2009; 11:929–36.

171 Blume GG, Mcleod CJ, Barnes ME, Seward JB, Pellikka PA, Bastiansen PM, *et al.* Left atrial function: physiology, assessment, and clinical implications. *Eur J Echocardiogr* 2011; 12:421–30.

172 Schievano S, Taylor AM, Capelli C, Lurz P, Nordmeyer J, Migliavacca F, *et al.* Patient specific finite element analysis results in more accurate prediction of stent fractures: application to percutaneous pulmonary valve implantation. *J Biomech* 2010; 43:687–93.

173 Hunter PJ, Pullan AJ, Smaill BH. Modeling total heart function. *Annu Rev Biomed Eng* 2003; 5:147–177.

174 Nordsletten DA, Niederer SA, Nash MP, Hunter PJ, Smith NP. Coupling multi-physics models to cardiac mechanics. *Prog Biophys Mol Biol* 2011; 104:77–88.

175 Katz AM. *Physiology of the Heart*. 5th edition. Philadelphia: Lippincott Williams & Wilkins; 2011.

176 Matos J, Kronzon I, Panagopoulos G, Perk G. Mitral annular plane systolic excursion as a surrogate for left ventricular ejection fraction. *J Am Soc Echocardiogr* 2012; 25:969–74.

177 Portnoy SG al, Rudski LG. Echocardiographic evaluation of the right ventricle: a 2014 perspective. Curr. Cardiol. Rep. 2015; 17:21.

178 Claessens TE, Rietzschel ER, De Buyzere ML, De Bacquer D, De Backer G, Gillebert TC, *et al.* Noninvasive assessment of left ventricular and myocardial contractility in middle-aged men and women: disparate evolution above the age of 50? *Am J Physiol Heart Circ Physiol* 2007; 292:H856-65.

179 Forsberg LM, Tamás É, Vánky F, Engvall J, Nylander E. Differences in recovery of left and right ventricular function following aortic valve interventions: a longitudinal echocardiographic study in patients undergoing surgical, transapical or transfemoral aortic valve implantation. *Catheter Cardiovasc Interv* 2013; 82:1004–14.

180 Reynolds HR, Tunick PA, Grossi EA, Dilmanian H, Colvin SB, Kronzon I. Paradoxical septal motion after cardiac surgery: a review of 3,292 cases. *Clin Cardiol* 2007; 30:621–3.

181 Wranne B, Pinto FJ, Hammarström E, St Goar FG, Puryear J, Popp RL. Abnormal right heart filling after cardiac surgery: time course and mechanisms. *Br Heart J* 1991; 66:435–42.

182 Nordmeyer J, Khambadkone S, Coats L, Schievano S, Lurz P, Parenzan G, *et al.* Risk stratification, systematic classification, and anticipatory management strategies for stent fracture after percutaneous pulmonary valve implantation. *Circulation* 2007; 115:1392–7.

183 Wagenseil JE, Mecham RP. Elastin in large artery stiffness and hypertension. *J Cardiovasc Transl Res* 2012; 5:264–73.

184 Mitchell GF. Effects of central arterial aging on the structure and function of the peripheral vasculature: implications for end-organ damage. *J Appl Physiol* 2008; 105:1652–1660.

185 Li Z, Du L, Wang F, Luo X. Assessment of the arterial stiffness in patients with acute ischemic stroke using longitudinal elasticity modulus measurements obtained with Shear Wave Elastography. *Med Ultrason* 2016; 18:182–9.

186 Maksuti E, Bini F, Fiorentini S, Blasi G, Urban MW, Marinozzi F, *et al.* Influence of wall thickness and diameter on arterial shear wave elastography: a phantom and finite element study. (*Under review on 05 Nov 2016)*

187 Widman E, Maksuti E, Amador C, Urban MW, Caidahl K, Larsson M. Shear Wave Elastography Quantifies Stiffness in Ex Vivo Porcine Artery with Stiffened Arterial Region. *Ultrasound Med Biol* 2016; 42:2423–35.

188 Deng SX, Tomioka J, Debes JC, Fung YC. New experiments on shear modulus of elasticity of arteries. *Am J Physiol - Hear Circ Physiol* 1994; 266.

189 Kamenskiy A V, Dzenis YA, Kazmi SAJ, Pemberton MA, Pipinos II, Phillips NY, *et al.* Biaxial mechanical properties of the human thoracic and abdominal aorta, common carotid, subclavian, renal and common iliac arteries. *Biomech Model Mechanobiol* 2014; 13:1341–59.

190 Shcherbakova DA, Papadacci C, Swillens A, Caenen A, De Bock S, Saey V, *et al.* Supersonic shear wave imaging to assess arterial nonlinear behavior and anisotropy: proof of principle via ex vivo testing of the horse aorta. *Adv Mech Eng* 2014; 6:1–12.

191 Azinfar L, Ravanfar M, Wang Y, Zhang K, Duan D, Yao G. High resolution imaging of the fibrous microstructure in bovine common carotid artery using optical polarization tractography. *J Biophotonics* Published Online First: 11 December 2015. doi:10.1002/jbio.201500229.

192 Urban MW, Nenadic IZ, Pislaru C, Greenleaf JF. Measurement of longitudinal and circumferential waves in tubes and artery excited with ultrasound radiation force. In: *2013 IEEE International Ultrasonics Symposium (IUS)*.IEEE; 2013. pp. 1765–1768.

193 Hansen HHG, Pernot M, Chatelin S, Tanter M, de Korte CL. Shear wave elastography for lipid content detection in transverse arterial cross-sections. In:

2015 IEEE International Ultrasonics Symposium (IUS).IEEE; 2015. pp. 1–4.

194 Chen S, Fatemi M, Greenleaf JF. Quantifying elasticity and viscosity from measurement of shear wave speed dispersion. *J Acoust Soc Am* 2004; 115:2781.

195 Amador C, Urban MW, Chen S, Chen Q, An K-N, Greenleaf JF. Shear elastic modulus estimation from indentation and SDUV on gelatin phantoms. *IEEE Trans Biomed Eng* 2011; 58:1706–14.

196 De Korte CL, Fekkes S, Nederveen AJ, Manniesing R, Hansen HHG. Review: Mechanical Characterization of Carotid Arteries and Atherosclerotic Plaques. *IEEE Trans Ultrason Ferroelectr Freq Control* 2016; 63 (10): 1613-1623.

197 Herbert A, Cruickshank JK, Laurent S, Boutouyrie P. Establishing reference values for central blood pressure and its amplification in a general healthy population and according to cardiovascular risk factors. *Eur Heart J* 2014; 35(44):3122-33.

198 Carlsson M, Andersson R, Bloch K, Steding-Ehrenborg K, Mosén H, Stahlberg F, *et al.* Cardiac output and cardiac index measured with cardiovascular magnetic resonance in healthy subjects, elite athletes and patients with congestive heart failure. *J. Cardiovasc. Magn. Reson*. 2012; 14:51.

199 O'Brien IA, O'Hare P, Corrall RJ. Heart rate variability in healthy subjects: effect of age and the derivation of normal ranges for tests of autonomic function. *Br Heart J* 1986; 55:348–54.

200 Widman E, Maksuti E, Larsson D, Urban MW, Bjällmark A, Larsson M. Shear wave elastography plaque characterization with mechanical testing validation: a phantom study. *Phys Med Biol* 2015; 60:3151–3174.